

Optimisation of neoadjuvant pembrolizumab therapy for locally advanced MSI-H/dMMR colorectal cancer using data-driven delay integro-differential equations

Georgio Hawi^{1, *}, Peter S. Kim^{1, †}, and Peter P. Lee^{2, †}

¹School of Mathematics and Statistics, University of Sydney, Sydney, Australia

²Department of Immuno-Oncology, Beckman Research Institute, City of Hope, Duarte, California, USA

*Corresponding author: georgio.hawi@sydney.edu.au

†These authors contributed comparably to this work

Abstract

Colorectal cancer (CRC) poses a major public health challenge due to its increasing prevalence, particularly among younger populations. Microsatellite instability-high (MSI-H) CRC and deficient mismatch repair (dMMR) CRC constitute 15% of all CRC and exhibit remarkable responsiveness to immunotherapy, especially with PD-1 inhibitors. Despite this, there is a significant need to optimise immunotherapeutic regimens to maximise clinical efficacy and patient quality of life whilst minimising monetary costs. To address this, we employ a novel framework driven by delay integro-differential equations to model the interactions among cancer cells, immune cells, and immune checkpoints. Several of these components are being modelled deterministically for the first time in cancer, paving the way for a deeper understanding of the complex underlying immune dynamics. We consider two compartments: the tumour site and the tumour-draining lymph node, incorporating phenomena such as dendritic cell (DC) migration, T cell proliferation, and CD8+ T cell exhaustion and reinvigoration. Parameter values and initial conditions are derived from experimental data, integrating various pharmacokinetic, bioanalytical, and radiographic studies, along with deconvolution of bulk RNA-sequencing data from the TCGA COADREAD and GSE26571 datasets. We finally optimise neoadjuvant treatment with pembrolizumab, a widely used PD-1 inhibitor, to balance efficacy, efficiency, and toxicity in locally advanced MSI-H/dMMR CRC patients. We improve upon currently FDA-approved therapeutic regimens for metastatic MSI-H/dMMR CRC, demonstrating that a single medium-to-high dose of pembrolizumab is sufficient for effective tumour eradication whilst being efficient, safe and practical.

1 Introduction

Colorectal cancer (CRC) is the third most common cancer worldwide, accounting for approximately 10% of all cancer cases [1] with more than 1.85 million cases and 850,000 deaths annually [2]. The American Cancer Society estimates that in the United States, there will be 152,810 new cases of CRC diagnosed and 53,010 deaths due to CRC [3] with individual risk factors including a family history of CRC, inflammatory bowel disease, and type 2 diabetes [4]. Despite CRC being diagnosed mostly

in adults 65 and older, there has been an increase in the incidence rate of CRC amongst younger populations [3, 5, 6] since the mid-1990s, with CRC being the leading cause of cancer-related deaths in adults under 55 [3]. In particular, since many people will not experience symptoms in the early stages of CRC, diagnoses often occur at a later stage when the disease is more advanced, where treatment is significantly less effective, and survival is much worse [7]. Of new CRC diagnoses, 20% of patients present with metastatic disease, while an additional 25% who initially have localised disease eventually develop metastases [2]. In the United States, the 5-year survival rates for stage IIIA, stage IIIB, and Stage IIIC colon cancer are 90%, 72%, and 53%, respectively, whilst stage IV CRC has a 5-year survival of only 12% [8].

Whilst many systemic therapies are available for advanced CRC, chemotherapy has been the main treatment approach, with fluoropyrimidine 5-fluorouracil being the only Food and Drug Administration (FDA) agent approved for metastatic CRC treatment for nearly 40 years [9]. Noting that folinic acid (leucovorin), a vitamin B derivative, increases the cytotoxicity of 5-fluorouracil [10], and with the approval of the topoisomerase I inhibitor irinotecan in 1996 and the platinum-based agent oxaliplatin, mainstay chemotherapy regimens such as FOLFOX (folinic acid, 5-fluorouracil, oxaliplatin) and FOLFIRI (folinic acid, 5-fluorouracil, irinotecan) have become integral to the treatment of advanced CRC [11]. However, the response rate of advanced CRC patients with 5-fluorouracil monotherapy remains at only 10 – 15%, with the addition of other anti-cancer drugs increasing response rates to only 40 – 50% [12].

Moreover, patients with the hypermutant microsatellite instability-high (MSI-H) phenotype who have reached metastasis are less responsive to conventional chemotherapy and have a poorer prognosis compared to patients with microsatellite stable (MSS) CRC [13]. MSI-H CRC is associated with the inactivation of mismatch repair (MMR) genes, including *MLH1*, *MSH2*, *MSH6*, and *PMS2*, leading to deficient MMR (dMMR) and impaired recognition and correction of spontaneous mutations by cells [14]. In particular, we note that in CRC, MSI-H and dMMR tumours are equivalent [15], and we denote these tumours as MSI-H/dMMR for the remainder of this work. Approximately 20% of stage II, 12% of stage III, and 4% of stage IV CRC tumours are diagnosed as MSI-H/dMMR [16–18], with approximately 80% of sporadic MSI-H/dMMR CRC caused by *MLH1* promoter hypermethylation [19]. This leads to a highly increased mutational rate, with MSI-H/dMMR CRC tumours having 10 – 100 times more somatic tumours compared to microsatellite stable (MSS) CRC tumours [14], resulting in increased tumour mutation burden (TMB) and neoantigen load, and immunogenic tumour microenvironment (TME) with dense immune cell infiltration [20, 21]. This immunogenicity results in patients with MSI-H/dMMR CRC having good prognosis for immunotherapy treatment, in particular to immune checkpoint inhibitors (ICIs) [22].

Immune checkpoints, such as programmed cell death-1 (PD-1), cytotoxic T-lymphocyte-associated antigen 4 (CTLA-4), and lymphocyte-activation gene 3 (LAG-3) normally downregulate immune responses after antigen activation [23]. CTLA-4 is expressed on activated T and B cells and plays a major role in downmodulating the initial stages of T cell activation and proliferation [24]. PD-1, a cell membrane receptor that is expressed on a variety of cell types, including activated T cells, activated B cells and monocytes, has been extensively researched in the context of cancer such as MSI-H/dMMR CRC [25, 26]. When PD-1 interacts with its ligands (PD-L1 and PD-L2), effector T cell activity is inhibited, resulting in downregulation of pro-inflammatory cytokine secretion and upregulation of immunosuppressive regulatory T cells (Tregs) [27, 28]. Cancers can exploit this by expressing PD-L1 themselves, evading immunosurveillance, and impairing the proliferation and activity of cytotoxic T lymphocytes (CTLs) [29]. Blockade of PD-1/PD-L1 complex formation reinvigorates effector T cell

activity, resulting in enhanced anti-tumour immunity and responses, leading to improved clinical outcomes in cancer patients [30, 31].

The KEYNOTE-177 phase III trial, NCT02563002, aimed to evaluate the efficacy of first-line pembrolizumab, an anti-PD-1 antibody, in metastatic MSI-H/dMMR CRC [19]. In the trial, 307 treatment-naive metastatic MSI-H/dMMR CRC patients were randomly assigned to receive pembrolizumab at a dose of 200 mg every 3 weeks or 5-fluorouracil-based chemotherapy every 2 weeks. A partial or complete response was observed in 43.8% of patients allocated to pembrolizumab therapy, compared with 33.1% of patients participating in 5-fluorouracil-based therapy. Furthermore, among patients who responded, 83% in the pembrolizumab group maintained response at 24 months, compared with 35% of patients receiving chemotherapy. These results motivated the FDA to approve pembrolizumab for the first-line treatment of unresectable or metastatic MSI-H/dMMR CRC on June 29, 2020 [32].

In the past couple of years, there has been a surge in research into the efficacy of neoadjuvant pembrolizumab in the treatment of high-risk stage II and stage III MSI-H/dMMR CRC [33]. One such phase II study is the NEOPRISM-CRC, NCT05197322, 31 patients with a high TMR and high-risk stage II or stage III MSI-H/dMMR CRC were given three cycles of pembrolizumab, at a dose of 200 mg every 3 weeks via IV infusion, and underwent surgery 4 – 6 weeks after the last dose was administered [34]. Seventeen patients exhibited pathologic complete responses (pCRs) (55%, 95% CI 36% – 73%), with the remaining patients having their tumours removed after surgery. After a median follow-up time of 6 months, recurrence was found in no patients, and the median cancer-free period was 9.7 months.

Another phase II trial, NCT04082572, aimed to evaluate the efficacy of neoadjuvant pembrolizumab on localised MSI-H/dMMR solid tumours [35]. As part of this, 27 MSI-H/dMMR CRC patients with locally advanced cancer were either given 200 mg pembrolizumab via IV infusion every 3 weeks for eight treatments followed by surgical resection or 200 mg pembrolizumab via IV infusion every 3 weeks for 16 treatments. Overall, 21 MSI-H/dMMR patients exhibited pCR, and among the 14 MSI-H/dMMR CRC patients in the resection group, 11 exhibited pCRs. Additionally, after a median follow-up time of 9.5 months, only two patients who underwent surgical resection experienced recurrence or progression.

An important question to consider is the appropriate dosing and spacing of ICI therapies to balance tumour reduction with factors such as monetary cost, toxicity, and side effects [36, 37]. A retrospective study by Dubé-Pelletier et al. of 80 patients with advanced non-small cell lung cancer (NSCLC) who received 4 mg/kg pembrolizumab every 6 weeks and 80 NSCLC patients who received 2 mg/kg pembrolizumab every 3 weeks, revealed that both therapies were comparable in terms of OS, toxicity and progression-free survival [38], despite the less frequent therapy being more cost-effective. Various pharmacokinetic models have been developed to optimise ICI therapy [39–42], with [43] showing that tripling the dosing interval of nivolumab, another anti-PD-1 antibody, from 240 mg every 2 weeks to 240 mg every 6 weeks leads to comparable efficacy despite financial costs decreasing threefold. Mathematical models provide a powerful framework for optimising treatment regimens, and in this work, we construct a comprehensive data-driven model of the immunobiology of MSI-H/dMMR CRC using delay integro-differential equations and use this to evaluate and optimise neoadjuvant pembrolizumab therapy in locally advanced MSI-H/dMMR CRC.

To date, there are no existing mathematical models in the literature for ICI therapy in locally advanced CRC; however, there are numerous models of CRC. Kirshtein et al. developed an ordinary differential equation (ODE) model of CRC progression incorporating immunological components such

as T helper cells, Tregs, dendritic cells (DCs), macrophages, and they considered the effects of carcinogenic cytokines and immunosuppressive agents [44]. They used data from the TCGA COADREAD database [45] to perform estimates for the steady states and initial conditions of model variables and considered data from all patients, regardless of the TNM stage. Moreover, this model was extended in [46] to include FOLFIRI treatment. Bozkurt et al. presented a relatively simple ODE model of CRC treatment with anthracycline doxorubicin and IL-2 immunotherapy, modelling cancer cells, natural killer (NK) cells, CD8+ T cells, and other lymphocytes [47]. De Pillis et al. developed an ODE model of CRC with irinotecan and monoclonal antibody therapies, in particular cetuximab and panitumumab, modelling similar quantities [48].

ICI therapy has been modelled extensively in other cancers, and Butner et al. provide a comprehensive review of the merits and weaknesses of various modelling approaches, including continuum partial differential equations (PDEs), continuum ODEs, agent-based modelling (ABM), and hybrid modelling in [49]. We now summarise a few pre-existing differential-equation-based models of PD-1 blockade therapies. Lai et al. modelled the effects of anti-PD-1 and vaccines on cancer, taking into account DC maturation by high mobility group box 1 (HMGB1) and interleukin-2 (IL-2) and interleukin-12 (IL-12) in [50]. This model was adapted in [51] to optimise combination PD-1 and vascular endothelial growth factor (VEGF) inhibitor therapies in cancer. Siewe et al. modelled how transforming growth factor beta (TGF- β) can be used to overcome resistance to PD-1 blockade and also incorporated macrophages, Tregs, IL-2, IL-12, TGF- β , interleukin-10 (IL-10), and chemokine ligand 2 (CCL-2) [52]. This model was extended in [53] to model cancer therapy with PD-1 inhibitors with CSF-1 blockade, also including the cytokine tumour necrosis factor (TNF). Additionally, Liao et al. constructed a mathematical model that demonstrated the pro-cancer or anti-cancer nature of interleukin-27 (IL-27) in combination with anti-PD-1, incorporating the following cytokines: IL-27, TGF- β , IL-2, interferon-gamma (IFN- γ), and IL-10 [54].

There are, however, a multitude of limitations and drawbacks to these pre-existing models of CRC and ICI therapy. One of the biggest issues is that mature DC migration to the tumour-draining lymph node (TDLN) to activate naive T cells is not addressed, with T cell proliferation and migration to the tumour site (TS) also not being addressed. Kumbhari et al. attempted to address this in [55] and [56] in the context of optimising cancer vaccine therapy; however, activation is treated as occurring instantaneously which has been shown to be false experimentally [57]. Moreover, since T cell activation and proliferation take a non-negligible amount of time to occur, immune checkpoint inhibition of these processes must take this into account. No papers to date have properly considered this inhibition deterministically throughout the whole proliferation and activation programs since examining inhibition at a single moment in time is insufficient to characterise this properly. Additionally, damage-associated molecular patterns (DAMPs), released by necrotic cancer cells, induce DC maturation. To date, DC maturation is considered only by HMGB1 in some models, with other important DAMPs such as calreticulin not being taken into account [58]. Furthermore, no deterministic model to date has adequately addressed CD8+ T cell exhaustion due to prolonged antigen exposure [59], nor their potential reinvigoration through immune checkpoint blockade.

Many immune cell types and cytokines that are prevalent and have important roles in the TME have not been incorporated in pre-existing deterministic models of cancer. These include cancer-associated fibroblasts (CAFs), which are the most abundant component of the TME and produce immunosuppressive cytokines [60, 61], and cytokines such as interleukin-6 (IL-6) [62]. One thing to note is that pre-existing deterministic models mostly estimate cytokine production parameters via biologically informed assumptions, which can lead to inaccuracies and is a somewhat ad hoc approach. In this

work, we construct a mathematical model using data-driven delay integro-differential equations that addresses these drawbacks, incorporating all of the aforementioned processes and species, and use this to optimise neoadjuvant pembrolizumab therapy for locally advanced MSI-H/dMMR CRC.

It is prudent for us to briefly outline the functions and processes of some immune cells in the TME since their interaction with cancer cells directly or through chemokine/cytokine signalling significantly influences the efficacy of therapeutic regimens [63]. T cell activation occurs in the lymph node and occurs through T cell receptor (TCR) recognition of cancer antigen presented by major histocompatibility complex (MHC) class I molecules, in the case of CD8+ T cells, and MHC class II molecules, in the case of CD4+ T cells, expressed on the surfaces of mature DCs [64]. CTLs recognise cancer cells through TCR detection of peptide major histocompatibility complexes (pMHCs) on cancer cell surfaces via MHC class I [65]. CD8+ cells, as well as NK cells, are amongst the most cytotoxic and important cells in cancer cell lysis [66], in addition to secreting pro-inflammatory cytokines such as IL-2, IFN- γ , and TNF [67]. These are also secreted by CD4+ T helper 1 (Th1) cells and are an important part of cell-mediated immunity, allowing for neutrophil chemotaxis and macrophage activation [68]. Furthermore, we must also consider Tregs, which are vital in immune tissue homeostasis since they are able to suppress the synthesis of pro-inflammatory cytokines and control intestinal inflammatory processes [69]. This is done in a variety of ways, including the production of immunomodulatory and immunosuppressive cytokines such as TGF- β , IL-10, and interleukin 35 (IL-35) [70, 71]. We note that naive CD4+ T cells can differentiate towards multiple additional phenotypes such as Th2, Th9, Th22, Tfh and Th17 cells, each involved in the pathogenesis of cancer [72, 73].

Also of importance in CRC are macrophages, which, like T cells, are able to produce pro-inflammatory and anti-inflammatory cytokines [74]. Naive macrophages, denoted M0 macrophages, can differentiate into two main phenotypes: classically activated M1 macrophages and alternatively activated M2 macrophages. These names were given since M1 macrophages promote Th1 cell responses, and M2 macrophages promote Th2 responses, with Th1-associated cytokines downregulating M2 activity, and vice-versa [75]. M1 macrophages contribute to the inflammatory response by activating endothelial cells, promoting the induction of nitric oxide synthase, and producing large amounts of pro-inflammatory cytokines such as TNF, interleukin 1 β (IL-1 β), and IL-12 [76]. On the other hand, M2 macrophages are responsible for wound healing and the resolution of inflammation through phagocytosing apoptotic cells and releasing anti-inflammatory mediators such as IL-10, interleukin 13 α 1 (IL-13 α 1), and CC Motif Chemokine Ligand 17 (CCL17) [77].

It is important to note that the M1/M2 macrophage dichotomy is somewhat of a simplification. Macrophages are highly plastic and have been demonstrated to integrate environmental signals to change their phenotype and physiology [78]. To account for this, in the model, we incorporate macrophage polarisation and repolarisation between its anti-tumour and immunosuppressive phenotype by various cytokines and proteins.

2 Mathematical Model

2.1 Model Assumptions

The variables and their units in the model are shown in [Table 1](#). For simplicity, we ignore spatial effects in the model, ignoring the effects of diffusion, advection, and chemotaxis by all species. We assume the system has two compartments: one at the TS, located in the colon or rectum, and one at the tumour-

draining lymph node (TDLN). We assume that cytokines in the TS are produced only by effector or activated cells and that DAMPs in the TS are only produced by necrotic cancer cells. We assume that all mature DCs in the TDLN are cancer-antigen bearing and that all T cells in the TS are primed with cancer antigens. Furthermore, we assume that all activated T cells in the TDLN are activated with cancer antigens and that T cell proliferation/division follows a deterministic program. We ignore CD4+ and CD8+ memory T cells and assume that naive CD4+ T cells differentiate immediately upon activation. We also assume that all Tregs in the TS are natural Tregs (nTregs), ignoring induced Tregs (iTregs). We assume, for simplicity, that activated macrophages polarise into the M1/M2 dichotomy. Finally, we assume a constant solution history, where the history for each species is set to its respective initial condition.

Table 1: Variables used in the model. Quantities in the top box are in units of cell/cm³, quantities in the second and bottom box are in units of g/cm³, and all other quantities are in units of molec/cm³. All quantities refer to tumour site density/concentration unless otherwise specified. TDLN denotes the tumour-draining lymph node, whilst TS denotes the tumour site.

Var	Description	Var	Description
C	Viable cancer cell density	N_c	Necrotic cell density
D_0	Immature DC density	D	Mature DC density at TS
D^{LN}	Mature DC density at TDLN	T_0^8	Naive CD8+ T cell density in TDLN
T_A^8	Effector CD8+ T cell density in TDLN	T_8	Effector CD8+ T cell density at TS
T_{ex}	Exhausted CD8+ T cell density at TS	T_0^4	Naive CD4+ T cell density in TDLN
T_A^1	Effector Th1 cell density in TDLN	T_1	Effector Th1 cell density at TS
T_0^r	Naive Treg density in TDLN	T_A^r	Effector Treg density in TDLN
T_r	Effector Treg density at TS	C_F	CAF density
M_0	Naive macrophage density	M_1	M1 macrophage density
M_2	M2 macrophage density	K_0	Naive NK cell density
K	Activated NK cell density		
H	HMGB1 concentration	S	Calreticulin concentration
I_2	IL-2 concentration	I_γ	IFN- γ concentration
I_α	TNF concentration	I_β	TGF- β concentration
I_{10}	IL-10 concentration	I_6	IL-6 concentration
P_D	PD-1 concentration at TS	P_D^{8LN}	PD-1 concentration on effector CD8+ T cells in TDLN
P_D^{1LN}	PD-1 concentration on effector Th1 cells in TDLN	P_D^{rLN}	PD-1 concentration on effector Tregs in TDLN
P_L^C	PD-L1 concentration on cancer cells at TS	P_L	PD-L1 concentration at TS
P_L^{LN}	PD-L1 concentration in TDLN	Q^{8LN}	PD-1/PD-L1 complex concentration on effector CD8+ T cells in TDLN
Q^{1LN}	PD-1/PD-L1 complex concentration on effector Th1 cells in TDLN	Q^{rLN}	PD-1/PD-L1 complex concentration on effector Tregs in TDLN
A_1	Concentration of pembrolizumab at TS	A_1^{LN}	Concentration of pembrolizumab in TDLN

We assume that all species, X_i , degrade/die at a rate proportional to their concentration, with decay constant d_{X_i} . We assume that the rate of activation/polarisation of a species X_i by a species X_j follows the Michaelis-Menten kinetic law $\lambda_{X_i X_j} X_i \frac{X_j}{K_{X_i X_j} + X_j}$, for rate constant $\lambda_{X_i X_j}$, and half-saturation

constant $K_{X_i X_j}$. Similarly, we model the rate of inhibition of a species X_i by a species X_j using a term with form $\lambda_{X_i X_j} \frac{X_i}{1+X_j/K_{X_i X_j}}$ for rate constant $\lambda_{X_i X_j}$, and half-saturation constant $K_{X_i X_j}$. Production of X_i by X_j is modelled using mass-action kinetics unless otherwise specified so that the rate that X_i is formed is given by $\lambda_{X_i X_j} X_j$ for some positive constant $\lambda_{X_i X_j}$. Finally, we assume that the rate of lysis of X_i by X_j follows mass-action kinetics in the case where X_j is a cell and follows Michaelis-Menten kinetics in the case where X_j is a cytokine.

2.2 Model Summary

We now outline some of the main processes accounted for in the model, with all processes and equations being explained in [Section 2.3](#).

1. Effector CD8+ T cells, Th1 cells, and NK cells induce apoptosis of cancer cells with this being inhibited by TGF- β , IL-6, PD-1 and PD-L1. However, TNF and IFN- γ induce necroptosis of cancer cells, causing them to become necrotic before they are removed.
2. Necrotic cancer cells release DAMPs such as HMGB1 and calreticulin, which stimulate immature DCs to mature.
3. Some mature DCs migrate to the T cell zone of the TDLN, where they activate naive CD8+ and CD4+ T cells, as well as naive nTregs, with this being inhibited by PD-1.
4. Activated T cells undergo clonal expansion and proliferate rapidly in the TDLN, with this proliferation being inhibited by the PD-1/PD-L1 complex.
5. T cells that have completed proliferation migrate to the TS and perform effector functions, including the secretion of pro-inflammatory (IL-2, IFN- γ , and TNF) and immunosuppressive (TGF- β , IL-10, and IL-6) cytokines. Extended exposure to the cancer antigen can lead CD8+ T cells to become exhausted; however, this exhaustion can be reversed by pembrolizumab.
6. In addition, mature DCs, NK cells, macrophages and CAFs secrete cytokines that can activate NK cells and polarise and repolarise macrophages into pro-inflammatory and immunosuppressive phenotypes.

2.3 Model Equations

2.3.1 Equations for Cancer Cells (C and N_c)

Viable cancer cells are killed by effector CD8+ T cells [79], activated NK cells [80] and Th1 cells [81, 82] through direct contact, whilst TNF and IFN- γ indirectly eliminate cancer cells via activating cell death pathways [83–85]. In particular, TNF and IFN- γ induce the necroptosis, programmed necrotic cell death, of cancer cells [84, 86]. We note that TGF- β and PD-L1 on cancer cells have been shown to inhibit cancer cell lysis by CD8+ T cells [87, 88], and IL-6 and PD-1 have been shown to inhibit NK cell cytotoxicity [89, 90]. We assume that viable cancer cells grow logistically, as is done in many CRC

models [44, 46, 48], due to space and resource competition in the TME. Combining these, we have

$$\frac{dC}{dt} = \underbrace{\lambda_C C \left(1 - \frac{C}{C_0}\right)}_{\text{growth}} - \underbrace{\lambda_{CT_8} T_8 \frac{1}{1 + I_\beta / K_{CI_\beta}} \frac{1}{1 + P_L^C / K_{CP_L^C}} C}_{\substack{\text{elimination by } T_8 \\ \text{inhibited by } I_\beta \text{ and } P_L}} - \underbrace{\lambda_{CT_1} T_1 C}_{\text{elimination by } T_1} \quad (2.1)$$

$$- \underbrace{\lambda_{CK} K \frac{1}{1 + I_6 / K_{CI_6}} \frac{1}{1 + P_D / K_{CP_D}} C}_{\substack{\text{elimination by } K \\ \text{inhibited by } I_6 \text{ and } P_D}} - \underbrace{\lambda_{CI_\alpha} \frac{I_\alpha}{K_{CI_\alpha} + I_\alpha} C}_{\text{elimination by } I_\alpha} - \underbrace{\lambda_{CI_\gamma} \frac{I_\gamma}{K_{CI_\gamma} + I_\gamma} C}_{\text{elimination by } I_\gamma},$$

$$\frac{dN_c}{dt} = \underbrace{\lambda_{CI_\alpha} \frac{I_\alpha}{K_{CI_\alpha} + I_\alpha} C}_{\text{Elimination by } I_\alpha} + \underbrace{\lambda_{CI_\gamma} \frac{I_\gamma}{K_{CI_\gamma} + I_\gamma} C}_{\text{Elimination by } I_\gamma} - \underbrace{d_{N_c} N_c}_{\text{Removal}}. \quad (2.2)$$

2.3.2 Equation for HMGB1 (H)

The molecule HMGB1 is released by necrotic cancer cells [91] and CAFs [92] so that

$$\frac{dH}{dt} = \underbrace{\lambda_{HN_c} N_c}_{\text{production by } N_c} + \underbrace{\lambda_{HC_F} C_F}_{\text{production by } C_F} - \underbrace{d_H H}_{\text{degradation}}. \quad (2.3)$$

2.3.3 Equation for Calreticulin (S)

Necrotic cancer cells release calreticulin [93] so that

$$\frac{dS}{dt} = \underbrace{\lambda_{SN_c} N_c}_{\text{production by } N_c} - \underbrace{d_S S}_{\text{degradation}}. \quad (2.4)$$

2.3.4 Equations for Immature and Mature DCs in the TS (D_0 and D)

Immature DCs are stimulated to mature via DAMPs such as HMGB1 and calreticulin [58]; however, we employ Michaelis-Menten kinetics to accommodate for the limited rate of receptor recycling time [50]. In addition, activated NK cells have been shown to efficiently kill immature DCs but not mature DCs [94, 95]. We also need to consider that some mature DCs migrate into the T cell zone of the TDLN and stimulate naive T cells, causing them to be activated [96, 97]. Assuming that immature DCs are supplied at a rate \mathcal{A}_{D_0} , we have that

$$\frac{dD_0}{dt} = \underbrace{\mathcal{A}_{D_0}}_{\text{source}} - \underbrace{\lambda_{DH} D_0 \frac{H}{K_{DH} + H}}_{D_0 \rightarrow D \text{ by } H} - \underbrace{\lambda_{DS} D_0 \frac{S}{K_{DS} + S}}_{D_0 \rightarrow D \text{ by } S} - \underbrace{\lambda_{D_0K} D_0 K}_{\text{elimination by } K} - \underbrace{d_{D_0} D_0}_{\text{death}}, \quad (2.5)$$

$$\frac{dD}{dt} = \underbrace{\lambda_{DH} D_0 \frac{H}{K_{DH} + H}}_{D_0 \rightarrow D \text{ by } H} + \underbrace{\lambda_{DS} D_0 \frac{S}{K_{DS} + S}}_{D_0 \rightarrow D \text{ by } S} - \underbrace{\lambda_{DD^{\text{LN}}} D}_{D \text{ migration to TDLN}} - \underbrace{d_D D}_{\text{death}}. \quad (2.6)$$

2.3.5 Equation for Mature DCs in the TDLN (D^{LN})

We assume a fixed DC migration time of τ_m and also assume that only $e^{-d_D \tau_m}$ of the mature DCs that leave the TS survive migration. Taking into account the volume change between the TS and the

TDLN, we have that

$$\frac{dD^{\text{LN}}}{dt} = \frac{V_{\text{TS}}}{V_{\text{LN}}} \underbrace{\lambda_{DD^{\text{LN}}} e^{-d_D \tau_m} D(t - \tau_m)}_{D \text{ migration to TDLN}} - \underbrace{d_D D^{\text{LN}}}_{\text{death}}. \quad (2.7)$$

2.3.6 Equation for Naive CD8+ T Cells in the TDLN (T_0^8)

We assume that naive CD8+ T cells come into the TDLN at a constant rate and that they have not undergone cell division, nor will they until their activation. For simplicity, we do not consider cytokines in the TDLN, absorbing their influence into $\lambda_{T_0^8 T_A^8}$. We do, however, explicitly take into account the influence of PD-1 in the TDLN, which has been shown to inhibit T cell activation through limiting naive T cells from binding to mature DCs [98, 99]. Recalling that T cells that have become activated by mature DCs are no longer naive, and taking this all into account, leads to

$$\frac{dT_0^8}{dt} = \underbrace{\mathcal{A}_{T_0^8}}_{\text{source}} - \underbrace{R^8(t)}_{\text{CD8+ T cell activation}} - \underbrace{d_{T_0^8} T_0^8}_{\text{death}}, \quad (2.8)$$

where $R^8(t)$ is defined as

$$R^8(t) := \frac{\lambda_{T_0^8 T_A^8} e^{-d_{T_0^8} \tau_8^{\text{act}}} D^{\text{LN}}(t - \tau_8^{\text{act}}) T_0^8(t - \tau_8^{\text{act}})}{\underbrace{1 + \int_{t - \tau_8^{\text{act}}}^t P_D^{\text{8LN}}(s) ds / K_{T_0^8} P_D^{\text{8LN}}}_{\text{CD8+ T cell activation inhibited by } P_D^{\text{8LN}}}}. \quad (2.9)$$

In particular, since PD-1 inhibits T cell activation during the whole activation process, it is not sufficient to consider point estimates of PD-1 concentration. Instead, we resort to considering the integrals of the concentration of this immune checkpoint protein throughout the entire τ_8^{act} time that the CD8+ T cell takes to complete activation. This is because these integrals are proportional (with a proportionality constant of $1/\tau_8^{\text{act}}$) to the average concentration of these proteins throughout activation, allowing us to properly incorporate its inhibition by PD-1.

2.3.7 Equation for Effector CD8+ T Cells in the TDLN (T_A^8)

It is known that activated CD8+ T cells undergo clonal expansion in the TDLN and differentiate before they stop proliferating and migrate to the TS [100, 101].

We assume that activated CD8+ T cells proliferate up to n_{max}^8 times upon which they stop dividing. For simplicity, we assume that the death rate of CD8+ T cells that have not completed their division program is equal to $d_{T_0^8}$, the death rate of naive CD8+ T cells, regardless of the number of cell divisions previously undergone. We also assume that only activated CD8+ T cells that have undergone n_{max}^8 divisions become effector CD8+ T cells, which will leave the TDLN and migrate to the TS. Furthermore, we assume a constant cell cycle time Δ_8 , except for the first cell division, which has cycle time Δ_8^0 . Thus, the duration of the activated CD8+ T cell division program to n_{max}^8 divisions is given by

$$\tau_{T_A^8} = \Delta_8^0 + (n_{\text{max}}^8 - 1)\Delta_8. \quad (2.10)$$

In particular, we must take into account that some T cells will die before the division program is complete, and so we must introduce a shrinkage factor of $e^{-d_{T_0^8} \tau_{T_A^8}}$. Furthermore, we must also take into account that the PD-1/PD-L1 complex inhibits CD8+ T cell proliferation throughout the program

[24, 102]. We must also consider that some of these effector CD8+ T cells will migrate to the TS to perform effector functions. We finally assume that the death rate of CD8+ T cells that have completed their division program is equal to the death rate of CD8+ T cells in the TS. Taking this all into account leads to

$$\frac{dT_A^8}{dt} = \underbrace{\frac{2^{n_{\max}^8} e^{-d_{T_0^8} \tau_{T_A^8}} R^8(t - \tau_{T_A^8})}{1 + \int_{t-\tau_{T_A^8}}^t Q^{\text{8LN}}(s) ds / K_{T_A^8} Q^{\text{8LN}}}}_{\text{CD8+ T cell proliferation inhibited by } Q^{\text{8LN}}} - \underbrace{\lambda_{T_A^8 T_8} T_A^8}_{T_A^8 \text{ migration to TS}} - \underbrace{d_{T_8} T_A^8}_{\text{death}}. \quad (2.11)$$

2.3.8 Equation for Effector and Exhausted CD8+ T Cells in the TS (T_8 and T_{ex})

We assume that it takes τ_a amount of time for effector CD8+ T cells in the TDLN to migrate to the TS. We must also account for CTL expansion due to positive growth factors such as IL-2 [103]. Furthermore, the death of CD8+ T cells is resisted by IL-10 [104, 105].

However, chronic antigen exposure can cause effector CD8+ T cells to enter a state of exhaustion, where they lose their ability to kill cancer cells, and the rate of cytokine secretion significantly decreases [59, 106, 107]. We denote this exhausted CD8+ T cell population as $T_{\text{ex}}(t)$. It has also been shown that pembrolizumab can “reinvigorate” these cells back into the effector state [30, 108]. We model the re-invigoration and exhaustion using Michaelis-Menten terms in A_1 and $\int_{t-\tau_l}^t C(s) ds$ respectively, where τ_l is the median time that CD8+ T cells take to become exhausted after entering the TS. In particular, this has been shown to be more appropriate than simple mass-action kinetics as it accounts for extended antigen exposure [109].

As such, remembering to take the volume change between the TDLN and the TS into account, this implies that

$$\begin{aligned} \frac{dT_8}{dt} = & \frac{V_{\text{LN}}}{V_{\text{TS}}} \underbrace{\lambda_{T_A^8 T_8} e^{-d_{T_8} \tau_a} T_A^8 (t - \tau_a)}_{T_A^8 \text{ migration to TS}} + \underbrace{\lambda_{T_8 I_2} \frac{T_8 I_2}{K_{T_8 I_2} + I_2}}_{\text{growth by } I_2} \\ & - \underbrace{\lambda_{T_8 C} \frac{T_8 \int_{t-\tau_l}^t C(s) ds}{K_{T_8 C} + \int_{t-\tau_l}^t C(s) ds}}_{T_8 \rightarrow T_{\text{ex}} \text{ from } C \text{ exposure}} + \underbrace{\lambda_{T_{\text{ex}} A_1} \frac{T_{\text{ex}} A_1}{K_{T_{\text{ex}} A_1} + A_1}}_{T_{\text{ex}} \rightarrow T_8 \text{ by } A_1} - \underbrace{\frac{d_{T_8} T_8}{1 + I_{10}/K_{T_8 I_{10}}}}_{\text{death inhibited by } I_{10}}, \end{aligned} \quad (2.12)$$

$$\frac{dT_{\text{ex}}}{dt} = \underbrace{\lambda_{T_8 C} \frac{T_8 \int_{t-\tau_l}^t C(s) ds}{K_{T_8 C} + \int_{t-\tau_l}^t C(s) ds}}_{T_8 \rightarrow T_{\text{ex}} \text{ from } C \text{ exposure}} - \underbrace{\lambda_{T_{\text{ex}} A_1} \frac{T_{\text{ex}} A_1}{K_{T_{\text{ex}} A_1} + A_1}}_{T_{\text{ex}} \rightarrow T_8 \text{ by } A_1} - \underbrace{\frac{d_{T_{\text{ex}}} T_{\text{ex}}}{1 + I_{10}/K_{T_{\text{ex}} I_{10}}}}_{\text{death inhibited by } I_{10}}. \quad (2.13)$$

2.3.9 Equation for Naive CD4+ T Cells in the TDLN (T_0^4)

For simplicity, we consider only the Th1 subtype that naive CD4+ T cells differentiate into upon activation, absorbing the influence of cytokines via the kinetic rate constant $\lambda_{T_0^4 T_A^1}$. Taking into account that PD-1 inhibits Th1 cell activation and some mature DCs migrate into the TDLN and activate naive CD4+ T cells, causing them to no longer be naive, and assuming that naive CD4+ T

cells come into the TDLN at a rate $\mathcal{A}_{T_0^4}$, we can write a similar equation to (2.8):

$$\frac{dT_0^4}{dt} = \underbrace{\mathcal{A}_{T_0^4}}_{\text{source}} - \underbrace{(R^1(t))}_{\text{CD4+ T cell activation}} - \underbrace{d_{T_0^4} T_0^4}_{\text{death}}, \quad (2.14)$$

where $R^1(t)$ is defined as

$$R^1(t) = \frac{\lambda_{T_0^4 T_A^1} e^{-d_{T_0^4} \tau_{\text{act}}^4} D^{\text{LN}}(t - \tau_{\text{act}}^4) T_0^4(t - \tau_{\text{act}}^4)}{\underbrace{1 + \int_{t - \tau_{\text{act}}^4}^t P_D^{\text{LLN}}(s) ds / K_{T_0^4} P_D^{\text{LLN}}}_{T_A^1 \text{ activation inhibited by } P_D^{\text{LLN}}}}. \quad (2.15)$$

2.3.10 Equation for Effector Th1 Cells in the TDLN (T_A^1)

We assume that Th1 cells proliferate up to n_{max}^1 times, upon which they stop dividing and become effector cells. As before, we assume that the death rate of Th1 that have not completed their division program is equal to $d_{T_0^4}$, the death rate of naive CD4+ T cells, regardless of the number of cell divisions previously undergone or their phenotype. We assume a constant cell cycle time Δ_1 , except for the first cell division, which has cycle time Δ_1^0 . Thus, the duration of the Th1 cell division program to n_{max}^1 divisions is given by

$$\tau_{T_A^1} = \Delta_1^0 + (n_{\text{max}}^1 - 1)\Delta_1. \quad (2.16)$$

In particular, we must take into account that some Th1 cells will die before the division program is complete, so we must introduce a shrinkage factor of $e^{-d_{T_0^4} \tau_{T_A^1}}$. Furthermore, we must also take into account that the PD-1/PD-L1 complex inhibits Th1 cell proliferation throughout its program [24, 102]. We also assume that the death rate of Th1 cells that have completed their division program is equal to the corresponding degradation rate in the TS. Taking this all into account, and incorporating effector Th1 cell migration to the TS, leads to

$$\frac{dT_A^1}{dt} = \frac{2^{n_{\text{max}}^1} e^{-d_{T_0^4} \tau_{T_A^1}} R^1(t - \tau_{T_A^1})}{\underbrace{1 + \int_{t - \tau_{T_A^1}}^t Q^{\text{LLN}}(s) ds / K_{T_A^1} Q^{\text{LLN}}}_{\text{Th1 cell proliferation inhibited by } Q^{\text{LLN}}}} - \underbrace{\lambda_{T_A^1 T_1} T_A^1}_{T_A^1 \text{ migration to TS}} - \underbrace{d_{T_1} T_A^1}_{\text{death}}. \quad (2.17)$$

2.3.11 Equation for Effector Th1 Cells in the TS (T_1)

We assume that it takes τ_a amount of time for these cells to migrate to the TS. We take into account the fact that IL-2 induces the growth of effector Th1 cells [110]. Hence,

$$\frac{dT_1}{dt} = \frac{V_{\text{LN}}}{V_{\text{TS}}} \underbrace{\lambda_{T_A^1 T_1} e^{-d_{T_1} \tau_a} T_A^1(t - \tau_a)}_{T_A^1 \text{ migration to TS}} + \underbrace{\lambda_{T_1 I_2} \frac{T_1 I_2}{K_{T_1 I_2} + I_2}}_{\text{growth by } I_2} - \underbrace{d_{T_1} T_1}_{\text{death}}. \quad (2.18)$$

2.3.12 Equation for Naive Tregs in the TDLN (T_0^r)

Finally, we consider the concentration of naive Tregs in the TDLN, following the same procedure as for CD8+ T cells and Th1 cells. We absorb the influence of cytokines on Treg activation via the kinetic rate constant $\lambda_{T_0^r T_A^r}$. We also take into account that PD-1 inhibits Treg activation, and some mature DCs migrate into the TDLN and activate naive Tregs, causing them to no longer be naive. Assuming

that naive Tregs come into the TDLN at a rate $\mathcal{A}_{T_0^r}$, we can write a similar equation to (2.8) and (2.14):

$$\frac{dT_0^r}{dt} = \underbrace{\mathcal{A}_{T_0^r}}_{\text{source}} - \underbrace{R^r(t)}_{\text{Treg activation}} - \underbrace{d_{T_0^r} T_0^r}_{\text{death}}, \quad (2.19)$$

where

$$R^r(t) = \frac{\lambda_{T_0^r T_A^r} e^{-d_{T_0^r} \tau_{\text{act}}^r} D^{\text{LN}}(t - \tau_{\text{act}}^r) T_0^r(t - \tau_{\text{act}}^r)}{\underbrace{1 + \int_{t - \tau_{\text{act}}^r}^t P_D^{\text{rLN}}(s) ds / K_{T_0^r} P_D^{\text{rLN}}}_{T_A^r \text{ activation inhibited by } P_D^{\text{rLN}}}}. \quad (2.20)$$

2.3.13 Equation for Effector Tregs in the TDLN (T_A^r)

We assume that activated Tregs proliferate up to n_{max}^r , times upon which they stop dividing and become effector Tregs. As before, we assume that the death rate of Tregs that have not completed their division program is equal to $d_{T_0^r}$, the death rate of naive Tregs. We assume a constant cell cycle time Δ_r , except for the first cell division, which has cycle time Δ_r^0 . Thus, the duration of the activated Treg division program to n_{max}^r divisions is given by

$$\tau_{T_A^r} = \Delta_r^0 + (n_{\text{max}}^r - 1)\Delta_r. \quad (2.21)$$

In particular, we must take into account that some T cells will die before the division program is complete, so we must introduce a shrinkage factor of $e^{-d_{T_0^r} \tau_{T_A^r}}$. Furthermore, we must also take into account that the PD-1/PD-L1 complex inhibits Treg proliferation throughout the program [102, 111]. We finally assume that the death rate of effector Tregs in the TDLN is equal to the corresponding degradation rate in the TS. Taking this all into account, and incorporating effector Treg migration to the TS, leads to

$$\frac{dT_A^r}{dt} = \frac{2^{n_{\text{max}}^r} e^{-d_{T_0^r} \tau_{T_A^r}} R^r(t - \tau_{T_A^r})}{\underbrace{1 + \int_{t - \tau_{T_A^r}}^t Q^{\text{rLN}}(s) ds / K_{T_A^r} Q^{\text{rLN}}}_{\text{Treg proliferation inhibited by } Q^{\text{rLN}}}} - \underbrace{\lambda_{T_A^r T_r} T_A^r}_{T_A^r \text{ migration to TS}} - \underbrace{d_{T_r} T_A^r}_{\text{death}}. \quad (2.22)$$

2.3.14 Equation for Effector Tregs in the TS (T_r)

Assuming that it also takes τ_a amount of time for Tregs to migrate to the TS, we have that

$$\frac{dT_r}{dt} = \frac{V_{\text{LN}}}{V_{\text{TS}}} \underbrace{\lambda_{T_A^r T_r} e^{-d_{T_r} \tau_a} T_A^r(t - \tau_a)}_{T_A^r \text{ migration to TS}} - \underbrace{d_{T_r} T_r}_{\text{death}}. \quad (2.23)$$

2.3.15 Equation for CAFs (C_F)

We assume that CAFs grow logistically for the same reason as cancer cells. We take into account the growth rate of CAFs and their induced growth due to fibrotic signalling via TGF- β [112]. In particular, we note that their effects are saturation-limited and need to be incorporated via Michaelis-Menten kinetics. Hence,

$$\frac{dC_F}{dt} = \left(\underbrace{\lambda_{C_F}}_{\text{growth}} + \underbrace{\lambda_{C_F I_\beta} \frac{I_\beta}{K_{C_F I_\beta} + I_\beta}}_{I_\beta\text{-induced growth}} \right) \underbrace{C_F \left(1 - \frac{C_F}{C_{F0}} \right)}_{\text{growth}} - \underbrace{d_{C_F} C_F}_{\text{death}}. \quad (2.24)$$

2.3.16 Equations for Naive, M1, and M2 Macrophages (M_0 , M_1 , and M_2)

TNF and IFN- γ polarise naive macrophages into M1 macrophages [113–116], whilst IL-10 and PD-L1 polarise naive macrophages into the M2 phenotype [117–119]. In addition, TGF- β and IL-6 induce M1 macrophages to convert into M2 macrophages [120–122]. Furthermore, M2 macrophages change phenotype to M1 under the influence of TNF [113] and IFN- γ also induces M2 to M1 phenotype change [123]. Assuming a production rate \mathcal{A}_{M_0} of naive macrophages, we thus have that

$$\begin{aligned} \frac{dM_0}{dt} = & \underbrace{\mathcal{A}_{M_0}}_{\text{source}} - \underbrace{\lambda_{M_1 I_\alpha} M_0 \frac{I_\alpha}{K_{M_1 I_\alpha} + I_\alpha}}_{M_0 \rightarrow M_1 \text{ by } I_\alpha} - \underbrace{\lambda_{M_1 I_\gamma} M_0 \frac{I_\gamma}{K_{M_1 I_\gamma} + I_\gamma}}_{M_0 \rightarrow M_1 \text{ by } I_\gamma} - \underbrace{\lambda_{M_2 I_{10}} M_0 \frac{I_{10}}{K_{M_2 I_{10}} + I_{10}}}_{M_0 \rightarrow M_2 \text{ by } I_{10}} \\ & - \underbrace{\lambda_{M_2 P_L} M_0 \frac{P_L}{K_{M_2 P_L} + P_L}}_{M_0 \rightarrow M_2 \text{ by } P_L} - \underbrace{d_{M_0} M_0}_{\text{degradation}}, \end{aligned} \quad (2.25)$$

$$\begin{aligned} \frac{dM_1}{dt} = & \underbrace{\lambda_{M_1 I_\alpha} M_0 \frac{I_\alpha}{K_{M_1 I_\alpha} + I_\alpha}}_{M_0 \rightarrow M_1 \text{ by } I_\alpha} + \underbrace{\lambda_{M_1 I_\gamma} M_0 \frac{I_\gamma}{K_{M_1 I_\gamma} + I_\gamma}}_{M_0 \rightarrow M_1 \text{ by } I_\gamma} + \underbrace{\lambda_{M I_\gamma} M_2 \frac{I_\gamma}{K_{M I_\gamma} + I_\gamma}}_{M_2 \rightarrow M_1 \text{ by } I_\gamma} + \underbrace{\lambda_{M I_\alpha} M_2 \frac{I_\alpha}{K_{M I_\alpha} + I_\alpha}}_{M_2 \rightarrow M_1 \text{ by } I_\alpha} \\ & - \underbrace{\lambda_{M I_\beta} M_1 \frac{I_\beta}{K_{M I_\beta} + I_\beta}}_{M_1 \rightarrow M_2 \text{ by } I_\beta} - \underbrace{\lambda_{M I_6} M_1 \frac{I_6}{K_{M I_6} + I_6}}_{M_1 \rightarrow M_2 \text{ by } I_6} - \underbrace{d_{M_1} M_1}_{\text{degradation}}, \end{aligned} \quad (2.26)$$

$$\begin{aligned} \frac{dM_2}{dt} = & \underbrace{\lambda_{M_2 I_{10}} M_0 \frac{I_{10}}{K_{M_2 I_{10}} + I_{10}}}_{M_0 \rightarrow M_2 \text{ by } I_{10}} + \underbrace{\lambda_{M_2 P_L} M_0 \frac{P_L}{K_{M_2 P_L} + P_L}}_{M_0 \rightarrow M_2 \text{ by } P_L} - \underbrace{\lambda_{M I_\gamma} M_2 \frac{I_\gamma}{K_{M I_\gamma} + I_\gamma}}_{M_2 \rightarrow M_1 \text{ by } I_\gamma} - \underbrace{\lambda_{M I_\alpha} M_2 \frac{I_\alpha}{K_{M I_\alpha} + I_\alpha}}_{M_2 \rightarrow M_1 \text{ by } I_\alpha} \\ & + \underbrace{\lambda_{M I_\beta} M_1 \frac{I_\beta}{K_{M I_\beta} + I_\beta}}_{M_1 \rightarrow M_2 \text{ by } I_\beta} + \underbrace{\lambda_{M I_6} M_1 \frac{I_6}{K_{M I_6} + I_6}}_{M_1 \rightarrow M_2 \text{ by } I_6} - \underbrace{d_{M_2} M_2}_{\text{degradation}}. \end{aligned} \quad (2.27)$$

2.3.17 Equations for Naive and Activated NK Cells (K_0 and K)

Naive NK cells are activated by IL-2 [124, 125]. In addition, immature and mature DCs activate NK cells [126]. Thus, assuming a supply rate \mathcal{A}_{K_0} of naive NK cells, we have that

$$\frac{dK_0}{dt} = \underbrace{\mathcal{A}_{K_0}}_{\text{source}} - \underbrace{\lambda_{K I_2} K_0 \frac{I_2}{K_{K I_2} + I_2}}_{K_0 \rightarrow K \text{ by } I_2} - \underbrace{\lambda_{K D_0} K_0 \frac{D_0}{K_{K D_0} + D_0}}_{K_0 \rightarrow K \text{ by } D_0} - \underbrace{\lambda_{K D} K_0 \frac{D}{K_{K D} + D}}_{K_0 \rightarrow K \text{ by } D} - \underbrace{d_{K_0} K_0}_{\text{degradation}}, \quad (2.28)$$

$$\frac{dK}{dt} = \underbrace{\lambda_{K I_2} K_0 \frac{I_2}{K_{K I_2} + I_2}}_{K_0 \rightarrow K \text{ by } I_2} + \underbrace{\lambda_{K D_0} K_0 \frac{D_0}{K_{K D_0} + D_0}}_{K_0 \rightarrow K \text{ by } D_0} + \underbrace{\lambda_{K D} K_0 \frac{D}{K_{K D} + D}}_{K_0 \rightarrow K \text{ by } D} - \underbrace{d_K K}_{\text{degradation}}. \quad (2.29)$$

2.3.18 Equation for IL-2 (I_2)

IL-2 is produced by effector CD8+ T cells [127, 128] and Th1 cells [129], so that

$$\frac{dI_2}{dt} = \underbrace{\lambda_{I_2 T_8} T_8}_{\text{production by } T_8} + \underbrace{\lambda_{I_2 T_1} T_1}_{\text{production by } T_1} - \underbrace{d_{I_2} I_2}_{\text{degradation}}. \quad (2.30)$$

2.3.19 Equation for IFN- γ (I_γ)

IFN- γ is produced by effector CD8+ T cells [130] and Th1 cells [86, 131], with both expressions being inhibited by Tregs [132]. Furthermore, activated NK cells also produce IFN- γ [133]. Thus,

$$\frac{dI_\gamma}{dt} = \left(\underbrace{\lambda_{I_\gamma T_8} T_8}_{\text{production by } T_8} + \underbrace{\lambda_{I_\gamma T_1} T_1}_{\text{production by } T_1} \right) \underbrace{\frac{1}{1 + T_r / K_{I_\gamma T_r}}}_{\text{inhibition by } T_r} + \underbrace{\lambda_{I_\gamma K} K}_{\text{production by } K} - \underbrace{d_{I_\gamma} I_\gamma}_{\text{degradation}} . \quad (2.31)$$

2.3.20 Equation for TNF (I_α)

TNF is produced by effector CD8+ T cells [67, 134] and Th1 cells [135, 136], M1 macrophages [137], and activated NK cells [138, 139]. Hence,

$$\frac{dI_\alpha}{dt} = \underbrace{\lambda_{I_\alpha T_8} T_8}_{\text{production by } T_8} + \underbrace{\lambda_{I_\alpha T_1} T_1}_{\text{production by } T_1} + \underbrace{\lambda_{I_\alpha M_1} M_1}_{\text{production by } M_1} + \underbrace{\lambda_{I_\alpha K} K}_{\text{production by } K} - \underbrace{d_{I_\alpha} I_\alpha}_{\text{degradation}} .$$

2.3.21 Equation for TGF- β (I_β)

TGF- β is produced by viable cancer cells [140], effector Tregs [141] and CAFs [142]. Thus,

$$\frac{dI_\beta}{dt} = \underbrace{\lambda_{I_\beta C} C}_{\text{production by } C} + \underbrace{\lambda_{I_\beta T_r} T_r}_{\text{production by } T_r} + \underbrace{\lambda_{I_\beta C_F} C_F}_{\text{production by } C_F} - \underbrace{d_{I_\beta} I_\beta}_{\text{degradation}} . \quad (2.32)$$

2.3.22 Equation for IL-10 (I_{10})

IL-10 is produced by viable cancer cells [143, 144] and M2 macrophages [145, 146]. Additionally, effector Tregs secrete IL-10 [147] with IL-2 enhancing this production [148]. In particular, IL-2 binds to its cognate receptors and is rapidly internalised [149], which we account for using Michaelis-Menten kinetics. Hence,

$$\frac{dI_{10}}{dt} = \underbrace{\lambda_{I_{10} C} C}_{\text{production by } C} + \underbrace{\lambda_{I_{10} M_2} M_2}_{\text{production by } M_2} + \underbrace{\lambda_{I_{10} T_r} T_r \left(1 + \lambda_{I_{10} I_2} \frac{I_2}{K_{I_{10} I_2} + I_2} \right)}_{\text{production by } T_r \text{ enhanced by } I_2} - \underbrace{d_{I_{10}} I_{10}}_{\text{degradation}} . \quad (2.33)$$

2.3.23 Equation for IL-6 (I_6)

IL-6 is produced by mature DCs [150] and CAFs [151]. As such,

$$\frac{dI_6}{dt} = \underbrace{\lambda_{I_6 D} D}_{\text{production by } D} + \underbrace{\lambda_{I_6 C_F} C_F}_{\text{production by } C_F} - \underbrace{d_{I_6} I_6}_{\text{degradation}} . \quad (2.34)$$

2.3.24 Equation for PD-1 in the TS (P_D)

It is known that PD-1 is expressed on the surface of effector and exhausted CD8+ T cells [152–154], effector Th1 cells [155], effector Tregs [156], M2 macrophages [157, 158], and activated NK cells [159]. In the case where no pembrolizumab is administered, we assume that PD-1 expression is proportional to the concentration of the cell expressing it. For example, the total number of PD-1 molecules

expressed by effector Th1 cells in the TS is $\rho_{P_D^1} T_1$ for some constant $\rho_{P_D^1}$. If no pembrolizumab is present, then P_D simply follows

$$P_D = \rho_{P_D^8} T_8 + \rho_{P_D^{\text{ex}}} T_{\text{ex}} + \rho_{P_D^1} T_1 + \rho_{P_D^r} T_r + \rho_{P_D^{M_2}} M_2 + \rho_{P_D^K} K. \quad (2.35)$$

However, when pembrolizumab is injected, PD-1 on these PD-1-expressing cells can bind to pembrolizumab, causing their depletion [28] and, in turn, changing the number of PD-1 molecules expressed on each cell. We assume that the depletion of PD-1 follows principles analogous to the log-kill hypothesis for chemotherapeutic agents [160] so that the rate of depletion is proportional to the pembrolizumab concentration. Properly accounting for depletion, and denoting $d_{P_D A_1}$ as the rate at which PD-1 binds to pembrolizumab, leads to

$$\frac{dP_D}{dt} = P_D \underbrace{\left(\frac{\rho_{P_D^8} \frac{dT_8}{dt} + \rho_{P_D^{\text{ex}}} \frac{dT_{\text{ex}}}{dt} + \rho_{P_D^1} \frac{dT_1}{dt} + \rho_{P_D^r} \frac{dT_r}{dt} + \rho_{P_D^{M_2}} \frac{dM_2}{dt} + \rho_{P_D^K} \frac{dK}{dt} \right)}_{\text{surface expression}} - \underbrace{d_{P_D A_1} P_D A_1}_{\text{depletion by } A_1}. \quad (2.36)$$

A derivation of (2.36) can be found in [Appendix A](#).

2.3.25 Equations for PD-1 on effector T cells in the TDLN (P_D^{8LN} , P_D^{1LN} , and P_D^{rLN})

For simplicity, we assume that the number of PD-1 molecules on T cells in the TDLN is the same as for those in the TS. Thus, accounting for depletion as in (2.36), we have that

$$\frac{dP_D^{8LN}}{dt} = \underbrace{\frac{P_D^{8LN}}{T_A^8} \frac{dT_A^8}{dt}}_{\text{surface expression}} - \underbrace{d_{P_D^{8LN} A_1^{LN}} P_D^{8LN} A_1^{LN}}_{\text{depletion by } A_1^{LN}}, \quad (2.37)$$

$$\frac{dP_D^{1LN}}{dt} = \underbrace{\frac{P_D^{1LN}}{T_A^1} \frac{dT_A^1}{dt}}_{\text{surface expression}} - \underbrace{d_{P_D^{1LN} A_1^{LN}} P_D^{1LN} A_1^{LN}}_{\text{depletion by } A_1^{LN}}. \quad (2.38)$$

$$\frac{dP_D^{rLN}}{dt} = \underbrace{\frac{P_D^{rLN}}{T_A^r} \frac{dT_A^r}{dt}}_{\text{surface expression}} - \underbrace{d_{P_D^{rLN} A_1^{LN}} P_D^{rLN} A_1^{LN}}_{\text{depletion by } A_1^{LN}}. \quad (2.39)$$

2.3.26 Equations for PD-L1 in the TS (P_L^C and P_L)

We also know that PD-L1 is expressed on the surface of viable cancer cells [161], mature DCs [162], effector CD8+ T cells [163, 164], effector Th1 cells [165], effector Tregs [156], CAFs [166–168], and M2 macrophages [169]. Thus, we have that

$$P_L^C = \underbrace{\rho_{P_L^C} C}_{\text{surface expression}}, \quad (2.40)$$

$$P_L = \underbrace{\rho_{P_L^C} C + \rho_{P_L^D} D + \rho_{P_L^8} T_8 + \rho_{P_L^1} T_1 + \rho_{P_L^r} T_r + \rho_{P_L^{C_F}} C_F + \rho_{P_L^{M_2}} M_2}_{\text{surface expression}}, \quad (2.41)$$

2.3.27 Equation for PD-L1 in the TDLN (P_L^{LN})

For simplicity, we assume that the number of PD-L1 molecules on cells in the TDLN is the same as for those in the TS. As such,

$$P_L^{\text{LN}} = \underbrace{\rho_{P_L^D} D^{\text{LN}} + \rho_{P_L^8} T_A^8 + \rho_{P_L^1} T_A^1 + \rho_{P_L^r} T_A^r}_{\text{surface expression}}. \quad (2.42)$$

2.3.28 Equations for PD-1/PD-L1 Complex in the TDLN (Q^{8LN} , Q^{1LN} , and Q^{rLN})

In the TDLN, PD-L1 binds to PD-1 on the surfaces of effector CD8+ cells, effector Th1 cells, and effector Tregs, forming the PD-1/PD-L1 complex [170]. This formation is a reversible chemical process, and for simplicity, we assume that the association and dissociation rates are the same regardless of the cell expressing PD-1. We denote the association rate as $\alpha_{P_D^{\text{LN}} P_L^{\text{LN}}}$, and the dissociation rate as $d_{Q^{\text{LN}}}$. Considering Q^{8LN} as an example, we can express its formation and dissociation via the reaction $P_D^{\text{8LN}} + P_L^{\text{LN}} \xrightleftharpoons[d_{Q^{\text{8LN}}}{\alpha_{P_D^{\text{8LN}} P_L^{\text{LN}}}} Q^{\text{8LN}}$. Hence,

$$\frac{dQ^{\text{8LN}}}{dt} = \underbrace{\alpha_{P_D^{\text{8LN}} P_L^{\text{LN}}} P_D^{\text{8LN}} P_L^{\text{LN}}}_{\text{formation}} - \underbrace{d_{Q^{\text{8LN}}} Q^{\text{8LN}}}_{\text{dissociation}}. \quad (2.43)$$

Since the half-life of PD-1/PD-L1 is very small, being less than 1 second ($\approx 1.16 \times 10^{-5}$ days) [171], we employ a quasi-steady-state approximation (QSSA) for Q^{8LN} , so that $\frac{dQ^{\text{8LN}}}{dt} = 0 \implies \alpha_{P_D^{\text{8LN}} P_L^{\text{LN}}} P_D^{\text{8LN}} P_L^{\text{LN}} - d_{Q^{\text{8LN}}} Q^{\text{8LN}}$, or equivalently

$$Q^{\text{8LN}} = \frac{\alpha_{P_D^{\text{8LN}} P_L^{\text{LN}}}}{d_{Q^{\text{8LN}}}} P_D^{\text{8LN}} P_L^{\text{LN}}. \quad (2.44)$$

Similarly, we have that

$$Q^{\text{1LN}} = \frac{\alpha_{P_D^{\text{1LN}} P_L^{\text{LN}}}}{d_{Q^{\text{1LN}}}} P_D^{\text{1LN}} P_L^{\text{LN}}, \quad (2.45)$$

$$Q^{\text{rLN}} = \frac{\alpha_{P_D^{\text{rLN}} P_L^{\text{LN}}}}{d_{Q^{\text{rLN}}}} P_D^{\text{rLN}} P_L^{\text{LN}}. \quad (2.46)$$

2.3.29 Equations for Pembrolizumab (A_1 and A_1^{LN})

We assume that pembrolizumab is administered intravenously at a constant rate over a duration Δ_{pembro} at times t_1, t_2, \dots, t_n with doses $\xi_1, \xi_2, \dots, \xi_n$ respectively. We also account for depletion due to blocking PD-1 and the systemic nature of pembrolizumab distribution. It is important to note that the administered dose is not equal to the corresponding change in concentration in the TS or the TDLN. For simplicity, we assume linear pharmacokinetics so that, for some scaling factor f_{pembro} , we have that

$$\frac{dA_1}{dt} = \underbrace{\sum_{j=1}^n \xi_j f_{\text{pembro}} \frac{\theta(t - t_j) - \theta(t - t_j - \Delta_{\text{pembro}})}{\Delta_{\text{pembro}}}}_{\text{infusion}} - \underbrace{d_{A_1 P_D} A_1 P_D}_{\text{depletion from blocking } P_D} - \underbrace{d_{A_1} A_1}_{\text{degradation}}, \quad (2.47)$$

and

$$\frac{dA_1^{\text{LN}}}{dt} = \underbrace{\sum_{j=1}^n \xi_j f_{\text{pembro}} \frac{\theta(t-t_j) - \theta(t-t_j - \Delta_{\text{pembro}})}{\Delta_{\text{pembro}}}}_{\text{infusion}} - \underbrace{\sum_{i=8,1,r} d_{A_1^{\text{LN}} P_D^{\text{iLN}} A_1^{\text{LN}} P_D^{\text{iLN}}}}_{\text{depletion from blocking } P_D^{\text{iLN}}} - \underbrace{d_{A_1} A_1^{\text{LN}}}_{\text{degradation}}, \quad (2.48)$$

where $\theta(t)$ is the Heaviside function which equals 1 if $t \geq 0$, and 0 otherwise.

2.3.30 Model Reduction via QSSA

The model parameter values are estimated in [Appendix C](#) and are listed in [Table C.1](#).

We observe that the degradation rates of cytokines and DAMPs are, in general, order of magnitudes larger than those of immune and cancer cells. In particular, IL-2, IFN- γ , TNF, and TGF- β evolve on a very fast timescale, with degradation rates significantly higher than all other species in the model, causing them to equilibrate much more rapidly. As such, we perform a QSSA and reduce the model by setting (2.30) - (2.32) to 0 and solving for I_2 , I_γ , I_α , and I_β in terms of the other parameters and variables in the model. This minimally affects the system's evolution after a very short period of transient behaviour [172], and we justify this by observing that, empirically, the deviation in system trajectories remains negligible for nearby parameter choices. Performing the QSSA leads to

$$\frac{dI_2}{dt} = 0 \implies I_2 = \frac{1}{d_{I_2}} (\lambda_{I_2 T_8} T_8 + \lambda_{I_2 T_1} T_1), \quad (2.49)$$

$$\frac{dI_\gamma}{dt} = 0 \implies I_\gamma = \frac{1}{d_{I_\gamma}} \left[(\lambda_{I_\gamma T_8} T_8 + \lambda_{I_\gamma T_1} T_1) \frac{1}{1 + T_r / K_{I_\gamma T_r}} + \lambda_{I_\gamma K} K \right], \quad (2.50)$$

$$\frac{dI_\alpha}{dt} = 0 \implies I_\alpha = \frac{1}{d_{I_\alpha}} (\lambda_{I_\alpha T_8} T_8 + \lambda_{I_\alpha T_1} T_1 + \lambda_{I_\alpha M_1} M_1 + \lambda_{I_\alpha K} K), \quad (2.51)$$

$$\frac{dI_\beta}{dt} = 0 \implies I_\beta = \frac{1}{d_{I_\beta}} (\lambda_{I_\beta C} C + \lambda_{I_\beta T_r} T_r + \lambda_{I_\beta C_F} C_F). \quad (2.52)$$

We note that this reduction is valid since the timescale of IFN- γ , the slowest of the ‘‘fast’’ species, is significantly shorter than the timescales of all ‘‘slow’’ species in the model.

3 Steady States and Initial Conditions

We estimated all initial conditions and steady states under the assumption that pembrolizumab has not been and will not be administered. We assumed that the patient initially has stage IIIA or stage IIIB MSI-H/dMMR colorectal adenocarcinoma with metastasis to at least one lymph node.

3.1 Tumour Site Cell Steady States and Initial Conditions

Digital cytometry has proved itself to be a powerful technique in characterising immune cell populations from individual patients' bulk tissue transcriptomes without requiring physical cell isolation [173–177]. In particular, RNA-sequencing (RNA-seq) deconvolution of tumour gene expressions has been very useful in determining immune profiles and adjusting treatment accordingly.

Using the UCSC Xena web portal [178], RSEM normalised RNA-seq gene expression profiles of patients from the TCGA COAD and TCGA READ projects [45] were acquired, featuring patients with

colorectal adenocarcinomas. Corresponding clinical and biospecimen data were downloaded from the GDC portal [179] and included tumour dimensions, necrotic cell percentage, AJCC TNM stage, and MSIsensor and MANTIS MSI statuses. We filtered for samples from primary tumours and with non-empty necrosis percentage data from patients with AJCC stage III or stage IV CRC, and at least one of MANTIS score > 0.4 or MSIsensor score $> 3.5\%$, as these are the default thresholds for MSI-H [180]. We used the stage IIIC samples to infer steady states and the stage IIIA and stage IIIB samples to infer initial conditions. For all algorithms outlined in the sequel, we aggregated the estimates by taking the median of the relevant non-zero values elementwise and then normalising such that their sums become 1. We also used the manually curated TIMEDB cell composition database [181] to source tumour deconvolution estimates for each relevant individual sample.

To estimate immune cell population proportions in locally advanced MSI-H/dMMR CRC, we applied multiple algorithms and then synthesised their results to obtain estimates for all cell types in the model. We first used the ImmuCellAI algorithm [182], which estimates the abundance of 24 immune cell types from gene expression data and has also been shown to be highly accurate in predicting immunotherapy response. These immune cell types include 18 T cell subsets, including CD4+ T cells which incorporate T helper cells (namely Th1 cells, Th2 cells, Th17 cells, and T follicular helper cells), regulatory T cells (including natural Tregs (nTregs), induced Tregs (iTregs), and type 1 regulatory T cells (Tr1s)), naive CD4+ T cells (CD4_naive) and other CD4+ T cells (CD4_T). In addition, they include naive CD8+ T cells (CD8_T), cytotoxic T cells or CTLs (Tc), exhausted CD8+ T cells (Tex) cells, central memory T cells (Tcm), effector memory T cells (Tem), natural killer T cells (NKT), $\gamma\delta$ T cells (Tgd), and mucosal-associated invariant T cells (MAIT). ImmuCellAI also estimates the abundance of DCs, B cells, monocytes, macrophages, NK cells, and neutrophils. Direct correspondences between state variables in the model and ImmuCellAI cell types are shown in Table B.1. Additionally, the aggregated estimated cell proportions generated by ImmuCellAI for steady states and initial conditions, after normalisation, are shown in Table B.2 and Table B.3.

To determine the proportions of D_0 and D , K_0 and K , M_0 and M_1 and M_2 , we used the CIBERSORTx algorithm [173], due to its high accuracy [183]. We followed a similar approach to [44] and [46] and applied CIBERSORTx B-mode on the refined gene expression data, using the validated LM22 signature matrix [177], which gave relative immune cell proportions of 22 immune cell types using 547 signature genes derived from microarray data. Direct correspondences between state variables in the model and keys of the LM22 signature matrix are shown in Table B.4. The aggregated estimated cell proportions generated by CIBERSORTx for steady states and initial conditions, after normalisation, are shown in Table B.5 and Table B.6.

However, to determine the proportions of K_0 and K at steady state, we could not use CIBERSORTx due to its nil results. Instead, we used a combination of biologically informed assumptions and data from physical experiments. It was determined in [184] that the ratio of the proportions of cytotoxic, activated NK cells to naive NK cells decreases as CRC progresses. We thus assumed that $\bar{K} = 10\bar{K}_0$.

We integrated the relative proportions within cell types for DCs, NK cells, and macrophages outputted by CIBERSORTx into the ImmuCellAI abundance estimates. We note that the density of immune cells in a healthy adult colon is approximately 3.37×10^7 cell/g [185], which assuming a tissue density of 1.03 g/cm³, results in a total immune cell density of 3.47×10^7 cell/cm³. However, advanced cancer induces lymphadenopathy [186, 187], which [185] estimates results in an increase in the total number of lymphocytes of at most 10%. As such, we assume that there is a 10% increase in lymphocyte concentration in locally advanced MSI-H/dMMR CRC.

To determine the densities of CAFs, which are considered to be essentially all fibroblasts in the TME [60], we used MCP-counter [188]. MCP-counter uses a gene expression matrix to estimate the sample relative abundance of eight immune and two stromal cell populations in the TME from gene expression data and is amongst the highest accuracy and specificity estimation methods available [189]. The aggregated estimated cell proportions generated by MCP-counter for steady states and initial conditions, after normalisation, are shown in Table B.7 and Table B.8. To estimate CAF densities at steady state and to choose its initial condition, we assumed that the ratio of all immune cells (that is, cells excluding endothelial cells and fibroblasts) to fibroblasts given by MCP-counter is the ratio of immune cells to fibroblasts in the TME.

Accounting for the high immunogenicity of tumours in locally advanced MSI-H/dMMR CRC [190], we assumed at steady state that the density of cancer cells is equal to the total immune cell density, excluding fibroblasts. From the TCGA biospecimen data, the median necrotic cancer cell percentage for stage IIIA and stage IIIC MSI-H CRC samples is 10%. As such, denoting TIC as the total immune cell density, and N_p as the necrotic cell percentage, we have that

$$C + N_c = \text{TIC}, \tag{3.1}$$

$$\frac{N_c}{N_p} = \frac{C}{1 - N_p}, \quad C = \text{TIC} \times (1 - N_p) \implies N_c = \text{TIC} \times N_p. \tag{3.2}$$

Taking into account lymphadenopathy and using data from [185], we assumed that the total immune cell density in locally advanced MSI-H/dMMR CRC initially is approximately 3.72×10^7 cell/cm³ and at steady state is approximately 3.68×10^7 cell/cm³. Thus, at steady state $C \approx 3.31 \times 10^7$ cell/cm³ and $N_c \approx 3.68 \times 10^6$ cell/cm³.

A retrospective cohort study by Burke et al. considered CRC patients at Leeds Teaching Hospitals NHS Trust over a 2-year interval who received no treatment and who underwent CT twice more than 5 weeks apart. It was found that in patients whose M category changed from M0 to M1, the median interval between CTs was 155 days, and the median tumour doubling time was 172 days [191]. We assumed that these timeframes are similar to stage IIIA/IIIB MSI-H/dMMR CRC progression, and, as such, we assume that it takes 155 days for C and N_c to reach their steady-state values. This corresponds to an initial condition for C being $C(0) = 1.79 \times 10^7$ cell/cm³ and thus $N_c(0) \approx 1.99 \times 10^6$ cell/cm³.

Combining everything, the resultant steady states and initial conditions for the model are shown in Table 2 and Table 3.

Table 2: TS steady-state cell densities for the model, combining estimates derived from ImmuCellAI, CIBERSORTx, and MCP-counter. All values are in cell/cm³.

C	N_c	D_0	D	T_8	T_{ex}	T_1
3.31×10^7	3.68×10^6	1.46×10^6	4.78×10^5	1.78×10^5	1.40×10^5	7.23×10^4
T_r	C_F	M_0	M_1	M_2	K_0	K
1.45×10^5	2.56×10^7	5.16×10^5	4.14×10^5	1.60×10^6	4.82×10^5	4.82×10^6

Table 3: TS initial conditions for the model, combining estimates derived from ImmuCellAI, CIBERSORTx, and MCP-counter. All values are in cell/cm³.

C	N_c	D_0	D	T_8	T_{ex}	T_1
1.79×10^7	1.99×10^6	1.63×10^6	8.29×10^5	2.43×10^5	2.09×10^5	1.04×10^5
T_r	C_F	M_0	M_1	M_2	K_0	K
2.12×10^5	2.00×10^7	6.67×10^5	6.61×10^5	1.23×10^6	3.06×10^5	5.20×10^6

3.2 TDLN Cell Steady States and Initial Conditions

To determine the initial conditions and steady-state values for T_0^8 , T_A^8 , T_0^4 , T_A^1 , and T_A^r , we used ImmuCellAI on the GSE26571 dataset from the NCBI Gene Expression Omnibus repository [192, 193], obtaining deconvolution results from TIMEDB. This contains nine samples of lymph node metastases from 7 patients with colon adenocarcinoma, with data from [194]. However, the dataset’s metadata does not contain AJCC TNM stages for patients. To estimate the TNM stages of the patients with lymph node metastases, noting that lymph node metastases guarantee a TNM stage of at least stage IIIA, we considered the samples of the primary tumour for these patients and apply the ImmuCellAI algorithm to estimate their immune cell abundances, ignoring Tcm and Tem cell subtypes. Mappings between ImmuCellAI immune cell types and TDLN cell types in the model are shown in Table B.9.

We categorised patients as being in stage IIA or stage IIIB if their lymph node metastases were well or moderately differentiated and categorised patients as being in stage IIIC if their lymph node metastases were poorly differentiated, noting that poorer differentiation is correlated with more advanced disease staging in CRC [195]. Like before, we used lymph node metastases from stage IIIC patients to infer TDLN steady states and the stage IIIA/IIIB samples to infer initial conditions. Aggregating the estimates, as before, and then normalising such that their sums become 1, results in the proportions as shown in Table B.10 and Table B.11.

The density of immune cells in the lymph nodes of an adult is approximately 1.8×10^9 cell/g [185], which assuming a tissue density of 1.03 g/cm³, results in a total immune cell density of 1.854×10^9 cell/cm³. Finally, we assumed that in the TDLN, the number of activated CD8+ T cells having undergone n_{max}^8 divisions is roughly half the number which has only undergone $n_{\text{max}}^8 - 1$ divisions and so forth. Furthermore, we assumed that initially, and at steady state, 10% of all Tregs are naive. Thus, we assume that for $i = 1, 8$,

$$T_A^i = \frac{2^{n_{\text{max}}^i}}{2^{n_{\text{max}}^i+1} - 1} T_A^{i\text{LN}},$$

and that

$$T_0^r = \frac{T_A^{r\text{LN}}}{10}, \quad T_A^r = \frac{9}{10} \frac{2^{n_{\text{max}}^r}}{2^{n_{\text{max}}^r+1} - 1} T_A^{r\text{LN}},$$

where $T_A^{i\text{LN}}$ is the total number of activated T cells in the TDLN of the corresponding type.

Combining everything, the resultant steady states and initial conditions for the model are shown in Table 4 and Table 5.

Table 4: TDLN steady-state cell densities for the model, using estimates derived from ImmuCellAI. All values are in cell/cm³.

T_0^8	T_A^8	T_0^4	T_A^1	T_0^r	T_A^r
1.15×10^7	1.20×10^6	6.64×10^6	5.74×10^6	1.06×10^6	4.79×10^6

Table 5: TDLN initial conditions for the model, using estimates derived from ImmuCellAI. All values are in cell/cm³.

T_0^8	T_A^8	T_0^4	T_A^1	T_0^r	T_A^r
1.18×10^7	8.47×10^5	5.08×10^6	7.61×10^6	1.70×10^5	7.69×10^5

To estimate the steady states and initial conditions for D^{LN} , we considered (2.7) at steady state, which led to

$$\frac{V_{\text{TS}}}{V_{\text{LN}}} \lambda_{D^{\text{DLN}}} e^{-d_D \tau_m} \bar{D} - d_D \bar{D}^{\text{LN}} = 0 \implies \bar{D}^{\text{LN}} = \frac{V_{\text{TS}} \lambda_{D^{\text{DLN}}} e^{-d_D \tau_m} \bar{D}}{V_{\text{LN}} d_D} = 6.04 \times 10^6 \text{ cell/cm}^3,$$

where we acquired the value of \bar{D} from Table 2. We set the initial condition for D^{LN} to be such that $D^{\text{LN}}(0)/\bar{D}^{\text{LN}} = D(0)/\bar{D} \implies D^{\text{LN}}(0) = 1.05 \times 10^7 \text{ cell/cm}^3$.

3.3 DAMP Steady States and Initial Conditions

We chose the DAMP steady states and initial conditions to be as in Table 6. Justification for the choice of these values is done in Appendix C.1.

Table 6: DAMP steady states and initial conditions for the model. All values are in units of g/cm³.

DAMP	Steady State	Initial Condition
H	1.01×10^{-8}	5.76×10^{-9}
S	4.50×10^{-8}	2.00×10^{-8}

3.4 Cytokine Steady States and Initial Conditions

We chose the cytokine steady states and initial conditions to be as in Table 7. Justification for the choice of these values is done in Appendix C.2.

Table 7: Cytokine steady states and initial conditions for the model. All values are in units of g/cm³.

Cytokine	Steady State	Initial Condition
I_2	2.00×10^{-12}	2.81×10^{-12}
I_γ	1.69×10^{-11}	1.82×10^{-11}
I_α	5.30×10^{-11}	5.85×10^{-11}
I_β	1.51×10^{-6}	1.05×10^{-6}
I_{10}	1.15×10^{-10}	4.60×10^{-11}
I_6	3.12×10^{-6}	3.64×10^{-6}

3.5 Immune Checkpoint Protein Steady States and Initial Conditions

We chose the immune checkpoint protein steady states and initial conditions to be as in [Table 8](#). Justification for the choice of these values is done in [Appendix C.3](#).

Table 8: Immune checkpoint protein steady states and initial conditions for the model. All values are in units of molec/cm³.

Protein	Steady State	Initial Condition
P_D	7.88×10^9	8.88×10^9
P_D^{8LN}	3.31×10^9	2.34×10^9
P_D^{1LN}	1.18×10^{10}	1.56×10^{10}
P_D^{rLN}	9.82×10^9	1.58×10^9
P_L^C	5.53×10^{10}	2.99×10^{10}
P_L	1.39×10^{11}	1.04×10^{11}
P_L^{LN}	1.30×10^{11}	2.05×10^{11}
Q^{8LN}	9.20×10^4	1.02×10^5
Q^{1LN}	3.27×10^5	6.79×10^5
Q^{rLN}	2.73×10^5	6.88×10^4

4 Results

We now aim to optimise neoadjuvant pembrolizumab therapy for locally advanced MSI-H/dMMR CRC. For simplicity, we assume that pembrolizumab is given at a constant dosage, and the spacing between consecutive pembrolizumab infusions is constant. We also assume that the patient has pembrolizumab at $t = 0$ days, and we consider a treatment regimen lasting for 12 weeks so that the time for the latest allowed infusion is $t = 84$ days, and simulate to 24 weeks = 168 days. In our optimisation of pembrolizumab therapy, we consider the following four endpoints: tumour concentration reduction (TCR), efficacy, efficiency, and toxicity.

We define $V(t) = C(t) + N_c(t)$ as the total cancer concentration at time t without treatment, and define $V(\xi_{\text{pembro}}; \eta_{\text{pembro}}, t) = C(\xi_{\text{pembro}}; \eta_{\text{pembro}}, t) + N_c(\xi_{\text{pembro}}; \eta_{\text{pembro}}, t)$ as the total cancer concentration at time t with treatment with pembrolizumab doses of ξ_{pembro} at a dosing interval of η_{pembro} . We define the TCR from this regimen to be

$$\text{TCR}(\xi_{\text{pembro}}; \eta_{\text{pembro}}, t) := \frac{V(0) - V(\xi_{\text{pembro}}; \eta_{\text{pembro}}, t)}{V(0)} \times 100\%. \quad (4.1)$$

We also define the efficacy similarly as

$$\text{efficacy}(\xi_{\text{pembro}}; \eta_{\text{pembro}}, t) := \frac{V(t) - V(\xi_{\text{pembro}}; \eta_{\text{pembro}}, t)}{V(t)} \times 100\%. \quad (4.2)$$

In particular, the efficacy represents the extent of tumour density shrinkage throughout its growth course in comparison to no treatment, whereas the TCR reveals how much the tumour density has reduced since the commencement of treatment. We see that the TCR and efficacy are linearly related, so that an increase in treatment efficacy results in increased TCR, and vice-versa, via the formula

$$\text{efficacy}(\xi_{\text{pembro}}; \eta_{\text{pembro}}, t) = \left(1 - \frac{V(0)}{V(t)}\right) \times 100\% + \frac{V(0)}{V(t)} \times \text{TCR}(\xi_{\text{pembro}}; \eta_{\text{pembro}}, t). \quad (4.3)$$

We can also consider the efficiency of the treatment regimen, with a dosing interval of η_{pembro} and dosage ξ_{pembro} given by

$$\text{efficiency}(\xi_{\text{pembro}}; \eta_{\text{pembro}}, t) := \frac{\text{TCR}(\xi_{\text{pembro}}; \eta_{\text{pembro}}, t)}{\xi_{\text{pembro}} (1 + \lfloor \min(t, 84) / \eta_{\text{pembro}} \rfloor)}, \quad (4.4)$$

where $\xi_{\text{pembro}} (1 + \lfloor \min(t, 84) / \eta_{\text{pembro}} \rfloor)$ is the total dose of pembrolizumab administered by time t . This corresponds to the ratio between the TCR percentage and the total dose of pembrolizumab administered.

Finally, we can define the toxicity of the treatment regimen, noting that large enough pembrolizumab concentrations can potentially cause hepatotoxicity and ocular toxicity [196, 197], as well as increase the probability of serious infections and malignancies. Experiments show that dosages of pembrolizumab between 0.1 mg/kg and 10 mg/kg, given every 2 weeks, is safe and tolerable [198, 199]. We thus assume that the threshold for pembrolizumab toxicity is 10 mg/kg every 2 weeks, with higher doses being deemed toxic. To rigorise this notion, we define the toxicity of the treatment regimen, with dose interval η_{pembro} and dosage ξ_{pembro} , as

$$\text{toxicity}(\xi_{\text{pembro}}; \eta_{\text{pembro}}, t) := \max \left(\frac{\max_{s \in [0, t]} A_1(\xi_{\text{pembro}}; \eta_{\text{pembro}}, s)}{\max_{s \in [0, t]} A_1(800 \text{ mg}; 14 \text{ days}, s)}, \frac{\max_{s \in [0, t]} A_1^{\text{LN}}(\xi_{\text{pembro}}; \eta_{\text{pembro}}, s)}{\max_{s \in [0, t]} A_1^{\text{LN}}(800 \text{ mg}; 14 \text{ days}, s)} \right). \quad (4.5)$$

In particular, $A_1(\xi_{\text{pembro}}; \eta_{\text{pembro}}, s)$ and $A_1^{\text{LN}}(\xi_{\text{pembro}}; \eta_{\text{pembro}}, s)$ denote the concentrations of A_1 and A_1^{LN} at time s , with pembrolizumab doses of ξ_{pembro} at a dosing interval of η_{pembro} , respectively, noting that we assume a patient mass of 80 kg. In particular, the toxicity quantifies the ratio of the maximum pembrolizumab concentrations from the regimen to those of a 10 mg/kg dose given every 2 weeks, taking the highest value of this ratio between the TDLN and TS. A toxicity greater than 1 indicates a toxic and unsafe regimen, whereas a toxicity of 1 or less signifies a non-toxic and safe regimen, with lower toxicity values corresponding to safer treatments.

It is beneficial for us to consider FDA-approved pembrolizumab regimens for the first-line treatment of metastatic MSI-H/dMMR CRC as a benchmark for comparison. There are two distinct treatment regimens for pembrolizumab therapy that are approved by the FDA for metastatic MSI-H/dMMR CRC in adults [200]:

- Treatment 1: 200 mg of pembrolizumab administered by intravenous infusion over a duration of 30 minutes every 3 weeks until disease progression or unacceptable toxicity.
- Treatment 2: 400 mg of pembrolizumab administered by intravenous infusion over a duration of 30 minutes every 6 weeks until disease progression or unacceptable toxicity.

These correspond to the following parameter values in the model:

- Treatment 1: $\xi_j = 200 \text{ mg}$, $t_j = 21(j - 1)$, $n = 5$, $\Delta_{\text{pembro}} = 2.08 \times 10^{-2} \text{ day}$,
- Treatment 2: $\xi_j = 400 \text{ mg}$, $t_j = 42(j - 1)$, $n = 3$, $\Delta_{\text{pembro}} = 2.08 \times 10^{-2} \text{ day}$.

Furthermore, this corresponds to a dose of 2.5 mg/kg (5 mg/kg) of pembrolizumab being administered in Treatment 1(2), assuming a patient mass of 80 kg.

Denoting the dosing interval of pembrolizumab as η_{pembro} , we perform a sweep across the space $\eta_{\text{pembro}} \in \{1, 2, 3, 4, 6, 7, 12, 14, 21, 28, 42, 84, \infty\}$ days, where $\eta_{\text{pembro}} = \infty$ days denotes a single dose of treatment, given at $t = 0$ days. These values are integer factors of 84 days, and each η_{pembro} corresponds to a distinct number of doses administered. This approach ensures practicality whilst preventing any artefacts that could occur from selecting a treatment regimen that ends at a fixed time of 12 weeks. We consider linearly spaced dosages in the domain $\xi_{\text{pembro}} \in [1 \text{ mg/kg}, 10 \text{ mg/kg}]$, corresponding to $\xi_{\text{pembro}} \in [80 \text{ mg}, 800 \text{ mg}]$, assuming a patient mass of 80 kg, with an increment of 1 mg. We also assume, as with Treatments 1 and 2, that pembrolizumab is administered as an intravenous infusion over a duration of 30 minutes, so that $\Delta_{\text{pembro}} = 2.08 \times 10^{-2}$ day.

Heatmaps of TCR, efficacy, efficiency, and toxicity at $t = 24$ weeks for these η_{pembro} and ξ_{pembro} values are shown in Fig 1. All simulations were done in MATLAB using the dde23 solver with the initial conditions stated in Section 3 and drug parameters as above.

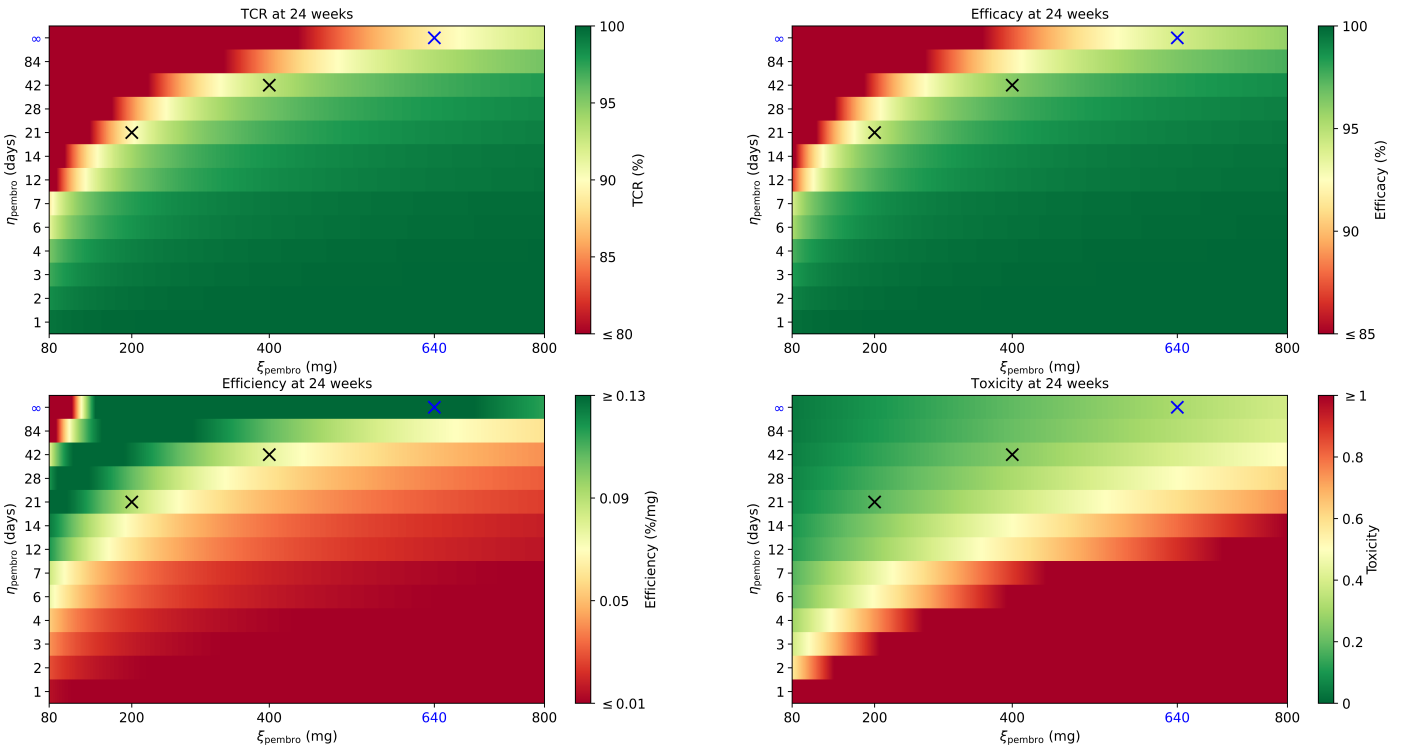


Fig 1: TCR (top left), efficacy (top right), efficiency (bottom left), and toxicity (bottom right) at 24 weeks for η_{pembro} in the domain $\{1, 2, 3, 4, 6, 7, 12, 14, 21, 28, 42, 84, \infty\}$ days. We sweep across linearly spaced ξ_{pembro} dosages between 80 mg and 800 mg with an increment of 1 mg. The FDA-approved regimens (Treatment 1 and Treatment 2) for metastatic MSI-H/dMMR CRC are shown in black, and the optimal treatment regimen for locally advanced MSI-H/dMMR CRC is shown in blue.

We can determine the optimal pembrolizumab therapy by considering the regimen that achieves an acceptable TCR at 24 weeks whilst maximising treatment efficiency as much as possible and ensuring a toxicity of less than 1. The TCR of Treatment 1 at 24 weeks was calculated to be 89.68%, and the TCR of Treatment 2 at 24 weeks was calculated to be 92.98%. As such, to ensure that the TCR of the optimal treatment is comparable to current FDA-approved pembrolizumab regimens, we set the threshold TCR to be 89%. We also consider constraints due to practicality, so that $\eta_{\text{pembro}}^{\text{opt}} \in \{7, 14, 21, 28, 42, 84, \infty\}$ days, so that the pembrolizumab dose intervals are an integer number of weeks. We also constrain that $\eta_{\text{pembro}}^{\text{opt}}$ is an integer multiple of 0.1 mg/kg, corresponding to an integer multiple

of 8 mg. Denoting the space of $(\xi_{\text{pembro}}, \eta_{\text{pembro}})$ pairs that satisfy these criteria as $\mathcal{S}^{\text{prac}}$, the optimal pembrolizumab dosing and spacing, denoted $\xi_{\text{pembro}}^{\text{opt}}$ and $\eta_{\text{pembro}}^{\text{opt}}$, satisfy

$$(\xi_{\text{pembro}}^{\text{opt}}, \eta_{\text{pembro}}^{\text{opt}}) = \underset{\substack{\text{TCR}(\xi_{\text{pembro}}; \eta_{\text{pembro}}, 168) \geq 89\% \\ (\xi_{\text{pembro}}, \eta_{\text{pembro}}) \in \mathcal{S}^{\text{prac}} \\ \text{toxicity}(\xi_{\text{pembro}}; \eta_{\text{pembro}}, 168) \leq 1}}{\text{argmax}} \text{efficiency}(\xi_{\text{pembro}}; \eta_{\text{pembro}}, 168). \quad (4.6)$$

Solving (4.6) leads to the optimal therapy occurring when $\xi_{\text{pembro}}^{\text{opt}} = 640$ mg and $\eta_{\text{pembro}}^{\text{opt}} = \infty$ days. This corresponds to a single dose of 640 mg, corresponding to 8 mg/kg, and results in a TCR of 89.06%, an efficacy of 94.09%, an efficiency of $1.39 \times 10^{-1}\%$ /mg, and a toxicity of 3.11×10^{-1} at 24 weeks. Time traces of TCR, efficacy, efficiency, and toxicity for Treatment 1, Treatment 2, and the optimal treatment are shown in Fig 2.

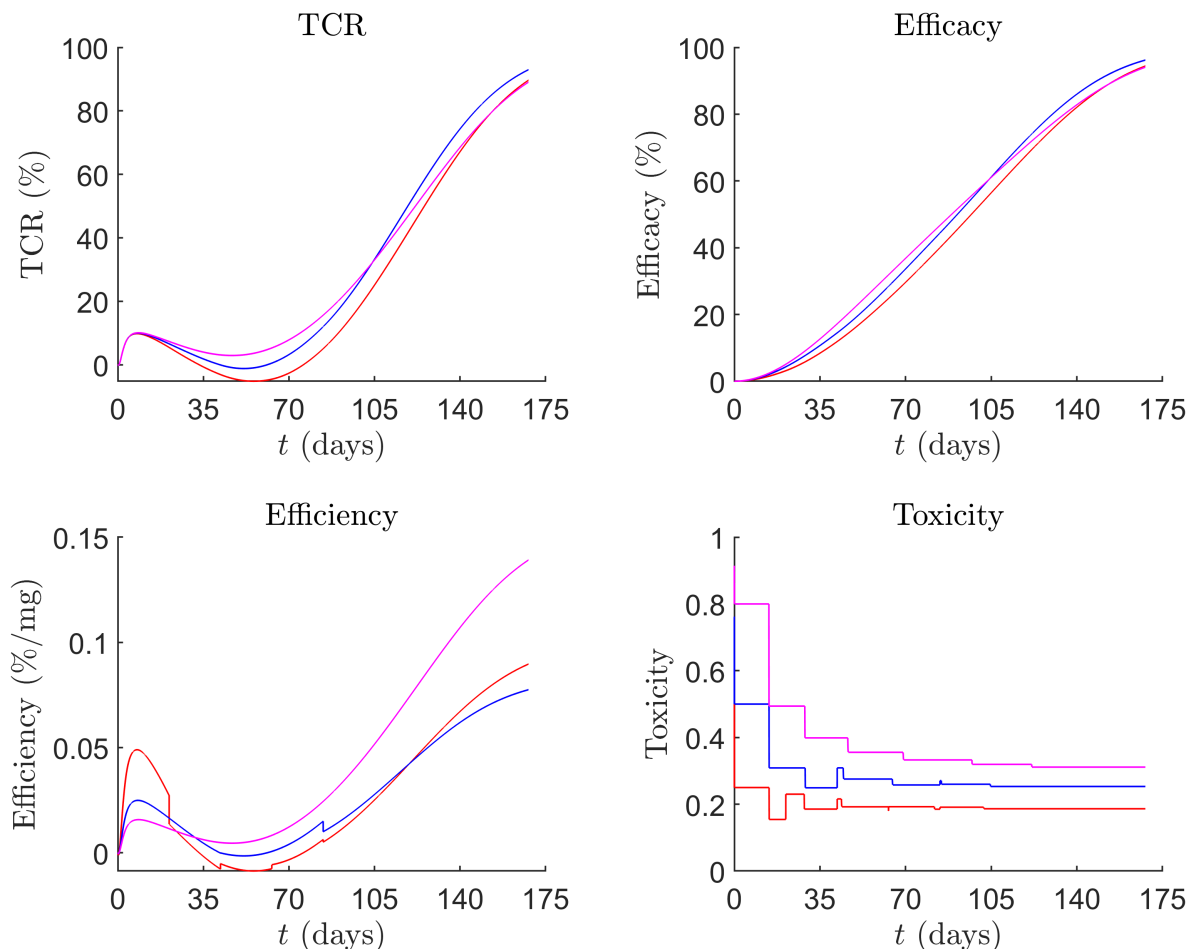


Fig 2: Time traces of TCR (top left), efficacy (top right), efficiency (bottom left), and toxicity (bottom right) for Treatment 1 (in red), Treatment 2 (in blue), and the optimal pembrolizumab treatment regimen for locally advanced MSI-H/dMMR CRC (in magenta).

Time traces for total cancer concentration (V) under optimal pembrolizumab therapy, compared to Treatments 1 and 2 and no treatment, are shown in Fig 3. We can also compare the effect of optimal pembrolizumab therapy against Treatments 1 and 2, as well as no treatment, on the TME, with time traces of key variables shown in Fig 4. The results from Fig 1, Fig 2, Fig 3, and Fig 4 will be discussed in detail in Section 5.

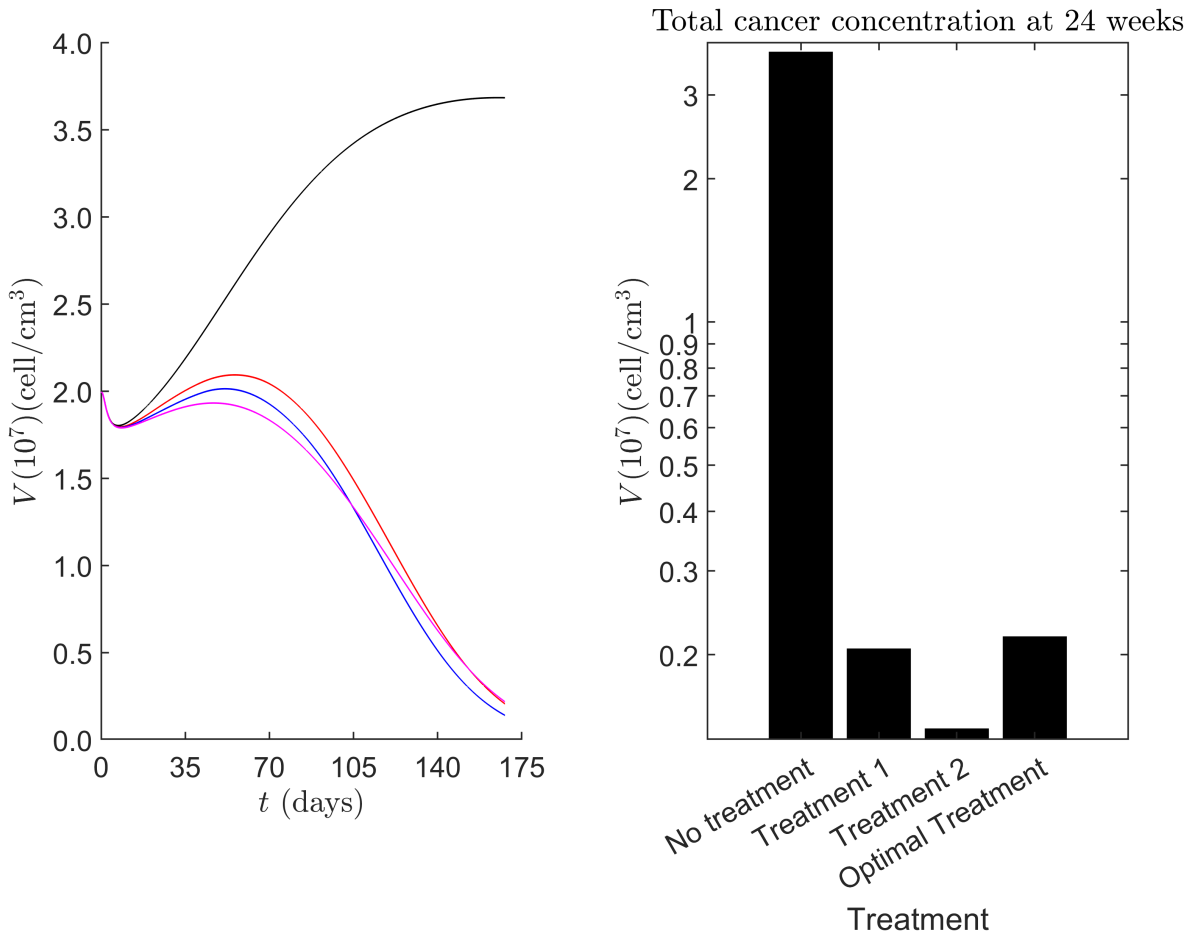


Fig 3: Left: time traces of V up to 24 weeks from commencement, with no treatment in black, Treatment 1 in red, Treatment 2 in blue, and the optimal pembrolizumab treatment regimen for locally advanced MSI-H/dMMR CRC in magenta. Right: concentration of V , 24 weeks after pembrolizumab treatment commencement.

5 Discussion

We can see from Fig 2, Fig 3, and Fig 4 that Treatments 1 and 2 are highly effective in eradicating cancer cells. Without treatment, the total cancer cell concentration (including necrotic cancer cells) at 24 weeks equals 3.68×10^7 cell/cm³, however, equals 2.05×10^6 cell/cm³, and 1.40×10^6 cell/cm³ with Treatments 1 and 2 respectively. This corresponds to an efficacy of 94.42% and 96.21% for Treatments 1 and 2, respectively. In particular, this leads to two immediate, but important, observations. We must note that when comparing pembrolizumab, we must ensure that we take into account that locally advanced MSI-H/dMMR CRC patients will not have been treated with chemotherapy/other therapies and that these drugs are given as a first-line treatment. Firstly, higher doses at larger intervals are comparable but slightly more effective than smaller doses at shorter intervals, which is consistent with clinical and experimental observations for other cancers [38, 201]. It is difficult to compare our results to that of pre-existing clinical trials for locally advanced MSI-H/dMMR CRC due to the lack of time-series data, widely varying treatment regimens tested, and the broad range of outcomes found. Focusing on Treatment 1, which appears to be the primary focus of ongoing clinical trials, a tumour concentration reduction of 89.68% at 24 weeks, following the cessation of treatment at 12 weeks, is consistent with the extent of response observed. Therefore, we consider the model to be accurate; however, additional experimental data is needed for further verification. We also observed that slight

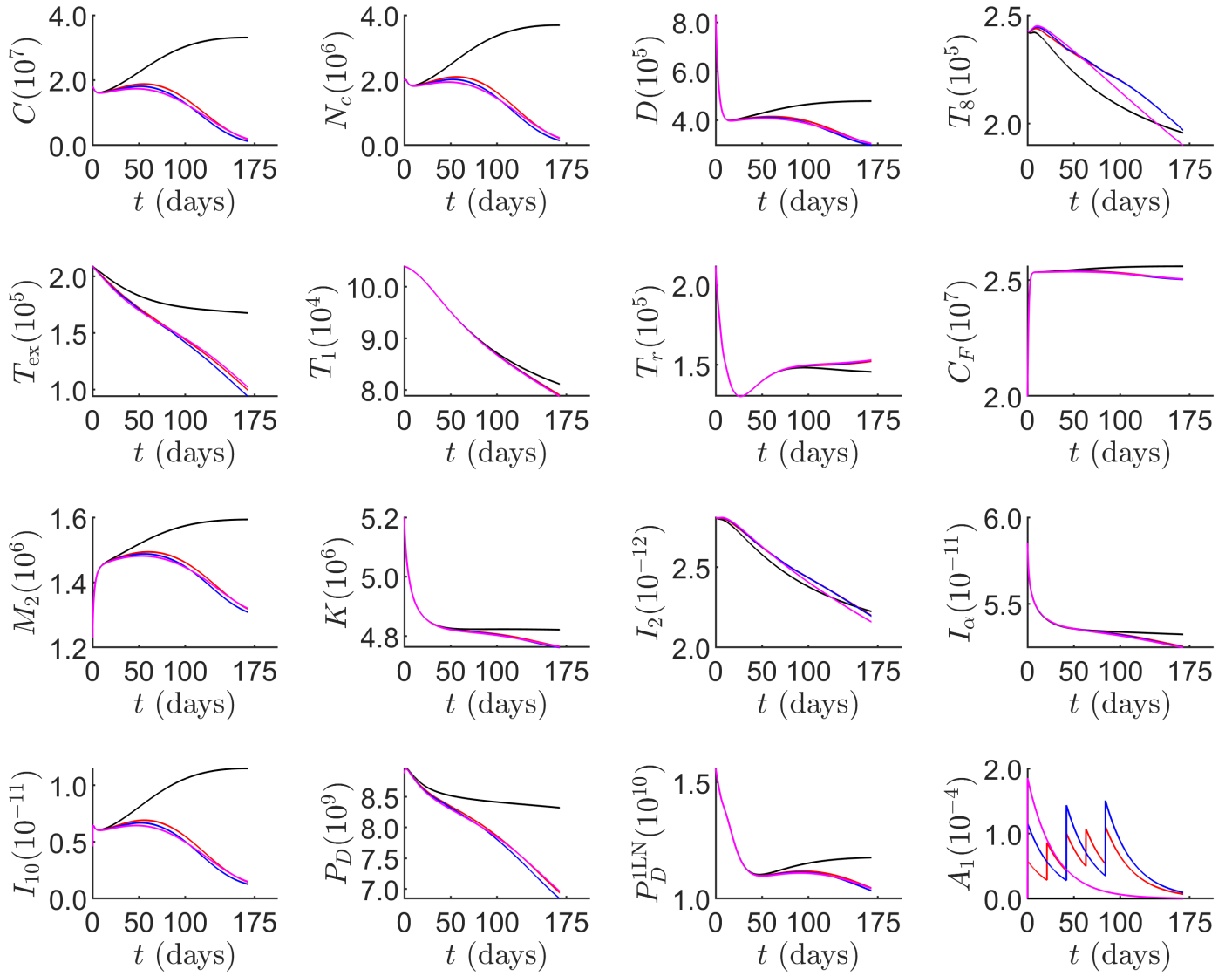


Fig 4: Time traces of notable variables in the model, with the units of the variables as in Table 1. Time traces with no treatment are in black, Treatment 1 in red, Treatment 2 in blue, and the optimal pembrolizumab treatment regimen for locally advanced MSI-H/dMMR CRC in magenta.

variations in the initial conditions had minimal impact on model trajectories after a few days and that reasonable choices of initial conditions did not lead to negativity for any model variables (not shown). Moreover, it takes a couple of months for pembrolizumab to begin showing effects and for tumour reductions to be observed, in agreement with experimental findings for CRC [19].

Furthermore, by analysing immune cell trajectories from Fig 4, offering potential explanations for behaviour in the TME and identifying key factors that contribute to maximising cancer reduction. One of the most important observations is that with pembrolizumab, the concentration of effector CD8+ T cells increases greatly compared to without treatment, with the exhausted CD8+ T cell concentration decreasing correspondingly. In particular, the concentration of exhausted CD8+ T cells without treatment at 24 weeks is 1.68×10^5 cell/cm³ compared to 9.96×10^4 cell/cm³, 9.41×10^4 cell/cm³, and 1.02×10^5 cell/cm³ with Treatments 1 and 2, and the optimal treatment respectively. This showcases that a) pembrolizumab increases the concentration of cytotoxic CD8+ T cells through re-invigorating exhausted CD8+ T cells, and b) the concentration of exhausted CD8+ T cells plays a major role in

treatment efficacy, as a reduction in exhausted T cells results in decreased PD-1 concentrations and improved cancer eradication.

One important thing to note is that the effector CD8+ T cell population for the optimal regimen drops significantly after a couple of months, and is only 1.90×10^5 cell/cm³ at 24 weeks, despite having the largest effector CD8+ T cell population initially. This occurs since the pembrolizumab concentration in the TS and TDLN gradually declines after the initial infusion so that reinvigoration of exhausted CD8+ T cells diminishes after a few months. However, the optimal therapy eradicates the tumour most rapidly, reducing the viable and necrotic cancer cell population to very low levels, eventually resulting in decreased DAMP release and a reduced influx of effector CD8+ T cells from the TDLN. Despite this, a sufficient number of effector CD8+ T cells and other cytotoxic cells remain to sufficiently kill the remaining cancer. In particular, this significantly reduced cancer population explains why the number of exhausted CD8+ T cells during the optimal treatment is comparable to Treatments 1 and 2, as the extent of antigen exposure is substantially decreased.

Of particular note is the concentration of TNF since it directly induces necroptosis of cancer cells, causing the release of DAMPs, which in turn induces DC maturation. For the first two to three months after treatment commencement, the concentration of TNF is increased compared to without treatment. However, without treatment, the TNF concentration at 24 weeks is 5.32×10^{-11} g/cm³, compared to approximately 5.25×10^{-11} g/cm³ with pembrolizumab therapy. To explain this, we first note that with treatment, the concentration of cancer cells decreases significantly over time, leading to reduced levels of DAMPs, as well as lower concentrations of TGF- β and IL-10. This leads to reduced maturation of DCs, which in turn results in decreased activation of naive T cells in the TDLN, subsequently leading to lower concentrations of effector T cells in both the TDLN and TS. This also leads to reduced activation of NK cells and polarisation of macrophages. As a result, the concentration of activated immune cells decreases over time, resulting in decreased rates of secretion of many cytokines, including TNF, since we assumed that the influx of naive immune cells remains constant over time. This also causes the concentration of immunosuppressive cell types, such as M2 macrophages and CAFs, to decrease with pembrolizumab therapy relative to the concentrations without treatment.

However, the concentration of IL-2, which acts as a growth factor for effector CD8+ and Th1 cells, as well as an activator of naive NK cells, increases with treatment. At 12 weeks, the concentration of IL-2 without treatment is 2.43×10^{-12} g/cm³, compared to 2.49×10^{-12} g/cm³, 2.48×10^{-12} g/cm³, and 2.47×10^{-12} g/cm³ with Treatments 1 and 2, and the optimal treatment respectively. We note, however, that at 24 weeks, the concentration of IL-2 decreases with pembrolizumab therapy as a result of the reduction in effector CD8+ T cells in the TS.

We can also analyse the impact of pembrolizumab therapy on the concentration of PD-1 in the TS and the TDLN. As expected, pembrolizumab therapy massively decreases the concentration of PD-1 in the TS and the TDLN. With the optimal treatment, and with Treatments 1 and 2, at 24 weeks, the concentration of PD-1 in the TS is reduced by 16.63%, 17.77%, and 16.31%, respectively. Thus, we see that treatment efficacy and success are directly correlated with the extent of PD-1 concentration reduction. This makes sense since PD-1 inhibits T cell activation in the TDLN, inhibits the cytotoxicity of NK cells, and interacts with PD-L1 to form the PD-1/PD-L1 complex, which inhibits T cell proliferation.

It is also beneficial for us to compare and analyse the time traces of TCR, efficacy, efficiency, and toxicity of Treatments 1 and 2, and the optimal therapy as shown in [Fig 2](#). For most of the treatment

period, the optimal regimen yields the highest TCR and efficacy; however, it is eventually surpassed by Treatments 1 and 2. This occurs since the optimal regimen leads to the greatest pembrolizumab concentrations for the first several weeks, resulting in enhanced exhausted CD8+ T cell reinvigoration and PD-1 depletion. In particular, since Treatments 1 and 2 are not single-dose, pembrolizumab concentrations are replenished with each dose so that the resultant effects occur at lower potency but for a longer period of time. This also explains why Treatment 1, the treatment with the lowest pembrolizumab dosages, is the most efficient during the first three weeks. However, following the administration of a second dose, the other treatments demonstrate greater efficiency, with the optimal treatment becoming much more efficient as the treatment progresses. Finally, as expected, the toxicity of all treatments is generally a non-increasing function of time, but if the pembrolizumab concentration is sufficiently high enough, small spikes in toxicity may occur following dose administration.

We now shift our focus to Fig 1. We see that TCR increases as the dosing increases and spacing decreases. In particular, the TCRs of Treatment 1 and Treatment 2 are high, and the TCR of treatments does not change significantly near these regions.

Unsurprisingly, the regimens of FDA-approved treatments for metastatic MSI-H/dMMR CRC are quite efficient, with the efficiency of Treatment 1 being approximately $8.97 \times 10^{-2}\%$ /mg and the efficiency of Treatment 2 being approximately $7.75 \times 10^{-2}\%$ /mg. Whilst these treatments are amongst the most efficient practical ones, they pale in comparison to the global maximum efficiency of $2.18 \times 10^{-1}\%$ /mg, achieved by administering a single 262 mg dose of pembrolizumab. There is also a clear transition between efficient and inefficient treatments, marked by the rapid shift in efficiency as one deviates from local optima. In particular, treatment is inefficient if its TCR is low, regardless of the dosing and spacing (corresponding to the top left inefficient region in Fig 1), or if an excessive amount of pembrolizumab is administered, regardless of the TCR (corresponding to the bottom right inefficient region in Fig 1).

In the spirit of completeness, we verify that Treatments 1 and 2 are non-toxic and compare their toxicity to that of the optimal regimen found. As expected, Treatments 1 and 2 are non-toxic, with toxicities of 1.86×10^{-1} and 2.53×10^{-1} , respectively, whilst the optimal regimen has a toxicity of 3.12×10^{-1} . Thus, we see that these treatments are all non-toxic, and the optimal regimen has comparable toxicity to FDA-approved regimens for metastatic MSI-H/dMMR CRC.

Striking a balance between TCR, efficiency, and toxicity is difficult, and the current FDA-approved regimens for metastatic MSI-H/dMMR CRC do this quite well in the case of locally advanced MSI-H/dMMR CRC. The optimal regimen of administering pembrolizumab as a single dose of 640 mg is also more efficient, leads to comparable TCR, and is more cost-effective and convenient than current regimens, whilst again, maintaining practicality and safety. Moreover, lower single doses of pembrolizumab are effective, with a single dose of 400 mg (equivalent to 5 mg/kg) achieving a TCR of 76.80%, and a single dose of 560 mg (equivalent to 7 mg/kg) achieving a TCR of 86.43%. The associated toxicities are 1.94×10^{-1} and 2.72×10^{-1} , respectively, which are lower than or comparable to those of Treatments 1 and 2. Administering a single dose of pembrolizumab before surgery has proven highly effective for achieving long-term tumour eradication in a phase 1b clinical trial involving resectable stage III/IV melanoma [202]. In particular, 30% of patients experienced > 90% tumour eradication, and all of these patients remained disease-free at a median follow-up of 25 months. Medium to high single-dose pembrolizumab demonstrates promising potential for successful and cost-effective treatment, with a phase II clinical trial to evaluate the efficacy and safety of a single-dose of 4 mg/kg of pembrolizumab in patients with stage I-III dMMR CRC currently underway [203].

It should be noted that the model has several limitations, many of which exist for simplicity, but the potential for addressing these issues serves as exciting avenues for future research.

- We ignored spatial effects in the model. However, their resolution can provide information about the distribution and clustering of different immune cell types in the TME and their clinical implications [204, 205].
- We assumed that the death rates were constant throughout the T cell proliferation program; however, linear death rates were shown to markedly improve the quality of fit of Deenick et al.'s model [206] to experimental data [207].
- We considered only the M1/M2 macrophage dichotomies, however, their plasticity motivates the description of their phenotypes as a continuum, giving them the ability to adapt their functions to achieve mixtures of M1 and M2 responses and functions [75].
- In the optimisation of neoadjuvant pembrolizumab therapy, we restricted ourselves to treatments with constant dosing and spacing as is common in the literature; however, varying dosages and dosing frequencies may result in improved regimens.
- We did not consider T cell avidity, the overall strength of a TCR-pMHC interaction, which governs whether a cancer cell will be successfully killed [56]. In particular, high-avidity T cells are necessary for lysing cancer cells and durable tumour eradication, whilst low-avidity T cells are ineffective and may inhibit high-avidity T cells [208, 209].
- We also did not consider the influence of cytokines in the TDLN for T cell activation and proliferation, which are important in influencing effector T cell differentiation [210, 211].
- The definition of toxicity does not account for its potential origins in autoimmunity, which is a crucial component of certain adverse effects [196].

In this work, we have provided a framework for mathematically modelling many immune cell types in the TME, using experimental data to govern parameter estimation. We finally analysed and optimised neoadjuvant pembrolizumab therapy for MSI-H/dMMR CRC for efficacy and efficiency. We conclude that a single medium-to-high dose of pembrolizumab is more efficient and demonstrates comparable efficacy and TCR than current FDA-approved regimens for metastatic MSI-H/dMMR CRC whilst maintaining practicality and safety. In addition, the versatility and power of the methods and equations herein can be easily adapted to attain a more comprehensive understanding of other cancers and improve healthcare as a result.

6 CRediT Authorship Contribution Statement

Georgio Hawi: conceptualisation, data curation, formal analysis, funding acquisition, investigation, methodology, project administration, resources, software, validation, visualisation, writing — original draft, writing — review & editing.

Peter S. Kim: conceptualisation, formal analysis, funding acquisition, investigation, methodology, project administration, resources, supervision, validation, visualisation, writing — original draft, writing — review & editing.

Peter P. Lee: conceptualisation, formal analysis, investigation, methodology, project administration, resources, supervision, validation, visualisation, writing — original draft, writing — review & editing.

7 Declaration of Competing Interests

The authors declare that they have no known competing financial interests or personal relationships that could have appeared to influence the work reported in this paper.

8 Data Availability

All data and procedures are available within the manuscript and its Supporting Information file.

9 Acknowledgements

This work was supported by an Australian Government Research Training Program Scholarship. PSK gratefully acknowledges support from the Australian Research Council Discovery Project (DP230100485).

References

- [1] Klimeck L, Heisser T, Hoffmeister M, Brenner H. Colorectal cancer: A health and economic problem. *Best Practice & Research Clinical Gastroenterology*. 2023 Oct;66:101839. Available from: <http://dx.doi.org/10.1016/j.bpg.2023.101839>.
- [2] Biller LH, Schrag D. Diagnosis and Treatment of Metastatic Colorectal Cancer: A Review. *JAMA*. 2021 Feb;325(7):669. Available from: <http://dx.doi.org/10.1001/jama.2021.0106>.
- [3] Siegel RL, Giaquinto AN, Jemal A. Cancer statistics, 2024. *CA: A Cancer Journal for Clinicians*. 2024 Jan;74(1):12–49. Available from: <http://dx.doi.org/10.3322/caac.21820>.
- [4] Gausman V, Dornblaser D, Anand S, Hayes RB, O’Connell K, Du M, et al. Risk Factors Associated With Early-Onset Colorectal Cancer. *Clinical Gastroenterology and Hepatology*. 2020 Nov;18(12):2752-9.e2. Available from: <http://dx.doi.org/10.1016/j.cgh.2019.10.009>.
- [5] Sifaki-Pistolla D, Poimenaki V, Fotopoulou I, Saloustros E, Mavroudis D, Vamvakas L, et al. Significant Rise of Colorectal Cancer Incidence in Younger Adults and Strong Determinants: 30 Years Longitudinal Differences between under and over 50s. *Cancers*. 2022 Sep;14(19):4799. Available from: <http://dx.doi.org/10.3390/cancers14194799>.
- [6] Siegel RL, Wagle NS, Cercek A, Smith RA, Jemal A. Colorectal cancer statistics, 2023. *CA: A Cancer Journal for Clinicians*. 2023 Mar;73(3):233–254. Available from: <http://dx.doi.org/10.3322/caac.21772>.
- [7] Andrew AS, Parker S, Anderson JC, Rees JR, Robinson C, Riddle B, et al. Risk Factors for Diagnosis of Colorectal Cancer at a Late Stage: a Population-Based Study. *Journal of General Internal Medicine*. 2018 Oct;33(12):2100–2105. Available from: <http://dx.doi.org/10.1007/s11606-018-4648-7>.
- [8] Rawla P, Sunkara T, Barsouk A. Epidemiology of colorectal cancer: incidence, mortality, survival, and risk factors. *Gastroenterology Review*. 2019;14(2):89–103. Available from: <http://dx.doi.org/10.5114/pg.2018.81072>.

- [9] Atreya CE, Yaeger R, Chu E. Systemic Therapy for Metastatic Colorectal Cancer: From Current Standards to Future Molecular Targeted Approaches. American Society of Clinical Oncology Educational Book. 2017 May;(37):246–256. Available from: http://dx.doi.org/10.1200/EDBK_175679.
- [10] Moran RG. Leucovorin enhancement of the effects of the fluoropyrimidines on thymidylate synthase. *Cancer*. 1989;63(S6):1008-12. Available from: [http://dx.doi.org/10.1002/1097-0142\(19890315\)63:6+<1008::AID-CNCR2820631303>3.0.CO;2-Z](http://dx.doi.org/10.1002/1097-0142(19890315)63:6+<1008::AID-CNCR2820631303>3.0.CO;2-Z).
- [11] Mohelnikova-Duchonova B. FOLFOX/FOLFIRI pharmacogenetics: The call for a personalized approach in colorectal cancer therapy. *World Journal of Gastroenterology*. 2014;20(30):10316. Available from: <http://dx.doi.org/10.3748/wjg.v20.i30.10316>.
- [12] Gu J, Li Z, Zhou J, Sun Z, Bai C. Response prediction to oxaliplatin plus 5-fluorouracil chemotherapy in patients with colorectal cancer using a four-protein immunohistochemical model. *Oncology Letters*. 2019 Jun. Available from: <http://dx.doi.org/10.3892/ol.2019.10474>.
- [13] Shulman K, Barnett-Griness O, Friedman V, Greenson JK, Gruber SB, Lejbkowitz F, et al. Outcomes of Chemotherapy for Microsatellite Instable–High Metastatic Colorectal Cancers. *JCO Precision Oncology*. 2018 Nov;(2):1–10. Available from: <http://dx.doi.org/10.1200/P0.17.00253>.
- [14] Mulet-Margalef N, Linares J, Badia-Ramentol J, Jimeno M, Sanz Monte C, Manzano Mozo JL, et al. Challenges and Therapeutic Opportunities in the dMMR/MSI-H Colorectal Cancer Landscape. *Cancers*. 2023 Feb;15(4):1022. Available from: <http://dx.doi.org/10.3390/cancers15041022>.
- [15] Boland CR, Thibodeau SN, Hamilton SR, Sidransky D, Eshleman JR, Burt RW, et al. A National Cancer Institute Workshop on Microsatellite Instability for cancer detection and familial predisposition: development of international criteria for the determination of microsatellite instability in colorectal cancer. *Cancer Res*. 1998 Nov;58(22):5248-57. Available from: <https://pubmed.ncbi.nlm.nih.gov/9823339/>.
- [16] Sinicrope FA, Foster NR, Thibodeau SN, Marsoni S, Monges G, Labianca R, et al. DNA Mismatch Repair Status and Colon Cancer Recurrence and Survival in Clinical Trials of 5-Fluorouracil-Based Adjuvant Therapy. *JNCI Journal of the National Cancer Institute*. 2011 May;103(11):863–875. Available from: <http://dx.doi.org/10.1093/jnci/djr153>.
- [17] Venderbosch S, Nagtegaal ID, Maughan TS, Smith CG, Cheadle JP, Fisher D, et al. Mismatch Repair Status and BRAF Mutation Status in Metastatic Colorectal Cancer Patients: A Pooled Analysis of the CAIRO, CAIRO2, COIN, and FOCUS Studies. *Clinical Cancer Research*. 2014 Oct;20(20):5322–5330. Available from: <http://dx.doi.org/10.1158/1078-0432.CCR-14-0332>.
- [18] Fan WX, Su F, Zhang Y, Zhang XL, Du YY, Gao YJ, et al. Oncological characteristics, treatments and prognostic outcomes in MMR-deficient colorectal cancer. *Biomarker Research*. 2024 Aug;12(1). Available from: <http://dx.doi.org/10.1186/s40364-024-00640-7>.
- [19] André T, Shiu KK, Kim TW, Jensen BV, Jensen LH, Punt C, et al. Pembrolizumab in Microsatellite-Instability–High Advanced Colorectal Cancer. *New England Journal of Medicine*. 2020 Dec;383(23):2207–2218. Available from: <http://dx.doi.org/10.1056/NEJMoa2017699>.

- [20] Llosa NJ, Cruise M, Tam A, Wicks EC, Hechenbleikner EM, Taube JM, et al. The Vigorous Immune Microenvironment of Microsatellite Instable Colon Cancer Is Balanced by Multiple Counter-Inhibitory Checkpoints. *Cancer Discovery*. 2015 Jan;5(1):43–51. Available from: <http://dx.doi.org/10.1158/2159-8290.CD-14-0863>.
- [21] Giannakis M, Mu XJ, Shukla SA, Qian ZR, Cohen O, Nishihara R, et al. Genomic Correlates of Immune-Cell Infiltrates in Colorectal Carcinoma. *Cell Reports*. 2016 Apr;15(4):857–865. Available from: <http://dx.doi.org/10.1016/j.celrep.2016.03.075>.
- [22] Ciardiello D, Vitiello PP, Cardone C, Martini G, Troiani T, Martinelli E, et al. Immunotherapy of colorectal cancer: Challenges for therapeutic efficacy. *Cancer Treatment Reviews*. 2019 Jun;76:22–32. Available from: <http://dx.doi.org/10.1016/j.ctrv.2019.04.003>.
- [23] Topalian SL, Hodi FS, Brahmer JR, Gettinger SN, Smith DC, McDermott DF, et al. Safety, Activity, and Immune Correlates of Anti-PD-1 Antibody in Cancer. *New England Journal of Medicine*. 2012 Jun;366(26):2443–2454. Available from: <http://dx.doi.org/10.1056/NEJMoa1200690>.
- [24] Buchbinder EI, Desai A. CTLA-4 and PD-1 Pathways: Similarities, Differences, and Implications of Their Inhibition. *American Journal of Clinical Oncology*. 2016 Feb;39(1):98–106. Available from: <http://dx.doi.org/10.1097/COC.000000000000239>.
- [25] Sarshekeh AM, Overman MJ, Kopetz S. Nivolumab in the Treatment of Microsatellite Instability High Metastatic Colorectal Cancer. *Future Oncology*. 2018 Feb;14(18):1869–1874. Available from: <http://dx.doi.org/10.2217/fon-2017-0696>.
- [26] Yaghoubi N, Soltani A, Ghazvini K, Hassanian SM, Hashemy SI. PD-1/ PD-L1 blockade as a novel treatment for colorectal cancer. *Biomedicine & Pharmacotherapy*. 2019 Feb;110:312–318. Available from: <http://dx.doi.org/10.1016/j.biopha.2018.11.105>.
- [27] Lin X, Kang K, Chen P, Zeng Z, Li G, Xiong W, et al. Regulatory mechanisms of PD-1/PD-L1 in cancers. *Molecular Cancer*. 2024 May;23(1). Available from: <http://dx.doi.org/10.1186/s12943-024-02023-w>.
- [28] Han Y, Liu D, Li L. PD-1/PD-L1 pathway: current researches in cancer. *American journal of cancer research*. 2020;10(3):727. Available from: <https://pmc.ncbi.nlm.nih.gov/articles/PMC7136921/>.
- [29] Oliveira AF, Bretes L, Furtado I. Review of PD-1/PD-L1 Inhibitors in Metastatic dMMR/MSI-H Colorectal Cancer. *Frontiers in Oncology*. 2019 May;9. Available from: <http://dx.doi.org/10.3389/fonc.2019.00396>.
- [30] Lee J, Ahn E, Kissick HT, Ahmed R. Reinvigorating Exhausted T Cells by Blockade of the PD-1 Pathway. *Forum on Immunopathological Diseases and Therapeutics*. 2015;6(1–2):7–17. Available from: <http://dx.doi.org/10.1615/ForumImmunDisTher.2015014188>.
- [31] Zhang Y, Zhang Z. The history and advances in cancer immunotherapy: understanding the characteristics of tumor-infiltrating immune cells and their therapeutic implications. *Cellular & Molecular Immunology*. 2020 Jul;17(8):807–821. Available from: <http://dx.doi.org/10.1038/s41423-020-0488-6>.

- [32] Casak SJ, Marcus L, Fashoyin-Aje L, Mushti SL, Cheng J, Shen YL, et al. FDA Approval Summary: Pembrolizumab for the First-line Treatment of Patients with MSI-H/dMMR Advanced Unresectable or Metastatic Colorectal Carcinoma. *Clinical Cancer Research*. 2021 Apr;27(17):4680–4684. Available from: <http://dx.doi.org/10.1158/1078-0432.CCR-21-0557>.
- [33] Zhang X, Wu T, Cai X, Dong J, Xia C, Zhou Y, et al. Neoadjuvant Immunotherapy for MSI-H/dMMR Locally Advanced Colorectal Cancer: New Strategies and Unveiled Opportunities. *Frontiers in Immunology*. 2022 Mar;13. Available from: <http://dx.doi.org/10.3389/fimmu.2022.795972>.
- [34] Shiu KK, Jiang Y, Saunders M, Seligmann JF, Iveson T, Wilson RH, et al. NEOPRISM-CRC: Neoadjuvant pembrolizumab stratified to tumour mutation burden for high risk stage 2 or stage 3 deficient-MMR/MSI-high colorectal cancer. *Journal of Clinical Oncology*. 2024 Jun;42(17_suppl):LBA3504–LBA3504. Available from: http://dx.doi.org/10.1200/JCO.2024.42.17_suppl.LBA3504.
- [35] Ludford K, Ho WJ, Thomas JV, Raghav KPS, Murphy MB, Fleming ND, et al. Neoadjuvant Pembrolizumab in Localized Microsatellite Instability High/Deficient Mismatch Repair Solid Tumors. *Journal of Clinical Oncology*. 2023 Apr;41(12):2181–2190. Available from: <http://dx.doi.org/10.1200/JCO.22.01351>.
- [36] Centanni M, Moes DJAR, Trocóniz IF, Ciccolini J, van Hasselt JGC. Clinical Pharmacokinetics and Pharmacodynamics of Immune Checkpoint Inhibitors. *Clinical Pharmacokinetics*. 2019 Feb;58(7):835–857. Available from: <http://dx.doi.org/10.1007/s40262-019-00748-2>.
- [37] Le Louedec F, Leenhardt F, Marin C, Chatelut E, Evrard A, Ciccolini J. Cancer Immunotherapy Dosing: A Pharmacokinetic/Pharmacodynamic Perspective. *Vaccines*. 2020 Oct;8(4):632. Available from: <http://dx.doi.org/10.3390/vaccines8040632>.
- [38] Dubé-Pelletier M, Labbé C, Côté J, Pelletier-St-Pierre AA. Pembrolizumab Every 6 Weeks Versus Every 3 Weeks in Advanced Non-Small Cell Lung Cancer. *The Oncologist*. 2023 Jun;28(11):969–977. Available from: <http://dx.doi.org/10.1093/oncolo/oyad182>.
- [39] Lindauer A, Valiathan C, Mehta K, Sriram V, de Greef R, Elassaiss-Schaap J, et al. Translational Pharmacokinetic/Pharmacodynamic Modeling of Tumor Growth Inhibition Supports Dose-Range Selection of the Anti-PD-1 Antibody Pembrolizumab: Translational Pharmacokinetic/Pharmacodynamic Modeling. *CPT: Pharmacometrics & Systems Pharmacology*. 2016 Nov;6(1):11–20. Available from: <http://dx.doi.org/10.1002/psp4.12130>.
- [40] Shang J, Huang L, Huang J, Ren X, Liu Y, Feng Y. Population pharmacokinetic models of anti-PD-1 mAbs in patients with multiple tumor types: A systematic review. *Frontiers in Immunology*. 2022 Aug;13. Available from: <http://dx.doi.org/10.3389/fimmu.2022.871372>.
- [41] Yan T, Yu L, Shangguan D, Li W, Liu N, Chen Y, et al. Advances in pharmacokinetics and pharmacodynamics of PD-1/PD-L1 inhibitors. *International Immunopharmacology*. 2023 Feb;115:109638. Available from: <http://dx.doi.org/10.1016/j.intimp.2022.109638>.
- [42] Wang Cy, Sheng Cc, Ma Gl, Xu D, Liu Xq, Wang Yy, et al. Population pharmacokinetics of the anti-PD-1 antibody camrelizumab in patients with multiple tumor types and model-informed dosing strategy. *Acta Pharmacologica Sinica*. 2020 Nov;42(8):1368–1375. Available from: <http://dx.doi.org/10.1038/s41401-020-00550-y>.

- [43] Puzkiel A, Bianconi G, Pasquiers B, Balakirouchenane D, Arrondeau J, Boudou-Rouquette P, et al. Extending the dosing intervals of nivolumab: model-based simulations in unselected cancer patients. *British Journal of Cancer*. 2024 Mar;130(11):1866–1874. Available from: <http://dx.doi.org/10.1038/s41416-024-02659-x>.
- [44] Kirshtein A, Akbarinejad S, Hao W, Le T, Su S, Aronow RA, et al. Data Driven Mathematical Model of Colon Cancer Progression. *Journal of Clinical Medicine*. 2020 Dec;9(12):3947. Available from: <http://dx.doi.org/10.3390/jcm9123947>.
- [45] Comprehensive molecular characterization of human colon and rectal cancer. *Nature*. 2012 Jul;487(7407):330–337. Available from: <http://dx.doi.org/10.1038/nature11252>.
- [46] Budithi A, Su S, Kirshtein A, Shahriyari L. Data Driven Mathematical Model of FOLFIRI Treatment for Colon Cancer. *Cancers*. 2021 May;13(11):2632. Available from: <http://dx.doi.org/10.3390/cancers13112632>.
- [47] Bozkurt F, Yousef A, Bilgil H, Baleanu D. A mathematical model with piecewise constant arguments of colorectal cancer with chemo-immunotherapy. *Chaos, Solitons & Fractals*. 2023 Mar;168:113207. Available from: <http://dx.doi.org/10.1016/j.chaos.2023.113207>.
- [48] dePillis L. Mathematical Model of Colorectal Cancer with Monoclonal Antibody Treatments. *British Journal of Medicine and Medical Research*. 2014 Jan;4(16):3101–3131. Available from: <http://dx.doi.org/10.9734/BJMMR/2014/8393>.
- [49] Butner JD, Dogra P, Chung C, Pasqualini R, Arap W, Lowengrub J, et al. Mathematical modeling of cancer immunotherapy for personalized clinical translation. *Nature Computational Science*. 2022 Dec;2(12):785–796. Available from: <http://dx.doi.org/10.1038/s43588-022-00377-z>.
- [50] Lai X, Friedman A. Combination therapy of cancer with cancer vaccine and immune checkpoint inhibitors: A mathematical model. *PLOS ONE*. 2017 May;12(5):e0178479. Available from: <http://dx.doi.org/10.1371/journal.pone.0178479>.
- [51] Lai X, Friedman A. How to schedule VEGF and PD-1 inhibitors in combination cancer therapy? *BMC Systems Biology*. 2019 Mar;13(1). Available from: <http://dx.doi.org/10.1186/s12918-019-0706-y>.
- [52] Siewe N, Friedman A. TGF- β inhibition can overcome cancer primary resistance to PD-1 blockade: A mathematical model. *PLOS ONE*. 2021 Jun;16(6):e0252620. Available from: <http://dx.doi.org/10.1371/journal.pone.0252620>.
- [53] Siewe N, Friedman A. Cancer therapy with immune checkpoint inhibitor and CSF-1 blockade: A mathematical model. *Journal of Theoretical Biology*. 2023 Jan;556:111297. Available from: <http://dx.doi.org/10.1016/j.jtbi.2022.111297>.
- [54] Liao KL, Bai XF, Friedman A. IL-27 in combination with anti-PD-1 can be anti-cancer or pro-cancer. *Journal of Theoretical Biology*. 2024 Feb;579:111704. Available from: <http://dx.doi.org/10.1016/j.jtbi.2023.111704>.
- [55] Kumbhari A, Kim PS, Lee PP. Optimisation of anti-cancer peptide vaccines to preferentially elicit high-avidity T cells. *Journal of Theoretical Biology*. 2020 Feb;486:110067. Available from: <http://dx.doi.org/10.1016/j.jtbi.2019.110067>.

- [56] Kumbhari A, Egelston CA, Lee PP, Kim PS. Mature Dendritic Cells May Promote High-Avidity Tuning of Vaccine T Cell Responses. *Frontiers in Immunology*. 2020 Oct;11. Available from: <http://dx.doi.org/10.3389/fimmu.2020.584680>.
- [57] Plambeck M, Kazeroonian A, Loeffler D, Kretschmer L, Salinno C, Schroeder T, et al. Heritable changes in division speed accompany the diversification of single T cell fate. *Proceedings of the National Academy of Sciences*. 2022 Feb;119(9). Available from: <http://dx.doi.org/10.1073/pnas.2116260119>.
- [58] Del Prete A, Salvi V, Soriani A, Laffranchi M, Sozio F, Bosisio D, et al. Dendritic cell subsets in cancer immunity and tumor antigen sensing. *Cellular & Molecular Immunology*. 2023 Mar;20(5):432–447. Available from: <http://dx.doi.org/10.1038/s41423-023-00990-6>.
- [59] Blank CU, Haining WN, Held W, Hogan PG, Kallies A, Lugli E, et al. Defining ‘T cell exhaustion’. *Nature Reviews Immunology*. 2019 Sep;19(11):665–674. Available from: <http://dx.doi.org/10.1038/s41577-019-0221-9>.
- [60] Zhang Y, Lv N, Li M, Liu M, Wu C. Cancer-associated fibroblasts: tumor defenders in radiation therapy. *Cell Death & Disease*. 2023 Aug;14(8). Available from: <http://dx.doi.org/10.1038/s41419-023-06060-z>.
- [61] Mao X, Xu J, Wang W, Liang C, Hua J, Liu J, et al. Crosstalk between cancer-associated fibroblasts and immune cells in the tumor microenvironment: new findings and future perspectives. *Molecular Cancer*. 2021 Oct;20(1). Available from: <http://dx.doi.org/10.1186/s12943-021-01428-1>.
- [62] Briukhovetska D, Dörr J, Endres S, Libby P, Dinarello CA, Kobold S. Interleukins in cancer: from biology to therapy. *Nature Reviews Cancer*. 2021 Jun;21(8):481–499. Available from: <http://dx.doi.org/10.1038/s41568-021-00363-z>.
- [63] Wu T, Dai Y. Tumor microenvironment and therapeutic response. *Cancer Letters*. 2017 Feb;387:61–68. Available from: <http://dx.doi.org/10.1016/j.canlet.2016.01.043>.
- [64] Shah K, Al-Haidari A, Sun J, Kazi JU. T cell receptor (TCR) signaling in health and disease. *Signal Transduction and Targeted Therapy*. 2021 Dec;6(1). Available from: <http://dx.doi.org/10.1038/s41392-021-00823-w>.
- [65] Sugiyarto G, Lau D, Hill SL, Arcia-Anaya D, Boulanger DSM, Parkes EE, et al. Reactivation of low avidity tumor-specific CD8+ T cells associates with immunotherapeutic efficacy of anti-PD-1. *Journal for ImmunoTherapy of Cancer*. 2023 Aug;11(8):e007114. Available from: <https://doi.org/10.1136/jitc-2023-007114>.
- [66] Maimela NR, Liu S, Zhang Y. Fates of CD8+ T cells in Tumor Microenvironment. *Computational and Structural Biotechnology Journal*. 2019;17:1–13. Available from: <http://dx.doi.org/10.1016/j.csbj.2018.11.004>.
- [67] Hoekstra ME, Vijver SV, Schumacher TN. Modulation of the tumor micro-environment by CD8+ T cell-derived cytokines. *Current Opinion in Immunology*. 2021 Apr;69:65–71. Available from: <http://dx.doi.org/10.1016/j.coi.2021.03.016>.
- [68] Caza T, Landas S. Functional and Phenotypic Plasticity of CD4+ T Cell Subsets. *BioMed Research International*. 2015;2015:1-13. Available from: <https://doi.org/10.1155/2015/521957>.

- [69] Furiati SC, Catarino JS, Silva MV, Silva RF, Estevam RB, Teodoro RB, et al. Th1, Th17, and Treg Responses are Differently Modulated by TNF- α Inhibitors and Methotrexate in Psoriasis Patients. *Scientific Reports*. 2019 May;9(1). Available from: <https://doi.org/10.1038/s41598-019-43899-9>.
- [70] Jarnicki AG, Lysaght J, Todryk S, Mills KHG. Suppression of Antitumor Immunity by IL-10 and TGF- β -Producing T Cells Infiltrating the Growing Tumor: Influence of Tumor Environment on the Induction of CD4+ and CD8+ Regulatory T Cells. *The Journal of Immunology*. 2006 Jul;177(2):896–904. Available from: <http://dx.doi.org/10.4049/jimmunol.177.2.896>.
- [71] Turnis ME, Sawant DV, Szymczak-Workman AL, Andrews LP, Delgoffe GM, Yano H, et al. Interleukin-35 Limits Anti-Tumor Immunity. *Immunity*. 2016 Feb;44(2):316–329. Available from: <http://dx.doi.org/10.1016/j.immuni.2016.01.013>.
- [72] Cui G. TH9, TH17, and TH22 Cell Subsets and Their Main Cytokine Products in the Pathogenesis of Colorectal Cancer. *Frontiers in Oncology*. 2019 Oct;9. Available from: <http://dx.doi.org/10.3389/fonc.2019.01002>.
- [73] Hetta HF, Elkady A, Yahia R, Meshall AK, Saad MM, Mekky MA, et al. T follicular helper and T follicular regulatory cells in colorectal cancer: A complex interplay. *Journal of Immunological Methods*. 2020 May;480:112753. Available from: <http://dx.doi.org/10.1016/j.jim.2020.112753>.
- [74] Kerneur C, Cano CE, Olive D. Major pathways involved in macrophage polarization in cancer. *Frontiers in Immunology*. 2022 Oct;13. Available from: <http://dx.doi.org/10.3389/fimmu.2022.1026954>.
- [75] Mills C. M1 and M2 Macrophages: Oracles of Health and Disease. *Critical Reviews in Immunology*. 2012;32(6):463–88. Available from: <https://doi.org/10.1615/critrevimmunol.v32.i6.10>.
- [76] Viola A, Munari F, Sánchez-Rodríguez R, Scolaro T, Castegna A. The Metabolic Signature of Macrophage Responses. *Frontiers in Immunology*. 2019 Jul;10. Available from: <https://doi.org/10.3389/fimmu.2019.01462>.
- [77] Han X, Ding S, Jiang H, Liu G. Roles of Macrophages in the Development and Treatment of Gut Inflammation. *Frontiers in Cell and Developmental Biology*. 2021 Mar;9. Available from: <https://doi.org/10.3389/fcell.2021.625423>.
- [78] Xue J, Schmidt SV, Sander J, Draffehn A, Krebs W, Quester I, et al. Transcriptome-Based Network Analysis Reveals a Spectrum Model of Human Macrophage Activation. *Immunity*. 2014 Feb;40(2):274–88. Available from: <https://doi.org/10.1016/j.immuni.2014.01.006>.
- [79] Raskov H, Orhan A, Christensen JP, Gögenur I. Cytotoxic CD8+ T cells in cancer and cancer immunotherapy. *British Journal of Cancer*. 2020 Sep;124(2):359–367. Available from: <http://dx.doi.org/10.1038/s41416-020-01048-4>.
- [80] Zhang C, Hu Y, Shi C. Targeting Natural Killer Cells for Tumor Immunotherapy. *Frontiers in Immunology*. 2020 Feb;11. Available from: <http://dx.doi.org/10.3389/fimmu.2020.00060>.

- [81] Knutson KL, Disis ML. Tumor antigen-specific T helper cells in cancer immunity and immunotherapy. *Cancer Immunology, Immunotherapy*. 2005 Jan;54(8):721–728. Available from: <http://dx.doi.org/10.1007/s00262-004-0653-2>.
- [82] Haabeth OAW, Tveita AA, Fauskanger M, Schjesvold F, Lorvik KB, Hofgaard PO, et al. How Do CD4+ T Cells Detect and Eliminate Tumor Cells That Either Lack or Express MHC Class II Molecules? *Frontiers in Immunology*. 2014 Apr;5. Available from: <http://dx.doi.org/10.3389/fimmu.2014.00174>.
- [83] Josephs SF, Ichim TE, Prince SM, Kesari S, Marincola FM, Escobedo AR, et al. Unleashing endogenous TNF-alpha as a cancer immunotherapeutic. *Journal of Translational Medicine*. 2018 Aug;16(1). Available from: <http://dx.doi.org/10.1186/s12967-018-1611-7>.
- [84] Wang X, Lin Y. Tumor necrosis factor and cancer, buddies or foes? *Acta Pharmacologica Sinica*. 2008 Nov;29(11):1275–1288. Available from: <http://dx.doi.org/10.1111/j.1745-7254.2008.00889.x>.
- [85] Jorgovanovic D, Song M, Wang L, Zhang Y. Roles of IFN- γ in tumor progression and regression: a review. *Biomarker Research*. 2020 Sep;8(1). Available from: <http://dx.doi.org/10.1186/s40364-020-00228-x>.
- [86] Castro F, Cardoso AP, Gonçalves RM, Serre K, Oliveira MJ. Interferon-Gamma at the Crossroads of Tumor Immune Surveillance or Evasion. *Frontiers in Immunology*. 2018 May;9. Available from: <http://dx.doi.org/10.3389/fimmu.2018.00847>.
- [87] Thomas DA, Massagué J. TGF- β directly targets cytotoxic T cell functions during tumor evasion of immune surveillance. *Cancer Cell*. 2005 Nov;8(5):369–380. Available from: <http://dx.doi.org/10.1016/j.ccr.2005.10.012>.
- [88] Juneja VR, McGuire KA, Manguso RT, LaFleur MW, Collins N, Haining WN, et al. PD-L1 on tumor cells is sufficient for immune evasion in immunogenic tumors and inhibits CD8 T cell cytotoxicity. *Journal of Experimental Medicine*. 2017 Mar;214(4):895–904. Available from: <http://dx.doi.org/10.1084/jem.20160801>.
- [89] Kang YJ, Jeung IC, Park A, Park YJ, Jung H, Kim TD, et al. An increased level of IL-6 suppresses NK cell activity in peritoneal fluid of patients with endometriosis via regulation of SHP-2 expression. *Human Reproduction*. 2014 Jul;29(10):2176–2189. Available from: <http://dx.doi.org/10.1093/humrep/deu172>.
- [90] Hsu J, Hodgins JJ, Marathe M, Nicolai CJ, Bourgeois-Daigneault MC, Trevino TN, et al. Contribution of NK cells to immunotherapy mediated by PD-1/PD-L1 blockade. *Journal of Clinical Investigation*. 2018 Sep;128(10):4654–4668. Available from: <http://dx.doi.org/10.1172/JCI99317>.
- [91] Fucikova J, Kepp O, Kasikova L, Petroni G, Yamazaki T, Liu P, et al. Detection of immunogenic cell death and its relevance for cancer therapy. *Cell Death & Disease*. 2020 Nov;11(11). Available from: <http://dx.doi.org/10.1038/s41419-020-03221-2>.
- [92] Ren Y, Cao L, Wang L, Zheng S, Zhang Q, Guo X, et al. Autophagic secretion of HMGB1 from cancer-associated fibroblasts promotes metastatic potential of non-small cell lung cancer cells via NF κ B signaling. *Cell Death & Disease*. 2021 Sep;12(10). Available from: <http://dx.doi.org/10.1038/s41419-021-04150-4>.

- [93] Ahmed A, Tait SWG. Targeting immunogenic cell death in cancer. *Molecular Oncology*. 2020 Dec;14(12):2994–3006. Available from: <http://dx.doi.org/10.1002/1878-0261.12851>.
- [94] Morandi B, Mortara L, Chiossone L, Accolla RS, Mingari MC, Moretta L, et al. Dendritic Cell Editing by Activated Natural Killer Cells Results in a More Protective Cancer-Specific Immune Response. *PLoS ONE*. 2012 Jun;7(6):e39170. Available from: <http://dx.doi.org/10.1371/journal.pone.0039170>.
- [95] Vivier E, Tomasello E, Baratin M, Walzer T, Ugolini S. Functions of natural killer cells. *Nature Immunology*. 2008 Apr;9(5):503–510. Available from: <http://dx.doi.org/10.1038/ni1582>.
- [96] Ruhland MK, Roberts EW, Cai E, Mujal AM, Marchuk K, Beppler C, et al. Visualizing Synaptic Transfer of Tumor Antigens among Dendritic Cells. *Cancer Cell*. 2020 Jun;37(6):786–99.e5. Available from: <http://dx.doi.org/10.1016/j.ccell.2020.05.002>.
- [97] Choi G, Kim BS, Park YJ, Shim I, Chung Y. Clonal Expansion of Allergen-specific CD4+ T Cell in the Lung in the Absence of Lymph Nodes. *Immune Network*. 2017;17(3):163. Available from: <http://dx.doi.org/10.4110/in.2017.17.3.163>.
- [98] Brunner-Weinzierl MC, Rudd CE. CTLA-4 and PD-1 Control of T-Cell Motility and Migration: Implications for Tumor Immunotherapy. *Frontiers in Immunology*. 2018 Nov;9. Available from: <http://dx.doi.org/10.3389/fimmu.2018.02737>.
- [99] Mizuno R, Sugiura D, Shimizu K, Maruhashi T, Watada M, Okazaki Im, et al. PD-1 Primarily Targets TCR Signal in the Inhibition of Functional T Cell Activation. *Frontiers in Immunology*. 2019 Mar;10. Available from: <http://dx.doi.org/10.3389/fimmu.2019.00630>.
- [100] Harris NL, Watt V, Ronchese F, Le Gros G. Differential T Cell Function and Fate in Lymph Node and Nonlymphoid Tissues. *The Journal of Experimental Medicine*. 2002 Feb;195(3):317–326. Available from: <http://dx.doi.org/10.1084/jem.20011558>.
- [101] Catron DM, Rusch LK, Hataye J, Itano AA, Jenkins MK. CD4+ T cells that enter the draining lymph nodes after antigen injection participate in the primary response and become central-memory cells. *The Journal of Experimental Medicine*. 2006 Mar;203(4):1045–1054. Available from: <http://dx.doi.org/10.1084/jem.20051954>.
- [102] Riley JL. PD-1 signaling in primary T cells. *Immunological Reviews*. 2009 Apr;229(1):114–125. Available from: <http://dx.doi.org/10.1111/j.1600-065X.2009.00767.x>.
- [103] Rosenberg SA. IL-2: The First Effective Immunotherapy for Human Cancer. *The Journal of Immunology*. 2014 Jun;192(12):5451–5458. Available from: <http://dx.doi.org/10.4049/jimmunol.1490019>.
- [104] Oft M. Immune regulation and cytotoxic T cell activation of IL-10 agonists – Preclinical and clinical experience. *Seminars in Immunology*. 2019 Aug;44:101325. Available from: <http://dx.doi.org/10.1016/j.smim.2019.101325>.
- [105] Qiu H, Hu X, Gao L, Chen L, Chen J, Yuan J, et al. Interleukin 10 enhanced CD8+ T cell activity and reduced CD8+ T cell apoptosis in patients with diffuse large B cell lymphoma. *Experimental Cell Research*. 2017 Nov;360(2):146–152. Available from: <http://dx.doi.org/10.1016/j.yexcr.2017.08.036>.

- [106] Lee KA, Shin KS, Kim GY, Song YC, Bae EA, Kim IK, et al. Characterization of age-associated exhausted CD8⁺ T cells defined by increased expression of Tim-3 and PD-1. *Aging Cell*. 2016 Jan;15(2):291–300. Available from: <http://dx.doi.org/10.1111/ace1.12435>.
- [107] Shive CL, Freeman ML, Younes S, Kowal CM, Canaday DH, Rodriguez B, et al. Markers of T Cell Exhaustion and Senescence and Their Relationship to Plasma TGF- β Levels in Treated HIV⁺ Immune Non-responders. *Frontiers in Immunology*. 2021 Mar;12. Available from: <http://dx.doi.org/10.3389/fimmu.2021.638010>.
- [108] Pauken KE, Wherry EJ. Overcoming T cell exhaustion in infection and cancer. *Trends in Immunology*. 2015 Apr;36(4):265–276. Available from: <http://dx.doi.org/10.1016/j.it.2015.02.008>.
- [109] De Boer RJ, Perelson AS. Towards a general function describing T cell proliferation. *Journal of Theoretical Biology*. 1995 Aug;175(4):567–576. Available from: <http://dx.doi.org/10.1006/jtbi.1995.0165>.
- [110] Choudhry H, Helmi N, Abdulaal WH, Zeyadi M, Zamzami MA, Wu W, et al. Prospects of IL-2 in Cancer Immunotherapy. *BioMed Research International*. 2018;2018:1–7. Available from: <http://dx.doi.org/10.1155/2018/9056173>.
- [111] Marangoni F, Zhakyp A, Corsini M, Geels SN, Carrizosa E, Thelen M, et al. Expansion of tumor-associated Treg cells upon disruption of a CTLA-4-dependent feedback loop. *Cell*. 2021 Jul;184(15):3998–4015.e19. Available from: <http://dx.doi.org/10.1016/j.cell.2021.05.027>.
- [112] Fotsitzoudis C, Koulouridi A, Messaritakis I, Konstantinidis T, Gouvas N, Tsiaoussis J, et al. Cancer-Associated Fibroblasts: The Origin, Biological Characteristics and Role in Cancer—A Glance on Colorectal Cancer. *Cancers*. 2022 Sep;14(18):4394. Available from: <http://dx.doi.org/10.3390/cancers14184394>.
- [113] Kroner A, Greenhalgh AD, Zarruk JG, Passos dos Santos R, Gaestel M, David S. TNF and Increased Intracellular Iron Alter Macrophage Polarization to a Detrimental M1 Phenotype in the Injured Spinal Cord. *Neuron*. 2014 Sep;83(5):1098–1116. Available from: <http://dx.doi.org/10.1016/j.neuron.2014.07.027>.
- [114] Kratochvill F, Neale G, Haverkamp JM, Van de Velde LA, Smith AM, Kawauchi D, et al. TNF Counterbalances the Emergence of M2 Tumor Macrophages. *Cell Reports*. 2015 Sep;12(11):1902–1914. Available from: <http://dx.doi.org/10.1016/j.celrep.2015.08.033>.
- [115] Nathan CF, Murray HW, Wiebe ME, Rubin BY. Identification of interferon-gamma as the lymphokine that activates human macrophage oxidative metabolism and antimicrobial activity. *The Journal of experimental medicine*. 1983 Sep;158(3):670–689. Available from: <http://dx.doi.org/10.1084/jem.158.3.670>.
- [116] Ivashkiv LB. IFN γ : signalling, epigenetics and roles in immunity, metabolism, disease and cancer immunotherapy. *Nature Reviews Immunology*. 2018 Jun;18(9):545–558. Available from: <http://dx.doi.org/10.1038/s41577-018-0029-z>.
- [117] Ambade A, Satishchandran A, Saha B, Gyongyosi B, Lowe P, Kodys K, et al. Hepatocellular carcinoma is accelerated by NASH involving M2 macrophage polarization mediated

- by hif-1 α induced IL-10. *OncoImmunology*. 2016 Sep;5(10):e1221557. Available from: <http://dx.doi.org/10.1080/2162402X.2016.1221557>.
- [118] Chen Y, Song Y, Du W, Gong L, Chang H, Zou Z. Tumor-associated macrophages: an accomplice in solid tumor progression. *Journal of Biomedical Science*. 2019 Oct;26(1). Available from: <http://dx.doi.org/10.1186/s12929-019-0568-z>.
- [119] Wei Y, Liang M, Xiong L, Su N, Gao X, Jiang Z. PD-L1 induces macrophage polarization toward the M2 phenotype via Erk/Akt/mTOR. *Experimental Cell Research*. 2021 May;402(2):112575. Available from: <http://dx.doi.org/10.1016/j.yexcr.2021.112575>.
- [120] Zhang F, Wang H, Wang X, Jiang G, Liu H, Zhang G, et al. TGF- β induces M2-like macrophage polarization via SNAIL-mediated suppression of a pro-inflammatory phenotype. *Oncotarget*. 2016 Jul;7(32):52294–52306. Available from: <http://dx.doi.org/10.18632/oncotarget.10561>.
- [121] Chanmee T, Ontong P, Konno K, Itano N. Tumor-Associated Macrophages as Major Players in the Tumor Microenvironment. *Cancers*. 2014 Aug;6(3):1670–1690. Available from: <http://dx.doi.org/10.3390/cancers6031670>.
- [122] Wu X, Lu W, Xu C, Jiang C, Zhuo Z, Wang R, et al. Macrophages Phenotype Regulated by IL-6 Are Associated with the Prognosis of Platinum-Resistant Serous Ovarian Cancer: Integrated Analysis of Clinical Trial and Omics. *Journal of Immunology Research*. 2023 Apr;2023:1–15. Available from: <http://dx.doi.org/10.1155/2023/6455704>.
- [123] Ye J, Xie C, Wang C, Huang J, Yin Z, Heng BC, et al. Promoting musculoskeletal system soft tissue regeneration by biomaterial-mediated modulation of macrophage polarization. *Bioactive Materials*. 2021 Nov;6(11):4096–4109. Available from: <http://dx.doi.org/10.1016/j.bioactmat.2021.04.017>.
- [124] Konjević GM, Vuletić AM, Mirjačić Martinović KM, Larsen AK, Jurišić VB. The role of cytokines in the regulation of NK cells in the tumor environment. *Cytokine*. 2019 May;117:30–40. Available from: <http://dx.doi.org/10.1016/j.cyto.2019.02.001>.
- [125] Widowati W, K Jasaputra D, B Sumitro S, A Widodo M, Mozef T, Rizal R, et al. Effect of interleukins (IL-2, IL-15, IL-18) on receptors activation and cytotoxic activity of natural killer cells in breast cancer cell. *African Health Sciences*. 2020 Jul;20(2):822–832. Available from: <http://dx.doi.org/10.4314/ahs.v20i2.36>.
- [126] Ferlazzo G, Tsang ML, Moretta L, Melioli G, Steinman RM, Münz C. Human Dendritic Cells Activate Resting Natural Killer (NK) Cells and Are Recognized via the NKp30 Receptor by Activated NK Cells. *The Journal of Experimental Medicine*. 2002 Feb;195(3):343–351. Available from: <http://dx.doi.org/10.1084/jem.20011149>.
- [127] Kish DD, Gorbachev AV, Fairchild RL. CD8⁺ T cells produce IL-2, which is required for CD4⁺CD25⁺ T cell regulation of effector CD8⁺ T cell development for contact hypersensitivity responses. *Journal of Leukocyte Biology*. 2005 Jul;78(3):725–735. Available from: <http://dx.doi.org/10.1189/jlbb.0205069>.
- [128] D'Souza WN, Lefrançois L. Frontline: An in-depth evaluation of the production of IL-2 by antigen-specific CD8 T cells in vivo. *European Journal of Immunology*. 2004 Oct;34(11):2977–2985. Available from: <http://dx.doi.org/10.1002/eji.200425485>.

- [129] Hwang ES, Hong JH, Glimcher LH. IL-2 production in developing Th1 cells is regulated by heterodimerization of RelA and T-bet and requires T-bet serine residue 508. *The Journal of Experimental Medicine*. 2005 Nov;202(9):1289–1300. Available from: <http://dx.doi.org/10.1084/jem.20051044>.
- [130] Bhat P, Leggatt G, Waterhouse N, Frazer IH. Interferon- γ derived from cytotoxic lymphocytes directly enhances their motility and cytotoxicity. *Cell Death & Disease*. 2017 Jun;8(6):e2836–e2836. Available from: <http://dx.doi.org/10.1038/cddis.2017.67>.
- [131] Szabo SJ, Sullivan BM, Stemmann C, Satoskar AR, Sleckman BP, Glimcher LH. Distinct Effects of T-bet in TH1 Lineage Commitment and IFN- γ Production in CD4 and CD8 T Cells. *Science*. 2002 Jan;295(5553):338–342. Available from: <http://dx.doi.org/10.1126/science.1065543>.
- [132] Sojka DK, Fowell DJ. Regulatory T cells inhibit acute IFN- γ synthesis without blocking T-helper cell type 1 (Th1) differentiation via a compartmentalized requirement for IL-10. *Proceedings of the National Academy of Sciences*. 2011 Oct;108(45):18336–18341. Available from: <http://dx.doi.org/10.1073/pnas.1110566108>.
- [133] Cui F, Qu D, Sun R, Zhang M, Nan K. NK cell-produced IFN- γ regulates cell growth and apoptosis of colorectal cancer by regulating IL-15. *Experimental and Therapeutic Medicine*. 2019 Dec. Available from: <http://dx.doi.org/10.3892/etm.2019.8343>.
- [134] Mehta AK, Gracias DT, Croft M. TNF activity and T cells. *Cytokine*. 2018 Jan;101:14–18. Available from: <http://dx.doi.org/10.1016/j.cyto.2016.08.003>.
- [135] Basu A, Ramamoorthi G, Albert G, Gallen C, Beyer A, Snyder C, et al. Differentiation and Regulation of TH Cells: A Balancing Act for Cancer Immunotherapy. *Frontiers in Immunology*. 2021 May;12. Available from: <http://dx.doi.org/10.3389/fimmu.2021.669474>.
- [136] Zhang J, Patel MB, Griffiths R, Mao A, Song Ys, Karlovich NS, et al. Tumor Necrosis Factor- α Produced in the Kidney Contributes to Angiotensin II-dependent Hypertension. *Hypertension*. 2014 Dec;64(6):1275–1281. Available from: <http://dx.doi.org/10.1161/HYPERTENSIONAHA.114.03863>.
- [137] Chen S, Saeed AFUH, Liu Q, Jiang Q, Xu H, Xiao GG, et al. Macrophages in immunoregulation and therapeutics. *Signal Transduction and Targeted Therapy*. 2023 May;8(1). Available from: <http://dx.doi.org/10.1038/s41392-023-01452-1>.
- [138] Fauriat C, Long EO, Ljunggren HG, Bryceson YT. Regulation of human NK-cell cytokine and chemokine production by target cell recognition. *Blood*. 2010 Mar;115(11):2167–2176. Available from: <http://dx.doi.org/10.1182/blood-2009-08-238469>.
- [139] Wang R, Jaw JJ, Stutzman NC, Zou Z, Sun PD. Natural killer cell-produced IFN- γ and TNF- α induce target cell cytolysis through up-regulation of ICAM-1. *Journal of Leukocyte Biology*. 2011 Nov;91(2):299–309. Available from: <http://dx.doi.org/10.1189/jlb.0611308>.
- [140] Massagué J. TGF β in Cancer. *Cell*. 2008 Jul;134(2):215–230. Available from: <http://dx.doi.org/10.1016/j.cell.2008.07.001>.
- [141] Tang Q, Bluestone JA. The Foxp3+ regulatory T cell: a jack of all trades, master of regulation. *Nature Immunology*. 2008 Feb;9(3):239–244. Available from: <http://dx.doi.org/10.1038/ni1572>.

- [142] Wu F, Yang J, Liu J, Wang Y, Mu J, Zeng Q, et al. Signaling pathways in cancer-associated fibroblasts and targeted therapy for cancer. *Signal Transduction and Targeted Therapy*. 2021 Jun;6(1). Available from: <http://dx.doi.org/10.1038/s41392-021-00641-0>.
- [143] Itakura E, Huang RR, Wen DR, Paul E, Wünsch PH, Cochran AJ. IL-10 expression by primary tumor cells correlates with melanoma progression from radial to vertical growth phase and development of metastatic competence. *Modern Pathology*. 2011 Jun;24(6):801–809. Available from: <http://dx.doi.org/10.1038/modpathol.2011.5>.
- [144] Krüger-Krasagakes S, Krasagakis K, Garbe C, Schmitt E, Hüls C, Blankenstein T, et al. Expression of interleukin 10 in human melanoma. *British Journal of Cancer*. 1994 Dec;70(6):1182–1185. Available from: <http://dx.doi.org/10.1038/bjc.1994.469>.
- [145] Chen L, Shi Y, Zhu X, Guo W, Zhang M, Che Y, et al. IL-10 secreted by cancer-associated macrophages regulates proliferation and invasion in gastric cancer cells via c-Met/STAT3 signaling. *Oncology Reports*. 2019 Jun. Available from: <http://dx.doi.org/10.3892/or.2019.7206>.
- [146] Qi L, Yu H, Zhang Y, Zhao D, Lv P, Zhong Y, et al. IL-10 secreted by M2 macrophage promoted tumorigenesis through interaction with JAK2 in glioma. *Oncotarget*. 2016 Sep;7(44):71673–71685. Available from: <http://dx.doi.org/10.18632/oncotarget.12317>.
- [147] Moore KW, de Waal Malefyt R, Coffman RL, O’Garra A. Interleukin-10 and the Interleukin-10 Receptor. *Annual Review of Immunology*. 2001 Apr;19(1):683–765. Available from: <http://dx.doi.org/10.1146/annurev.immunol.19.1.683>.
- [148] Tsuji-Takayama K, Suzuki M, Yamamoto M, Harashima A, Okochi A, Otani T, et al. The Production of IL-10 by Human Regulatory T Cells Is Enhanced by IL-2 through a STAT5-Responsive Intronic Enhancer in the IL-10 Locus. *The Journal of Immunology*. 2008 Sep;181(6):3897–3905. Available from: <http://dx.doi.org/10.4049/jimmunol.181.6.3897>.
- [149] Malek TR, Castro I. Interleukin-2 Receptor Signaling: At the Interface between Tolerance and Immunity. *Immunity*. 2010 Aug;33(2):153–165. Available from: <http://dx.doi.org/10.1016/j.immuni.2010.08.004>.
- [150] Xu YD, Cheng M, Shang PP, Yang YQ. Role of IL-6 in dendritic cell functions. *Journal of Leukocyte Biology*. 2021 Aug;111(3):695–709. Available from: <http://dx.doi.org/10.1002/JLB.3MR0621-616RR>.
- [151] Wu X, Tao P, Zhou Q, Li J, Yu Z, Wang X, et al. IL-6 secreted by cancer-associated fibroblasts promotes epithelial-mesenchymal transition and metastasis of gastric cancer via JAK2/STAT3 signaling pathway. *Oncotarget*. 2017 Feb;8(13):20741–20750. Available from: <http://dx.doi.org/10.18632/oncotarget.15119>.
- [152] Saito H, Kuroda H, Matsunaga T, Osaki T, Ikeguchi M. Increased PD-1 expression on CD4+ and CD8+ T cells is involved in immune evasion in gastric cancer. *Journal of Surgical Oncology*. 2012 Nov;107(5):517–522. Available from: <http://dx.doi.org/10.1002/jso.23281>.
- [153] Wu X, Zhang H, Xing Q, Cui J, Li J, Li Y, et al. PD-1+ CD8+ T cells are exhausted in tumours and functional in draining lymph nodes of colorectal cancer patients. *British Journal of Cancer*. 2014 Aug;111(7):1391–1399. Available from: <http://dx.doi.org/10.1038/bjc.2014.416>.

- [154] Jiang Y, Li Y, Zhu B. T-cell exhaustion in the tumor microenvironment. *Cell Death & Disease*. 2015 Jun;6(6):e1792–e1792. Available from: <http://dx.doi.org/10.1038/cddis.2015.162>.
- [155] Luz-Crawford P, Noël D, Fernandez X, Khoury M, Figueroa F, Carrión F, et al. Mesenchymal Stem Cells Repress Th17 Molecular Program through the PD-1 Pathway. *PLoS ONE*. 2012 Sep;7(9):e45272. Available from: <http://dx.doi.org/10.1371/journal.pone.0045272>.
- [156] Giancchetti E, Fierabracci A. Inhibitory Receptors and Pathways of Lymphocytes: The Role of PD-1 in Treg Development and Their Involvement in Autoimmunity Onset and Cancer Progression. *Frontiers in Immunology*. 2018 Oct;9. Available from: <http://dx.doi.org/10.3389/fimmu.2018.02374>.
- [157] Kono Y, Saito H, Miyauchi W, Shimizu S, Murakami Y, Shishido Y, et al. Increased PD-1-positive macrophages in the tissue of gastric cancer are closely associated with poor prognosis in gastric cancer patients. *BMC Cancer*. 2020 Mar;20(1). Available from: <http://dx.doi.org/10.1186/s12885-020-6629-6>.
- [158] Gordon SR, Maute RL, Dulken BW, Hutter G, George BM, McCracken MN, et al. PD-1 expression by tumour-associated macrophages inhibits phagocytosis and tumour immunity. *Nature*. 2017 May;545(7655):495–499. Available from: <http://dx.doi.org/10.1038/nature22396>.
- [159] Liu Y, Cheng Y, Xu Y, Wang Z, Du X, Li C, et al. Increased expression of programmed cell death protein 1 on NK cells inhibits NK-cell-mediated anti-tumor function and indicates poor prognosis in digestive cancers. *Oncogene*. 2017 Jul;36(44):6143–6153. Available from: <http://dx.doi.org/10.1038/onc.2017.209>.
- [160] Berenbaum M. In vivo determination of the fractional kill of human tumor cells by chemotherapeutic agents. *Cancer chemotherapy reports*. 1972;56(5):563-71.
- [161] Zheng Y, Fang YC, Li J. PD-L1 expression levels on tumor cells affect their immunosuppressive activity. *Oncology Letters*. 2019 Sep. Available from: <http://dx.doi.org/10.3892/ol.2019.10903>.
- [162] Oh SA, Wu DC, Cheung J, Navarro A, Xiong H, Cubas R, et al. PD-L1 expression by dendritic cells is a key regulator of T-cell immunity in cancer. *Nature Cancer*. 2020 Jun;1(7):681–691. Available from: <http://dx.doi.org/10.1038/s43018-020-0075-x>.
- [163] Zheng Y, Han L, Chen Z, Li Y, Zhou B, Hu R, et al. PD-L1+CD8+ T cells enrichment in lung cancer exerted regulatory function and tumor-promoting tolerance. *iScience*. 2022 Feb;25(2):103785. Available from: <http://dx.doi.org/10.1016/j.isci.2022.103785>.
- [164] Kowanetz M, Zou W, Gettinger SN, Koeppen H, Kockx M, Schmid P, et al. Differential regulation of PD-L1 expression by immune and tumor cells in NSCLC and the response to treatment with atezolizumab (anti-PD-L1). *Proceedings of the National Academy of Sciences*. 2018 Oct;115(43). Available from: <http://dx.doi.org/10.1073/pnas.1802166115>.
- [165] Chen L. Co-inhibitory molecules of the B7–CD28 family in the control of T-cell immunity. *Nature Reviews Immunology*. 2004 May;4(5):336–347. Available from: <http://dx.doi.org/10.1038/nri1349>.

- [166] Teramoto K, Igarashi T, Kataoka Y, Ishida M, Hanaoka J, Sumimoto H, et al. Clinical significance of PD-L1-positive cancer-associated fibroblasts in pN0M0 non-small cell lung cancer. *Lung Cancer*. 2019 Nov;137:56–63. Available from: <http://dx.doi.org/10.1016/j.lungcan.2019.09.013>.
- [167] Yoshikawa K, Ishida M, Yanai H, Tsuta K, Sekimoto M, Sugie T. Prognostic significance of PD-L1-positive cancer-associated fibroblasts in patients with triple-negative breast cancer. *BMC Cancer*. 2021 Mar;21(1). Available from: <http://dx.doi.org/10.1186/s12885-021-07970-x>.
- [168] Pei L, Liu Y, Liu L, Gao S, Gao X, Feng Y, et al. Roles of cancer-associated fibroblasts (CAFs) in anti- PD-1/PD-L1 immunotherapy for solid cancers. *Molecular Cancer*. 2023 Feb;22(1). Available from: <http://dx.doi.org/10.1186/s12943-023-01731-z>.
- [169] Zhu Z, Zhang H, Chen B, Liu X, Zhang S, Zong Z, et al. PD-L1-Mediated Immunosuppression in Glioblastoma Is Associated With the Infiltration and M2-Polarization of Tumor-Associated Macrophages. *Frontiers in Immunology*. 2020 Nov;11. Available from: <http://dx.doi.org/10.3389/fimmu.2020.588552>.
- [170] Lin DYw, Tanaka Y, Iwasaki M, Gittis AG, Su HP, Mikami B, et al. The PD-1/PD-L1 complex resembles the antigen-binding Fv domains of antibodies and T cell receptors. *Proceedings of the National Academy of Sciences*. 2008 Feb;105(8):3011–3016. Available from: <http://dx.doi.org/10.1073/pnas.0712278105>.
- [171] Maute RL, Gordon SR, Mayer AT, McCracken MN, Natarajan A, Ring NG, et al. Engineering high-affinity PD-1 variants for optimized immunotherapy and immuno-PET imaging. *Proceedings of the National Academy of Sciences*. 2015 Nov;112(47). Available from: <http://dx.doi.org/10.1073/pnas.1519623112>.
- [172] Snowden TJ, van der Graaf PH, Tindall MJ. Methods of Model Reduction for Large-Scale Biological Systems: A Survey of Current Methods and Trends. *Bulletin of Mathematical Biology*. 2017 Jun;79(7):1449–86. Available from: <https://doi.org/10.1007/s11538-017-0277-2>.
- [173] Newman AM, Steen CB, Liu CL, Gentles AJ, Chaudhuri AA, Scherer F, et al. Determining cell type abundance and expression from bulk tissues with digital cytometry. *Nature Biotechnology*. 2019 May;37(7):773–782. Available from: <http://dx.doi.org/10.1038/s41587-019-0114-2>.
- [174] Le T, Aronow RA, Kirshtein A, Shahriyari L. A review of digital cytometry methods: estimating the relative abundance of cell types in a bulk of cells. *Briefings in Bioinformatics*. 2020 Oct;22(4). Available from: <http://dx.doi.org/10.1093/bib/bbaa219>.
- [175] Gong T, Hartmann N, Kohane IS, Brinkmann V, Staedtler F, Letzkus M, et al. Optimal Deconvolution of Transcriptional Profiling Data Using Quadratic Programming with Application to Complex Clinical Blood Samples. *PLoS ONE*. 2011 Nov;6(11):e27156. Available from: <http://dx.doi.org/10.1371/journal.pone.0027156>.
- [176] Liebner DA, Huang K, Parvin JD. MMAD: microarray microdissection with analysis of differences is a computational tool for deconvoluting cell type-specific contributions from tissue samples. *Bioinformatics*. 2013 Oct;30(5):682–689. Available from: <http://dx.doi.org/10.1093/bioinformatics/btt566>.

- [177] Newman AM, Liu CL, Green MR, Gentles AJ, Feng W, Xu Y, et al. Robust enumeration of cell subsets from tissue expression profiles. *Nature Methods*. 2015 Mar;12(5):453–457. Available from: <http://dx.doi.org/10.1038/nmeth.3337>.
- [178] Goldman MJ, Craft B, Hastie M, Repečka K, McDade F, Kamath A, et al. Visualizing and interpreting cancer genomics data via the Xena platform. *Nature Biotechnology*. 2020 May;38(6):675–678. Available from: <http://dx.doi.org/10.1038/s41587-020-0546-8>.
- [179] Grossman RL, Heath AP, Ferretti V, Varmus HE, Lowy DR, Kibbe WA, et al. Toward a Shared Vision for Cancer Genomic Data. *New England Journal of Medicine*. 2016 Sep;375(12):1109–1112. Available from: <http://dx.doi.org/10.1056/NEJMp1607591>.
- [180] Kautto EA, Bonneville R, Miya J, Yu L, Krook MA, Reeser JW, et al. Performance evaluation for rapid detection of pan-cancer microsatellite instability with MANTIS. *Oncotarget*. 2016 Dec;8(5):7452–7463. Available from: <http://dx.doi.org/10.18632/oncotarget.13918>.
- [181] Wang X, Chen L, Liu W, Zhang Y, Liu D, Zhou C, et al. TIMEDB: tumor immune micro-environment cell composition database with automatic analysis and interactive visualization. *Nucleic Acids Research*. 2022 Nov;51(D1):D1417–D1424. Available from: <http://dx.doi.org/10.1093/nar/gkac1006>.
- [182] Miao YR, Zhang Q, Lei Q, Luo M, Xie GY, Wang H, et al. ImmuCellAI: A Unique Method for Comprehensive T-Cell Subsets Abundance Prediction and its Application in Cancer Immunotherapy. *Advanced Science*. 2020 Feb;7(7). Available from: <http://dx.doi.org/10.1002/adv.201902880>.
- [183] Sutton GJ, Poppe D, Simmons RK, Walsh K, Nawaz U, Lister R, et al. Comprehensive evaluation of deconvolution methods for human brain gene expression. *Nature Communications*. 2022 Mar;13(1). Available from: <http://dx.doi.org/10.1038/s41467-022-28655-4>.
- [184] Mao C, Chen Y, Xing D, Zhang T, Lin Y, Long C, et al. Resting natural killer cells promote the progress of colon cancer liver metastasis by elevating tumor-derived stem cell factor. *eLife*. 2024 Oct;13. Available from: <http://dx.doi.org/10.7554/eLife.97201.3>.
- [185] Sender R, Weiss Y, Navon Y, Milo I, Azulay N, Keren L, et al. The total mass, number, and distribution of immune cells in the human body. *Proceedings of the National Academy of Sciences*. 2023 Oct;120(44). Available from: <http://dx.doi.org/10.1073/pnas.2308511120>.
- [186] Maini R, Nagalli S. *Lymphadenopathy*. StatPearls Publishing, Treasure Island (FL); 2023. Available from: <https://www.ncbi.nlm.nih.gov/books/NBK558918/>.
- [187] West H, Jin J. Lymph Nodes and Lymphadenopathy in Cancer. *JAMA Oncology*. 2016 Jul;2(7):971. Available from: <http://dx.doi.org/10.1001/jamaoncol.2015.3509>.
- [188] Becht E, Giraldo NA, Lacroix L, Buttard B, Elarouci N, Petitprez F, et al. Estimating the population abundance of tissue-infiltrating immune and stromal cell populations using gene expression. *Genome Biology*. 2016 Oct;17(1). Available from: <http://dx.doi.org/10.1186/s13059-016-1070-5>.
- [189] Sturm G, Finotello F, Petitprez F, Zhang JD, Baumbach J, Fridman WH, et al. Comprehensive evaluation of transcriptome-based cell-type quantification methods for immunology. *Bioinformatics*. 2019 Jul;35(14):i436–i445. Available from: <http://dx.doi.org/10.1093/bioinformatics/btz363>.

- [190] Lin A, Zhang J, Luo P. Crosstalk Between the MSI Status and Tumor Microenvironment in Colorectal Cancer. *Frontiers in Immunology*. 2020 Aug;11. Available from: <http://dx.doi.org/10.3389/fimmu.2020.02039>.
- [191] Burke JR, Brown P, Quyn A, Lambie H, Tolan D, Sagar P. Tumour growth rate of carcinoma of the colon and rectum: retrospective cohort study. *BJS Open*. 2020 Sep;4(6):1200–1207. Available from: <http://dx.doi.org/10.1002/bjs5.50355>.
- [192] Clough E, Barrett T. In: *The Gene Expression Omnibus Database*. Springer New York; 2016. p. 93–110. Available from: http://dx.doi.org/10.1007/978-1-4939-3578-9_5.
- [193] Barrett T, Wilhite SE, Ledoux P, Evangelista C, Kim IF, Tomashevsky M, et al. NCBI GEO: archive for functional genomics data sets—update. *Nucleic Acids Research*. 2012 Nov;41(D1):D991–D995. Available from: <http://dx.doi.org/10.1093/nar/gks1193>.
- [194] Leydold SM, Seewald M, Stratowa C, Kaserer K, Sommergruber W, Kraut N, et al. Peroxiredoxin-4 is Over-Expressed in Colon Cancer and its Down-Regulation Leads to Apoptosis. *Cancer Growth and Metastasis*. 2011 Jan;4:CGM.S6584. Available from: <http://dx.doi.org/10.4137/CGM.S6584>.
- [195] Derwinger K, Kodeda K, Bexe-Lindskog E, Tafin H. Tumour differentiation grade is associated with TNM staging and the risk of node metastasis in colorectal cancer. *Acta Oncologica*. 2009 Dec;49(1):57–62. Available from: <http://dx.doi.org/10.3109/02841860903334411>.
- [196] Wang DY, Johnson DB, Davis EJ. Toxicities Associated With PD-1/PD-L1 Blockade. *The Cancer Journal*. 2018 Jan;24(1):36–40. Available from: <http://dx.doi.org/10.1097/PP0.000000000000296>.
- [197] Martins F, Sofiya L, Sykiotis GP, Lamine F, Maillard M, Fraga M, et al. Adverse effects of immune-checkpoint inhibitors: epidemiology, management and surveillance. *Nature Reviews Clinical Oncology*. 2019 May;16(9):563–580. Available from: <http://dx.doi.org/10.1038/s41571-019-0218-0>.
- [198] Robert C, Schachter J, Long GV, Arance A, Grob JJ, Mortier L, et al. Pembrolizumab versus Ipilimumab in Advanced Melanoma. *New England Journal of Medicine*. 2015 Jun;372(26):2521–2532. Available from: <http://dx.doi.org/10.1056/NEJMoa1503093>.
- [199] Chatterjee M, Turner DC, Felip E, Lena H, Cappuzzo F, Horn L, et al. Systematic evaluation of pembrolizumab dosing in patients with advanced non-small-cell lung cancer. *Annals of Oncology*. 2016 Jul;27(7):1291–1298. Available from: <http://dx.doi.org/10.1093/annonc/mdw174>.
- [200] Merck. KEYTRUDA (pembrolizumab) injection Label; 2021. Available from: https://www.accessdata.fda.gov/drugsatfda_docs/label/2021/125514s0961bl.pdf.
- [201] Simeone E, Mallardo D, Giannarelli D, Festino L, Vanella V, Trojaniello C, et al. Correlation of nivolumab 480 mg Q4W with better survival than other nivolumab monotherapy schedule in metastatic melanoma patients. *Journal of Clinical Oncology*. 2020 May;38(15_suppl):e22008–e22008. Available from: http://dx.doi.org/10.1200/JCO.2020.38.15_suppl.e22008.

- [202] Huang AC, Orlowski RJ, Xu X, Mick R, George SM, Yan PK, et al. A single dose of neoadjuvant PD-1 blockade predicts clinical outcomes in resectable melanoma. *Nature Medicine*. 2019 Feb;25(3):454–461. Available from: <http://dx.doi.org/10.1038/s41591-019-0357-y>.
- [203] Justesen TF, Gögenur I, Tarpgaard LS, Pfeiffer P, Qvortrup C. Evaluating the efficacy and safety of neoadjuvant pembrolizumab in patients with stage I–III MMR-deficient colon cancer: a national, multicentre, prospective, single-arm, phase II study protocol. *BMJ Open*. 2023 Jun;13(6):e073372. Available from: <http://dx.doi.org/10.1136/bmjopen-2023-073372>.
- [204] Barua S, Fang P, Sharma A, Fujimoto J, Wistuba I, Rao AUK, et al. Spatial interaction of tumor cells and regulatory T cells correlates with survival in non-small cell lung cancer. *Lung Cancer*. 2018 Mar;117:73–79. Available from: <http://dx.doi.org/10.1016/j.lungcan.2018.01.022>.
- [205] Maley CC, Koelble K, Natrajan R, Aktipis A, Yuan Y. An ecological measure of immune-cancer colocalization as a prognostic factor for breast cancer. *Breast Cancer Research*. 2015 Sep;17(1). Available from: <http://dx.doi.org/10.1186/s13058-015-0638-4>.
- [206] Deenick EK, Gett AV, Hodgkin PD. Stochastic Model of T Cell Proliferation: A Calculus Revealing IL-2 Regulation of Precursor Frequencies, Cell Cycle Time, and Survival. *The Journal of Immunology*. 2003 May;170(10):4963–4972. Available from: <http://dx.doi.org/10.4049/jimmunol.170.10.4963>.
- [207] De Boer RJ, Ganusov VV, Milutinović D, Hodgkin PD, Perelson AS. Estimating Lymphocyte Division and Death Rates from CFSE Data. *Bulletin of Mathematical Biology*. 2006 May;68(5):1011–1031. Available from: <http://dx.doi.org/10.1007/s11538-006-9094-8>.
- [208] Kumbhari A, Rose D, Lee PP, Kim PS. A minimal model of T cell avidity may identify sub-therapeutic vaccine schedules. *Mathematical Biosciences*. 2021 Apr;334:108556. Available from: <https://doi.org/10.1016/j.mbs.2021.108556>.
- [209] Chung B, Stuge TB, Murad JP, Beilhack G, Andersen E, Armstrong BD, et al. Antigen-Specific Inhibition of High-Avidity T Cell Target Lysis by Low-Avidity T Cells via Trogocytosis. *Cell Reports*. 2014 Aug;8(3):871–82. Available from: <https://doi.org/10.1016/j.celrep.2014.06.052>.
- [210] Curtsinger JM, Schmidt CS, Mondino A, Lins DC, Kedl RM, Jenkins MK, et al. Inflammatory Cytokines Provide a Third Signal for Activation of Naive CD4⁺ and CD8⁺ T Cells. *The Journal of Immunology*. 1999 Mar;162(6):3256–3262. Available from: <http://dx.doi.org/10.4049/jimmunol.162.6.3256>.
- [211] Raphael I, Nalawade S, Eagar TN, Forsthuber TG. T cell subsets and their signature cytokines in autoimmune and inflammatory diseases. *Cytokine*. 2015 Jul;74(1):5–17. Available from: <http://dx.doi.org/10.1016/j.cyto.2014.09.011>.

Supporting Information: Optimisation of neoadjuvant pembrolizumab therapy for locally advanced MSI-H/dMMR colorectal cancer using data-driven delay integro-differential equations

Georgio Hawi^{1, *}, Peter S. Kim^{1, †}, and Peter P. Lee^{2, †}

¹School of Mathematics and Statistics, University of Sydney, Sydney, Australia

²Department of Immuno-Oncology, Beckman Research Institute, City of Hope, Duarte, California, USA

*Corresponding author: georgio.hawi@sydney.edu.au

†These authors contributed comparably to this work

A Derivation of (2.36)

The derivation of (2.36) follows similarly to that in [1–3], which we include here for completeness. If no pembrolizumab is present, then P_D simply follows the equation

$$\begin{aligned} P_D &= \rho_{P_D^8} T_8 + \rho_{P_D^{\text{ex}}} T_{\text{ex}} + \rho_{P_D^1} T_1 + \rho_{P_D^r} T_r + \rho_{P_D^{M_2}} M_2 + \rho_{P_D^K} K \\ &= \rho_{P_D^1} \left(\frac{\rho_{P_D^8}}{\rho_{P_D^1}} T_8 + \frac{\rho_{P_D^{\text{ex}}}}{\rho_{P_D^1}} T_{\text{ex}} + T_1 + \frac{\rho_{P_D^r}}{\rho_{P_D^1}} T_r + \frac{\rho_{P_D^{M_2}}}{\rho_{P_D^1}} M_2 + \frac{\rho_{P_D^K}}{\rho_{P_D^1}} K \right), \end{aligned}$$

so that

$$\frac{dP_D}{dt} = \rho_{P_D^1} \left(\frac{\rho_{P_D^8}}{\rho_{P_D^1}} \frac{dT_8}{dt} + \frac{\rho_{P_D^{\text{ex}}}}{\rho_{P_D^1}} \frac{dT_{\text{ex}}}{dt} + \frac{dT_1}{dt} + \frac{\rho_{P_D^r}}{\rho_{P_D^1}} \frac{dT_r}{dt} + \frac{\rho_{P_D^{M_2}}}{\rho_{P_D^1}} \frac{dM_2}{dt} + \frac{\rho_{P_D^K}}{\rho_{P_D^1}} \frac{dK}{dt} \right),$$

where $\rho_{P_D^1}$ is constant. However, when pembrolizumab is injected, PD-1 on these PD-1-expressing cells can bind to it, causing their depletion [4] and, in turn, changing the number of PD-1 molecules expressed on each cell. We assume, however, that the ratio of the number of PD-1 molecules expressed on each cell stays invariant. Thus, we can replace $\rho_{P_D^1}$ above with

$P_D / \left(\frac{\rho_{P_D^8}}{\rho_{P_D^1}} T_8 + \frac{\rho_{P_D^{\text{ex}}}}{\rho_{P_D^1}} T_{\text{ex}} + T_1 + \frac{\rho_{P_D^r}}{\rho_{P_D^1}} T_r + \frac{\rho_{P_D^{M_2}}}{\rho_{P_D^1}} M_2 + \frac{\rho_{P_D^K}}{\rho_{P_D^1}} K \right)$. We assume that the depletion of PD-1 follows principles analogous to the log-kill hypothesis for chemotherapeutic agents [5] so that the rate

of depletion is proportional to the pembrolizumab concentration. Taking depletion into account, and denoting $d_{P_D A_1}$ as the rate at which PD-1 binds to pembrolizumab, we have that

$$\begin{aligned} \frac{dP_D}{dt} &= \frac{P_D \left(\frac{\rho_{P_D^8}}{\rho_{P_D^1}} \frac{dT_8}{dt} + \frac{\rho_{P_D^{\text{ex}}}}{\rho_{P_D^1}} \frac{T_{\text{ex}}}{dt} + \frac{dT_1}{dt} + \frac{\rho_{P_D^r}}{\rho_{P_D^1}} \frac{dT_r}{dt} + \frac{\rho_{P_D^{M_2}}}{\rho_{P_D^1}} \frac{dM_2}{dt} + \frac{\rho_{P_D^K}}{\rho_{P_D^1}} \frac{dK}{dt} \right)}{\frac{\rho_{P_D^8}}{\rho_{P_D^1}} T_8 + \frac{\rho_{P_D^{\text{ex}}}}{\rho_{P_D^1}} T_{\text{ex}} + T_1 + \frac{\rho_{P_D^r}}{\rho_{P_D^1}} T_r + \frac{\rho_{P_D^{M_2}}}{\rho_{P_D^1}} M_2 + \frac{\rho_{P_D^K}}{\rho_{P_D^1}} K} - d_{P_D A_1} P_D A_1 \\ &= P_D \frac{\left(\rho_{P_D^8} \frac{dT_8}{dt} + \rho_{P_D^{\text{ex}}} \frac{dT_{\text{ex}}}{dt} + \rho_{P_D^1} \frac{dT_1}{dt} + \rho_{P_D^r} \frac{dT_r}{dt} + \rho_{P_D^{M_2}} \frac{dM_2}{dt} + \rho_{P_D^K} \frac{dK}{dt} \right)}{\rho_{P_D^8} T_8 + \rho_{P_D^{\text{ex}}} T_{\text{ex}} + \rho_{P_D^1} T_1 + \rho_{P_D^r} T_r + \rho_{P_D^{M_2}} M_2 + \rho_{P_D^K} K} - d_{P_D A_1} P_D A_1, \end{aligned}$$

which is the same as (2.36).

B Digital Cytometry Calculations

B.1 Tumour Site Cell Steady States and Initial Conditions

Seven ImmuCellAI cell types have a direct correspondence to state variables in the model, which we outline in Table B.1.

Table B.1: Mappings between state variables of the model and ImmuCellAI immune cell types.

State Variable	ImmuCellAI Cell Type
T_8	Tc
T_{ex}	Tex
T_r	nTreg
D_0, D	DC
T_1	Th1
M_0, M_1, M_2	Macrophage
K_0, K	NK

Aggregated estimated cell proportions generated by ImmuCellAI for steady states and initial conditions, after normalisation, are shown in Table B.2 and Table B.3.

Table B.2: TS steady-state cell proportions for the model, derived using RNA-sequencing deconvolution via ImmuCellAI. Values for italicised cell types are used in estimating TS cell populations in the model. Values for italicised cell types are used in estimating TS cell populations in the model.

Cell Type	Proportion	Cell Type	Proportion
<i>DC</i>	0.055860	<i>nTreg</i>	0.003787
B_cell	0.107446	iTreg	0.003787
Monocyte	0.128762	<i>Th1</i>	0.001895
<i>Macrophage</i>	0.072902	Th2	0.003705
<i>NK</i>	0.138818	Th17	0.002779
Neutrophil	0.150538	Tfh	0.003787
CD4_T	0.040712	CD8_naive	0.003677
CD8_T	0.060652	<i>Tc</i>	0.004668
NKT	0.137899	<i>Tex</i>	0.003677
Tgd	0.062504	MAIT	0.004631
CD4_naive	0.000937	Tcm	0.002786
Tr1	0.003791	Tem	0.000000

Table B.3: Proportions of TS initial conditions for the model, derived using RNA-sequencing deconvolution via ImmuCellAI. Values for italicised cell types are used in estimating TS cell populations in the model.

Cell Type	Proportion	Cell Type	Proportion
<i>DC</i>	0.070785	<i>nTreg</i>	0.005557
B_cell	0.086875	iTreg	0.003705
Monocyte	0.059671	<i>Th1</i>	0.002732
<i>Macrophage</i>	0.073657	Th2	0.002802
<i>NK</i>	0.144167	Th17	0.002758
Neutrophil	0.080897	Tfh	0.009193
CD4_T	0.072488	CD8_naive	0.005449
CD8_T	0.091245	<i>Tc</i>	0.006358
NKT	0.129328	<i>Tex</i>	0.005475
Tgd	0.130304	MAIT	0.005475
CD4_naive	0.000912	Tcm	0.002758
Tr1	0.007410	Tem	0.000000

Seven keys from the LM22 signature matrix have a direct correspondence to state variables in the model, which we outline in [Table B.4](#).

Table B.4: Mappings between state variables of the model and keys of the LM22 signature matrix.

State Variable	LM22 key
D_0	Dendritic cells resting
D	Dendritic cells activated
M_0	Macrophages M0
M_1	Macrophages M1
M_2	Macrophages M2
K_0	NK cells resting
K	NK cells activated

The aggregated estimated cell proportions generated by CIBERSORTx for steady states and initial conditions, after normalisation, are shown in [Table B.5](#) and [Table B.6](#).

Table B.5: TS steady-state cell proportions for the model, derived using RNA-sequencing deconvolution via CIBERSORTx. Values for italicised cell types are used in estimating TS cell populations in the model.

Cell Type	Proportion	Cell Type	Proportion
B cells naive	0.059688	NK cells activated	0.083872
B cells memory	0.000000	Monocytes	0.018276
Plasma cells	0.005234	<i>Macrophages M0</i>	0.069199
T cells CD8	0.159313	<i>Macrophages M1</i>	0.055534
T cells CD4 naive	0.000000	<i>Macrophages M2</i>	0.214657
T cells CD4 memory resting	0.141747	<i>Dendritic cells resting</i>	0.012246
T cells CD4 memory activated	0.026479	<i>Dendritic cells activated</i>	0.004009
T cells follicular helper	0.004593	Mast cells resting	0.034480
T cells regulatory (Tregs)	0.013419	Mast cells activated	0.059208
T cells gamma delta	0.000000	Eosinophils	0.005205
NK cells resting	0.000000	Neutrophils	0.032841

Table B.6: Proportions for TS initial conditions for the model, derived using RNA-sequencing deconvolution via CIBERSORTx. Values for italicised cell types are used in estimating TS cell populations in the model.

Cell Type	Proportion	Cell Type	Proportion
B cells naive	0.024411	<i>NK cells activated</i>	0.085199
B cells memory	0.011051	Monocytes	0.019237
Plasma cells	0.002355	<i>Macrophages M0</i>	0.051451
T cells CD8	0.219758	<i>Macrophages M1</i>	0.051039
T cells CD4 naive	0.000000	<i>Macrophages M2</i>	0.094792
T cells CD4 memory resting	0.177310	<i>Dendritic cells resting</i>	0.019598
T cells CD4 memory activated	0.062485	<i>Dendritic cells activated</i>	0.009977
T cells follicular helper	0.007731	Mast cells resting	0.030947
T cells regulatory (Tregs)	0.032978	Mast cells activated	0.067909
T cells gamma delta	0.000000	Eosinophils	0.018542
<i>NK cells resting</i>	0.005009	Neutrophils	0.008219

The aggregated estimated cell proportions generated by MCP-counter for steady states and initial conditions, after normalisation, are shown in [Table B.7](#) and [Table B.8](#).

Table B.7: TS steady-state cell proportions for the model, derived using RNA-sequencing deconvolution via MCP-counter. Values for italicised cell types are used in estimating TS cell populations in the model.

Cell Type	Proportion	Cell Type	Proportion
CD3 T cells	0.082135	Monocytic lineage	0.089415
CD8 T cells	0.019104	Myeloid dendritic cells	0.056348
Cytotoxic lymphocytes	0.043297	Neutrophils	0.105035
B lineage	0.115906	Endothelial cells	0.108795
NK cells	0.014033	<i>Fibroblasts</i>	0.365932

Table B.8: Proportions for TS initial conditions for the model, derived using RNA-sequencing deconvolution via MCP-counter. Values for italicised cell types are used in estimating TS cell populations in the model.

Cell Type	Proportion	Cell Type	Proportion
CD3 T cells	0.103738	Monocytic lineage	0.087879
CD8 T cells	0.032749	Myeloid dendritic cells	0.073921
Cytotoxic lymphocytes	0.065962	Neutrophils	0.073720
B lineage	0.133257	Endothelial cells	0.100239
NK cells	0.013392	<i>Fibroblasts</i>	0.315143

B.2 TDLN Cell Steady States and Initial Conditions

Mappings between ImmuCellAI immune cell types and TDLN cell types in the model are shown in [Table B.9](#).

Table B.9: Mappings between TDLN cell types in the model and ImmuCellAI immune cell types.

State Variable	ImmuCellAI Cell Type
T_0^8	CD8_naive
T_A^{8LN}	Tc
T_0^4	CD4_naive
T_A^{1LN}	Th1
T_0^r	nTreg
T_A^{rLN}	nTreg

Aggregated estimated cell proportions generated by ImmuCellAI for steady states and initial conditions, after normalisation, are shown in [Table B.10](#) and [Table B.11](#).

Table B.10: TDLN steady-state cell proportions for the model, derived using RNA-sequencing deconvolution via ImmuCellAI. Values for italicised cell types are used in estimating TS cell populations in the model.

Cell Type	Proportion	Cell Type	Proportion
DC	0.133416	<i>nTreg</i>	0.005695
B_cell	0.137854	iTreg	0.002553
Monocyte	0.057306	<i>Th1</i>	0.006186
Macrophage	0.039766	Th2	0.019699
NK	0.027758	Th17	0.006268
Neutrophil	0.083950	Tfh	0.003535
CD4_T	0.139621	<i>CD8_naive</i>	0.006186
CD8_T	0.061858	<i>Tc</i>	0.001293
NKT	0.152219	Tex	0.004418
Tgd	0.104264	MAIT	0.001724
<i>CD4_naive</i>	0.003582	Tr1	0.000851

Table B.11: Proportions of TDLN initial conditions for the model, derived using RNA-sequencing deconvolution via ImmuCellAI. Values for italicised cell types are used in estimating TS cell populations in the model.

Cell Type	Proportion	Cell Type	Proportion
DC	0.162562	<i>nTreg</i>	0.000915
B_cell	0.109441	iTreg	0.003667
Monocyte	0.040678	<i>Th1</i>	0.008197
Macrophage	0.069026	Th2	0.026928
NK	0.037126	Th17	0.004563
Neutrophil	0.082688	Tfh	0.002295
CD4_T	0.135822	<i>CD8_naive</i>	0.006384
CD8_T	0.063604	<i>Tc</i>	0.000914
NKT	0.128791	Tex	0.003672
Tgd	0.107255	MAIT	0.001820
<i>CD4_naive</i>	0.002739	Tr1	0.000915

C Parameter Estimation

We estimate all parameters, where possible, under the assumption that no pembrolizumab has/will be administered. The exception to this is the parameters directly related to pembrolizumab treatment for which the assumptions are explicitly stated during estimation. We also denote 1 d to be 1 day, 1 h to be 1 hour, 1 m to be 1 minute, and 1 s to be 1 second.

C.1 DAMP Steady States and Initial Conditions

Like cytokines, we note that $1 \text{ cm}^3 = 1 \text{ mL}$ for all DAMP measurements. To estimate DAMP steady states and initial conditions, we looked at the respective experimental tissue concentration data, noting that this is more accurate than the more widely available serum/plasma concentration data. Nonethe-

less, we used serum/plasma concentration data, where relevant, to guide estimates if the corresponding tissue concentration data is limited.

C.1.1 Estimates for H

In [6], a study of blood samples from 144 patients with CRC was conducted, with the serum HMGB1 levels of patients with distant metastasis being $13.32 \pm 6.12 \mu\text{g/L}$, which was significantly higher than those with only lymphatic metastasis at $10.14 \pm 4.38 \mu\text{g/L}$. We assumed that the serum concentrations and tissue concentrations of HMGB1 are similar, so we took the initial condition of H to be $5.76 \times 10^{-9} \text{ g/cm}^3$ and the steady state to be $1.01 \times 10^{-8} \text{ g/cm}^3$.

C.1.2 Estimates for S

In epithelial ovarian cancer (EOC), calreticulin concentrations when no drugs are introduced were approximately $2 \times 10^{-2} \pm 2.5 \times 10^{-2} \mu\text{g/mL}$ [7]. Since surface calreticulin is produced by necrotic cancer cells, which have a larger population at steady state compared to initially, we assume that there is more surface calreticulin at steady state. We assumed that calreticulin concentrations in EOC are similar to those in MSI-H/dMMR CRC, so we assumed an initial condition for S of $2.00 \times 10^{-8} \text{ g/cm}^3$ and a steady state of $4.50 \times 10^{-8} \text{ g/cm}^3$.

C.2 Cytokine Steady States and Initial Conditions

To estimate cytokine steady states and initial conditions, we looked at the respective experimental tissue concentration data, noting that $1 \text{ cm}^3 = 1 \text{ mL}$ for all cytokine measurements.

C.2.1 Estimates for I_2

The tissue concentration of IL-2 in CRC is very low and was found to be below the lower limit of quantification in various experiments [8, 9]. In tumour supernatants of invasive ductal cancer, the median IL-2 concentration was found to be 2.1 pg/mL with the interquartile range being $2.0 \text{ pg/mL} - 4.9 \text{ pg/mL}$ [10]. We assumed similar concentrations of IL-2 in the tissue of CRC patients.

Taking into account the well-documented anti-tumour properties of IL-2 [11, 12] and decreased IL-2 serum concentration in metastatic CRC patients compared to those without distant metastasis [13], we assumed that I_2 has a steady state value of $2.00 \times 10^{-12} \text{ g/cm}^3$.

C.2.2 Estimates for I_γ

It was found in [8] that the median tissue concentration of IFN- γ in CRC patients was 15.2 pg/mL , with the upper quartile concentration being approximately 16.9 pg/mL . It was found in [14] that the serum concentration of IFN- γ in stage IV CRC patients (median $\approx 20.75 \text{ pg/mL}$) is significantly higher than that of stage I-III patients (median $\approx 1 \text{ pg/mL}$). We thus set the steady state of I_γ to $1.69 \times 10^{-11} \text{ g/cm}^3$.

C.2.3 Estimates for I_α

It was found in [14] that in advanced CRC patients, i.e those with stage III or stage IV disease, the mean TNF tissue concentration was $\approx 53 \text{ pg/mL}$, with the concentration one standard deviation below the mean being approximately $\approx 16 \text{ pg/mL}$. Furthermore, the serum TNF concentration in stage IV

CRC patients (median 20.3 pg/mL) is significantly higher than in stage III CRC patients (median 16.0 pg/mL) [15]. We thus set the steady state of I_α to 5.30×10^{-11} g/cm³.

C.2.4 Estimates for I_β

It was found in [16] that in CRC patients, the mean TGF- β tissue concentration was 1311.5 pg/mg, with the concentration one standard error above the mean being 1469.1 pg/mg. Assuming a tissue density of 1.03 g/mL, these correspond to tissue concentrations of 1.35×10^6 pg/mL and 1.51×10^6 pg/mL, respectively. Furthermore, the serum TGF- β concentration in stage IV CRC patients (mean 55 pg/mL) is significantly higher than in stage III CRC patients (mean 45 pg/mL) [17]. We thus set the steady state of I_β to 1.51×10^{-6} g/cm³.

C.2.5 Estimates for I_{10}

It was found in [14] that in advanced CRC patients, i.e those with stage III or stage IV disease, the mean IL-10 tissue concentration was 115 pg/mL, with the concentration one standard deviation below the mean being approximately ≈ 46 pg/mL. Furthermore, the serum IL-10 concentration in stage IV CRC patients (mean 36.02 pg/mL) is significantly higher than in stage III CRC patients (mean 17.07 pg/mL) [18]. We thus set the steady state of I_{10} to 1.15×10^{-10} g/cm³, with an initial condition of 4.60×10^{-11} g/cm³.

C.2.6 Estimates for I_6

It was found in [16] that in advanced CRC patients, i.e. those with stage III or stage IV disease, the mean IL-6 tissue concentration was 3026.2 pg/mg, with the concentration one standard error above the mean being 3532.5 pg/mg. Assuming a tissue density of 1.03 g/mL, these correspond to tissue concentrations of 3.12×10^6 pg/mL and 3.64×10^6 pg/mL, respectively. Furthermore, the tissue IL-6 concentration in early CRC patients (mean 4365.9 pg/mg) is significantly higher than in advanced CRC patients (mean 3026.2 pg/mg) [16]. We thus set the steady state of I_6 to 3.12×10^{-6} g/cm³, with an initial condition of 3.64×10^{-6} g/cm³.

C.3 Immune Checkpoint Protein Steady States and Initial Conditions

C.3.1 PD-1 Steady States and Initial Conditions

To find many of the parameters for P_D , we used the baseline data collected in [19] on 5 advanced cancer patients before their pembrolizumab infusions. The net number of PD-1 molecules on the surface of CD4+ T cells was 2053 molec/cell, and so we set $\rho_{P_D^1} = \rho_{P_D^r} = 2.05 \times 10^3$ molec/cell. The net number of PD-1 molecules on the surface of CD8+ T cells was 2761 molec/cell, and so we set $\rho_{P_D^s} = 2.76 \times 10^3$ molec/cell. However, PD-1 is significantly more expressed on exhausted CD8+ T cells compared to effector CD8+ T cells [20]. We estimated that there is a 5-fold increase in PD-1 expression on exhausted CD8+ T cells, so we set $\rho_{P_D^{\text{ex}}} = 1.38 \times 10^4$ molec/cell. The net number of PD-1 molecules on the surface of non-classical monocytes was 1474 molec/cell [19], and assumed that this is the same as that for M2 macrophages, and so we set $\rho_{P_D^{\text{M2}}} = 1.47 \times 10^3$ molec/cell. Despite the net number of PD-1 molecules on the surface of NK cells being below the lower limit of quantification in [19], NK cells substantially express PD-1 [21] in CRC, and so we set $\rho_{P_D^K} = \rho_{P_D^s}/5 = 5.52 \times 10^2$ molec/cell.

This corresponds to

$$\begin{aligned}
\overline{P_D} &= \rho_{P_D^8} \overline{T_8} + \rho_{P_D^{\text{ex}}} \overline{T_{\text{ex}}} + \rho_{P_D^1} \overline{T_1} + \rho_{P_D^r} \overline{T_r} + \rho_{P_{M_2}} \overline{M_2} + \rho_{P_K} \overline{K} = 7.88 \times 10^9 \text{ molec/cm}^3, \\
P_D(0) &= \rho_{P_D^8} T_8(0) + \rho_{P_D^{\text{ex}}} T_{\text{ex}}(0) + \rho_{P_D^1} T_1(0) + \rho_{P_D^r} T_r(0) + \rho_{P_{M_2}} M_2(0) + \rho_{P_K} K(0) = 8.88 \times 10^9 \text{ molec/cm}^3, \\
\overline{P_D^{\text{8LN}}} &= \rho_{P_D^8} \overline{T_A^8} = 3.31 \times 10^9 \text{ molec/cm}^3, \\
P_D^{\text{8LN}}(0) &= \rho_{P_D^8} T_A^8(0) = 2.34 \times 10^9 \text{ molec/cm}^3, \\
\overline{P_D^{\text{1LN}}} &= \rho_{P_D^1} \overline{T_A^1} = 1.18 \times 10^{10} \text{ molec/cm}^3, \\
P_D^{\text{1LN}}(0) &= \rho_{P_D^1} T_A^1(0) = 1.56 \times 10^{10} \text{ molec/cm}^3, \\
\overline{P_D^{\text{rLN}}} &= \rho_{P_D^r} \overline{T_A^r} = 9.82 \times 10^9 \text{ molec/cm}^3, \\
P_D^{\text{rLN}}(0) &= \rho_{P_D^r} T_A^r(0) = 1.58 \times 10^9 \text{ molec/cm}^3.
\end{aligned}$$

C.3.2 PD-L1 Steady States and Initial Conditions

It was found in [22] that the PD-L1 expression on activated CD3+ PD-L1+ T cells was 9282 molec/cell, whilst the PD-L1 expression on mature DCs was 80,372 molec/cell. However, amongst advanced CRC patients, only 22.4% of CD4+ T cells were PD-L1+, and only 16.1% of CD8+ T cells were PD-L1+ [23]. Moreover, only 22% of colonic DCs were PD-L1+ in [24]. We thus assumed that $\rho_{P_L^1} = \rho_{P_L^r} = 2.08 \times 10^3$ molec/cell, $\rho_{P_L^8} = 1.49 \times 10^3$ molec/cell, and $\rho_{P_L^D} = 1.77 \times 10^4$ molec/cell.

It was estimated in [1] and [25] that the ratio of net PD-L1 molecules on M2 macrophages to that of activated CD4+ and CD8+ T cells is 0.01. We assumed this too, so that $\rho_{P_{M_2}}/0.01 = (\rho_{P_L^1} + \rho_{P_L^8})/2 \implies \rho_{P_{M_2}} = 1.79 \times 10^3$ molec/cell. Furthermore, we assumed that the ratio $\rho_{P_{M_2}} : \rho_{P_L^C} : \rho_{P_L^{CF}}$ reflects the percentage of PD-L1+ M2 macrophages, PD-L1+ tumour cells, and PD-L1+ CAFs, respectively. Amongst advanced CRC patients, only 33.4% of tumour cells were PD-L1+, 56.0% of CD90+ stromal cells were PD-L1+, and 35.6% of CD11b+ myeloid cells were PD-L1+ [23]. We assumed that the percentage of PD-L1+ M2 macrophages is equal to the percentage of PD-L1+ CD11b+ myeloid cells, and that the percentage of PD-L1+ CAFs is equal to the percentage of CD90+ stromal cells. We have that $\rho_{P_{M_2}}/35.6\% = \rho_{P_L^C}/33.4\% = \rho_{P_L^{CF}}/56.0\%$. Thus, we have that $\rho_{P_L^C} = 1.67 \times 10^3$ molec/cell, and $\rho_{P_L^{CF}} = 2.81 \times 10^3$ molec/cell.

This corresponds to

$$\begin{aligned}
\overline{P_L^C} &= \rho_{P_L^C} \overline{C} = 5.53 \times 10^{10} \text{ molec/cm}^3, \\
P_L^C(0) &= \rho_{P_L^C} C(0) = 2.99 \times 10^{10} \text{ molec/cm}^3, \\
\overline{P_L} &= \rho_{P_L^C} \overline{C} + \rho_{P_L^D} \overline{D} + \rho_{P_L^8} \overline{T_8} + \rho_{P_L^1} \overline{T_1} + \rho_{P_L^r} \overline{T_r} + \rho_{P_L^{CF}} \overline{C_F} + \rho_{P_{M_2}} \overline{M_2} = 1.39 \times 10^{11} \text{ molec/cm}^3, \\
P_L(0) &= \rho_{P_L^C} C(0) + \rho_{P_L^D} D(0) + \rho_{P_L^8} T_8(0) + \rho_{P_L^1} T_1(0) + \rho_{P_L^r} T_r(0) + \rho_{P_L^{CF}} C_F(0) + \rho_{P_{M_2}} M_2(0) = 1.04 \times 10^{11} \text{ molec/cm}^3, \\
\overline{P_L^{\text{LN}}} &= \rho_{P_L^D} \overline{D^{\text{LN}}} + \rho_{P_L^8} \overline{T_A^8} + \rho_{P_L^1} \overline{T_A^1} + \rho_{P_L^r} \overline{T_A^r} = 1.30 \times 10^{11} \text{ molec/cm}^3, \\
P_L^{\text{LN}}(0) &= \rho_{P_L^D} D^{\text{LN}}(0) + \rho_{P_L^8} T_A^8(0) + \rho_{P_L^1} T_A^1(0) + \rho_{P_L^r} T_A^r(0) = 2.05 \times 10^{11} \text{ molec/cm}^3.
\end{aligned}$$

C.3.3 PD-1/PD-L1 Steady States and Initial Conditions

Looking at (2.44), (2.45), and (2.46), we have that

$$\begin{aligned}
\overline{Q^{8LN}} &= \frac{\alpha_{P_D^{LN} P_L^{LN}}}{d_{Q^{LN}}} \overline{P_D^{8LN} P_L^{LN}} = 9.20 \times 10^4 \text{ molec/cm}^3, \\
Q^{8LN}(0) &= \frac{\alpha_{P_D^{LN} P_L^{LN}}}{d_{Q^{LN}}} P_D^{8LN}(0) P_L^{LN}(0) = 1.02 \times 10^5 \text{ molec/cm}^3, \\
\overline{Q^{1LN}} &= \frac{\alpha_{P_D^{LN} P_L^{LN}}}{d_{Q^{LN}}} \overline{P_D^{1LN} P_L^{LN}} = 3.27 \times 10^5 \text{ molec/cm}^3, \\
Q^{1LN}(0) &= \frac{\alpha_{P_D^{LN} P_L^{LN}}}{d_{Q^{LN}}} P_D^{1LN}(0) P_L^{LN}(0) = 6.79 \times 10^5 \text{ molec/cm}^3, \\
\overline{Q^{rLN}} &= \frac{\alpha_{P_D^{LN} P_L^{LN}}}{d_{Q^{LN}}} \overline{P_D^{rLN} P_L^{LN}} = 2.73 \times 10^5 \text{ molec/cm}^3, \\
Q^{rLN}(0) &= \frac{\alpha_{P_D^{LN} P_L^{LN}}}{d_{Q^{LN}}} P_D^{rLN}(0) P_L^{LN}(0) = 6.88 \times 10^4 \text{ molec/cm}^3.
\end{aligned}$$

where $\alpha_{P_D^{LN} P_L^{LN}}$ and $d_{Q^{LN}}$ are estimated in [Appendix C.7](#).

C.4 Drug Steady States

C.4.1 Pembrolizumab Steady States

The value of the geometric mean C_{avg} of pembrolizumab in serum at steady state varied minimally regardless of whether pembrolizumab was administered at 200 mg every 3 weeks, or 400 mg every 6 weeks [26]. This was equal to approximately 50.8 $\mu\text{g/mL}$, and we assumed this to be the same in tissue, so we took $\overline{A_1} = 5.08 \times 10^{-5} \text{ g/cm}^3$.

C.5 Half-Saturation Constants

We recall that for some species X , K_X is denoted the half-saturation constant of X in a term of the form

$$\frac{X}{K_X + X}.$$

For simplicity, we assume that if \overline{X} denotes the steady state value of X , then

$$\frac{\overline{X}}{K_X + \overline{X}} = \frac{1}{2} \implies K_X = \overline{X}. \quad (\text{C.1})$$

This implies that

$$\begin{aligned}
K_{T_8C} &= \overline{C} \tau_l = 3.31 \times 10^8 \text{ (cell/cm}^3\text{) day}, \\
K_{KD_0} &= \overline{D_0} = 1.46 \times 10^6 \text{ cell/cm}^3, \\
K_{KD} &= \overline{D} = 4.78 \times 10^5 \text{ cell/cm}^3, \\
K_{DH} &= \overline{H} = 1.01 \times 10^{-8} \text{ g/cm}^3, \\
K_{DS} &= \overline{S} = 4.50 \times 10^{-8} \text{ g/cm}^3, \\
K_{T_8I_2} &= K_{T_1I_2} = K_{KI_2} = K_{I_{10}I_2} = \overline{I_2} = 2.00 \times 10^{-12} \text{ g/cm}^3,
\end{aligned}$$

$$\begin{aligned}
K_{CI_\gamma} &= K_{M_1I_\gamma} = K_{MI_\gamma} = \overline{I_\gamma} = 1.69 \times 10^{-11} \text{ g/cm}^3, \\
K_{CI_\alpha} &= K_{M_1I_\alpha} = K_{MI_\alpha} = \overline{I_\alpha} = 5.30 \times 10^{-11} \text{ g/cm}^3, \\
K_{CFI_\beta} &= K_{MI_\beta} = \overline{I_\beta} = 1.51 \times 10^{-6} \text{ g/cm}^3, \\
K_{M_2I_{10}} &= \overline{I_{10}} = 1.15 \times 10^{-10} \text{ g/cm}^3, \\
K_{MI_6} &= \overline{I_6} = 3.12 \times 10^{-6} \text{ g/cm}^3, \\
K_{M_2P_L} &= \overline{P_L} = 1.39 \times 10^{11} \text{ molec/cm}^3, \\
K_{T_{\text{ex}A_1}} &= \overline{A_1} = 5.08 \times 10^{-5} \text{ cm}^3/\text{g}.
\end{aligned}$$

C.6 Inhibition Constants

We recall that for some species X , K_X is denoted as the inhibition constant of X in a term of the form

$$\frac{1}{1 + X/K_X}.$$

For simplicity, we assume that if \overline{X} denotes the steady state value of X , then

$$\frac{1}{1 + \overline{X}/K_X} = \frac{1}{2} \implies K_X = \overline{X}. \quad (\text{C.2})$$

This implies that

$$\begin{aligned}
K_{I_\gamma T_r} &= \overline{T_r} = 1.45 \times 10^5 \text{ cell/cm}^3, \\
K_{CI_\beta} &= \overline{I_\beta} = 1.51 \times 10^{-6} \text{ g/cm}^3, \\
K_{T_8 I_{10}} &= K_{T_{\text{ex}I_{10}}} = \overline{I_{10}} = 1.15 \times 10^{-10} \text{ g/cm}^3, \\
K_{CI_6} &= \overline{I_6} = 3.12 \times 10^{-6} \text{ g/cm}^3, \\
K_{CP_D} &= \overline{P_D} = 7.88 \times 10^9 \text{ molec/cm}^3, \\
K_{CP_L^C} &= \overline{P_L^C} = 5.53 \times 10^{10} \text{ molec/cm}^3, \\
K_{T_0^8 P_D^{\text{SLN}}} &= \tau_8^{\text{act}} \overline{P_D^{\text{SLN}}} = 6.62 \times 10^9 \text{ (molec/cm}^3\text{) day}, \\
K_{T_A^8 Q^{\text{SLN}}} &= \tau_{T_A^8} \overline{Q^{\text{SLN}}} = 4.48 \times 10^5 \text{ (molec/cm}^3\text{) day}, \\
K_{T_0^4 P_D^{\text{1LN}}} &= \tau_4^{\text{act}} \overline{P_D^{\text{1LN}}} = 1.77 \times 10^{10} \text{ (molec/cm}^3\text{) day}, \\
K_{T_A^1 Q^{\text{1LN}}} &= \tau_{T_A^1} \overline{Q^{\text{1LN}}} = 1.35 \times 10^6 \text{ (molec/cm}^3\text{) day}, \\
K_{T_0^r P_D^{\text{rLN}}} &= \tau_r^{\text{act}} \overline{P_D^{\text{rLN}}} = 1.47 \times 10^{10} \text{ (molec/cm}^3\text{) day}, \\
K_{T_A^r Q^{\text{rLN}}} &= \tau_{T_A^r} \overline{Q^{\text{rLN}}} = 7.84 \times 10^5 \text{ (molec/cm}^3\text{) day}.
\end{aligned}$$

C.7 Degradation Rates

We recall the formula that the degradation rate of some species, X , is given by

$$d_X = \frac{\ln 2}{t_{1/2}^X} \quad (\text{C.3})$$

where $t_{1/2}^X$ is the half-life of X .

C.7.1 Estimate for d_H

The half-life of HMGB1 was found to be approximately 3 hours in the context of prostate cancer [27]. We assume a similar value for MSI-H/dMMR CRC, and so

$$d_H = \frac{\ln 2}{3 \text{ h}} = 5.55 \text{ d}^{-1}.$$

C.7.2 Estimate for d_S

Surface calreticulin has a half-life of approximately 12 hours [28, 29]. Thus, we have that

$$d_S = \frac{\ln 2}{12 \text{ h}} = 1.39 \text{ d}^{-1}.$$

C.7.3 Estimate for d_{D_0}

The time taken for immature DCs to degrade is estimated to be 28 days in mice [30]. We assume that this is similarly the case for humans so that this corresponds to

$$d_{D_0} = \frac{1}{28 \text{ d}} = 3.57 \times 10^{-2} \text{ d}^{-1}.$$

C.7.4 Estimate for d_D

Mature DCs have a half-life of 1.5 – 2.9 days in mice [31]. We assume that this is similarly the case for humans, and take $t_{1/2}^D = 2.2 \text{ d}$ so that

$$d_D = \frac{\ln 2}{2.2 \text{ d}} = 3.15 \times 10^{-1} \text{ d}^{-1}.$$

C.7.5 Estimate for $d_{T_0^8}$

The half-life of naive CD8+ T cells in the lymph node was estimated to be 21.5 days in [32] so that

$$d_{T_0^8} = \frac{\ln 2}{21.5 \text{ d}} = 3.22 \times 10^{-2} \text{ d}^{-1}.$$

C.7.6 Estimate for d_{T_8} and $d_{T_{\text{ex}}}$

It was measured in [33] that the mean degradation rate of circulating CD8+ T cells in HIV seronegative patients was 0.009 d^{-1} . We assume that this is the case for MSI-H/dMMR CRC, and so we set $d_{T_8} = d_{T_{\text{ex}}} = 0.009 \text{ d}^{-1}$.

C.7.7 Estimate for $d_{T_0^4}$

The half-life of naive CD4+ T cells in the lymph node was estimated to be 17.2 days in [32] so that

$$d_{T_0^4} = \frac{\ln 2}{17.2 \text{ d}} = 4.03 \times 10^{-2} \text{ d}^{-1}.$$

C.7.8 Estimate for d_{T_1}

It was measured in [33] that the mean degradation rate of circulating CD4+ T cells in HIV seronegative patients was 0.008 d^{-1} . We assume that this is the case for Th1 cells in MSI-H/dMMR CRC, and so we set $d_{T_1} = 0.008 \text{ d}^{-1}$.

C.7.9 Estimate for d_{T_0}

The degradation rate of naive Tregs in the lymph node was estimated to be $2.2 \times 10^{-3} \text{ d}^{-1}$ in [34], and we assume that the degradation rate in MSI-H CRC is similar so that

$$d_{T_0} = 2.2 \times 10^{-3} \text{ d}^{-1}.$$

C.7.10 Estimate for d_{T_r}

The mean half-life of Tregs in healthy adults was measured to be approximately 11 days in [35]. We assume that this is similarly the case for MSI-H/dMMR CRC, and so that this corresponds to

$$d_{T_r} = \frac{\ln 2}{11 \text{ d}} = 6.30 \times 10^{-2} \text{ d}^{-1}.$$

C.7.11 Estimate for d_{C_F}

The half-life of pancreatic stellate cells, one of the most studied subtypes of CAFs in pancreatic cancer, varies between 2 – 5 days [36]. We assume that the half-life of CAFs in CRC is similar, taking it to be 3.5 days, so that

$$d_{C_F} = \frac{\ln 2}{3.5 \text{ d}} = 1.98 \times 10^{-1} \text{ d}^{-1}.$$

C.7.12 Estimate for d_{M_0}

The lifespan for naive macrophages was found in humans to be approximately 1.37 days on average [37]. This corresponds to

$$d_{M_0} = \frac{1}{1.37 \text{ d}} = 0.73 \text{ d}^{-1}.$$

C.7.13 Estimate for d_{M_1}

The lifespan for M1 macrophages was found in humans to be approximately 1.01 days on average [37]. This corresponds to

$$d_{M_1} = \frac{1}{1.01 \text{ d}} = 0.99 \text{ d}^{-1}.$$

C.7.14 Estimate for d_{M_2}

The lifespan for M2 macrophages was found in humans to be approximately 7.41 days on average [37]. This corresponds to

$$d_{M_2} = \frac{1}{7.41 \text{ d}} = 1.35 \times 10^{-1} \text{ d}^{-1}.$$

C.7.15 Estimate for d_{K_0} and d_K

The half-life of human NK cells varies between 1 – 2 weeks [38–40]. We assume that the half-lives of naive and activated NK cells are both equal to 10 days, so that

$$d_{K_0} = d_K = \frac{\ln 2}{10 \text{ d}} = 6.93 \times 10^{-2} \text{ d}^{-1}.$$

C.7.16 Estimate for d_{I_2}

The half-life of IL-2 varies between 5 – 7 minutes [41]. We take $t_{1/2}^{I_2} = 6.9 \text{ m}$ so that

$$d_{I_2} = \frac{\ln 2}{6.9 \text{ m}} = 1.45 \times 10^2 \text{ d}^{-1}.$$

C.7.17 Estimate for d_{I_γ}

The half-life of IFN- γ varies between 25 – 35 minutes [42]. We take $t_{1/2}^{I_\gamma}$ to be 30 minutes so that

$$d_{I_\gamma} = \frac{\ln 2}{30 \text{ m}} = 3.33 \times 10^1 \text{ d}^{-1}.$$

C.7.18 Estimate for d_{I_α}

The half-life of TNF varies between 15 – 30 minutes [43, 44]. We take $t_{1/2}^{I_\alpha}$ to be 18.2 minutes, so that

$$d_{I_\alpha} = \frac{\ln 2}{18.2 \text{ m}} = 5.48 \times 10^1 \text{ d}^{-1}.$$

C.7.19 Estimate for d_{I_β}

The half-life of active TGF- β is approximately 2 – 3 minutes [45]. We take $t_{1/2}^{I_\beta} = 2.5 \text{ m}$, so that

$$d_{I_\beta} = \frac{\ln 2}{2.5 \text{ m}} = 3.99 \times 10^2 \text{ d}^{-1}.$$

C.7.20 Estimate for $d_{I_{10}}$

The half-life of IL-10 varies between 2.7 – 4.5 hours [46]. We take $t_{1/2}^{I_{10}} = 2.7 \text{ h}$ so that

$$d_{I_{10}} = \frac{\ln 2}{2.7 \text{ h}} = 6.16 \text{ d}^{-1}.$$

C.7.21 Estimate for d_{I_6}

The half-life of IL-6 varies between 103 minutes in meningococcal septic shock [47] and 15 hours during acute inflammation [48]. We assume that in MSI-H/dMMR CRC, $t_{1/2}^{I_6} = 15 \text{ h}$ so that

$$d_{I_6} = \frac{\ln 2}{15 \text{ h}} = 1.11 \text{ d}^{-1}.$$

C.7.22 Estimate for d_{A_1}

The half-life of pembrolizumab varies between 22 – 27 days [49–51]. We take it to be 26 days so that

$$d_{A_1} = \frac{\ln 2}{26 \text{ d}} = 2.67 \times 10^{-2} \text{ d}^{-1}.$$

C.7.23 Estimate for $d_{Q^{LN}}$

The dissociation rate of the PD-1/PD-L1 complex was found to be 1.44 s^{-1} in [22]. Thus, we have that

$$d_{Q^{LN}} = 60 \times 60 \times 24 \times 1.44 \text{ s}^{-1} = 1.24 \times 10^5 \text{ d}^{-1}.$$

C.7.24 Estimate for $\alpha_{P_D^{LN} P_L^{LN}}$

The formation rate of the PD-1/PD-L1 complex was found to be $1.84 \times 10^5 \text{ M}^{-1}\text{s}^{-1}$ in [22]. We need to convert this to units of $(\text{molec}/\text{cm}^3)^{-1}\text{d}^{-1}$. We recall that $1 \text{ M} = 1 \text{ mol/L} = 10^{-3} \text{ mol}/\text{cm}^3 = 6.02 \times 10^{20} \text{ molec}/\text{cm}^3$. Thus, we have that

$$\alpha_{P_D^{LN} P_L^{LN}} = 60 \times 60 \times 24 \times 1.84 \times 10^5 \times (6.02 \times 10^{20})^{-1} = 2.64 \times 10^{-11} (\text{molec}/\text{cm}^3)^{-1}\text{d}^{-1}.$$

C.8 TS DAMP and Cell Parameters

C.8.1 Estimates for H

Considering (2.3) at steady state, we have that

$$\lambda_{HN_c} \overline{N_c} + \lambda_{HC_F} \overline{C_F} - d_H \overline{H} = 0.$$

Since HMGB1 is released more by necrotic cancer cells than CAFs, we assume that

$$\frac{\lambda_{HN_c}}{9} = \frac{\lambda_{HC_F}}{1}.$$

Solving these simultaneously leads to

$$\begin{aligned} \lambda_{HN_c} &= 8.59 \times 10^{-15} \text{ (g/cell) day}^{-1}, \\ \lambda_{HC_F} &= 9.55 \times 10^{-16} \text{ (g/cell) day}^{-1}. \end{aligned}$$

C.8.2 Estimates for S

Considering (2.4) at steady state leads to the equation

$$\lambda_{SN_c} \overline{N_c} - d_S \overline{S} = 0.$$

This leads to

$$\lambda_{SN_c} = 1.70 \times 10^{-14} \text{ (g/cell) day}^{-1}.$$

C.8.3 Estimates for D_0 and D

Adding (2.5) and (2.6) at steady state, leads to

$$\mathcal{A}_{D_0} - \lambda_{D_0K} \overline{D_0K} - d_{D_0} \overline{D_0} - \lambda_{DD^{\text{LN}}} \overline{D} - d_D \overline{D} = 0.$$

We assume that HMGB1 is the most potent inducer of DC maturation, and as such, at steady state, we assume that

$$\frac{\lambda_{DH}}{2 \times 10} = \frac{\lambda_{DS}}{2 \times 1}.$$

In [52], it was also shown that the percentage of immature DCs that were lysed as a result of NK cells is roughly linear in the ratio of NK cells to immature DCs. When a 1:1 ratio of activated NK cells to immature DCs is present, after 24 hours, roughly 35.5% of immature DCs are lysed, whereas if a 5:1 ratio is present, 85.5% of immature DCs are lysed. At steady state, the ratio of NK cells to immature DCs is $\approx 2.39 : 1$, corresponding to an approximate 52.85% being lysed. However, if we consider only immature DC loss due to degradation, after 24 hours, only $1 - e^{-d_{D_0}} \approx 3.54\%$ are lost to it. Thus, we assume at steady state that

$$\frac{\lambda_{D_0K} \overline{D_0K}}{0.5285} = \frac{d_{D_0} \overline{D_0}}{0.0354} \implies \lambda_{D_0K} = 1.11 \times 10^{-7} \text{ (cell/cm}^3\text{)}^{-1} \text{ day}^{-1}.$$

Considering (2.6) at steady state leads to

$$\frac{\lambda_{DH} \overline{D_0}}{2} + \frac{\lambda_{DS} \overline{D_0}}{2} - \lambda_{DD^{\text{LN}}} \overline{D} - d_D \overline{D} = 0.$$

Finally, it was found in [53] that only a limited number of DCs migrate up to the TDLN, with at most 4% of DCs reaching the TDLN in melanoma patients when DCs were injected intradermally. We assume at steady state that this holds, too, for MSI-H/dMMR CRC. Taking into account that only $e^{-d_D \tau_m}$ of mature DCs that leave the TS survive their migration to the TDLN, we have that

$$\frac{\lambda_{DD^{\text{LN}}}}{0.04e^{d_D \tau_m}} = \frac{d_D}{1 - 0.04e^{d_D \tau_m}}$$

Solving these simultaneously leads to

$$\begin{aligned} \mathcal{A}_{D_0} &= 9.89 \times 10^5 \text{ (cell/cm}^3\text{)} \text{ day}^{-1}, \\ \lambda_{DH} &= 1.98 \times 10^{-1} \text{ day}^{-1}, \\ \lambda_{DS} &= 1.98 \times 10^{-2} \text{ day}^{-1}, \\ \lambda_{DD^{\text{LN}}} &= 1.68 \times 10^{-2} \text{ day}^{-1}. \end{aligned}$$

C.8.4 Estimates for C_F

We consider (2.24) at steady state, which leads to

$$\left(\lambda_{C_F} + \frac{\lambda_{C_F I_\beta}}{2} \right) \left(1 - \frac{\overline{C_F}}{C_{F0}} \right) - d_{C_F} = 0.$$

We assume that the carrying capacity of CAFs is 120% of its steady state, so that

$$C_{F0} = 1.2 \overline{C_F} = 3.07 \times 10^7 \text{ cell/cm}^3.$$

The mean doubling time of CAFs in CRC was estimated to be 24 h in [54], so we set

$$\lambda_{C_F} = \frac{\ln 2}{24 \text{ h}} = 6.93 \times 10^{-1} \text{ d}^{-1}.$$

Solving these simultaneously leads to

$$\lambda_{C_F I_\beta} = 9.98 \times 10^{-1} \text{ day}^{-1}.$$

C.8.5 Estimates for $M_0/M_1/M_2$

Adding (2.25), (2.26), and (2.27) at steady state, leads to

$$\mathcal{A}_{M_0} - d_{M_0} \overline{M_0} - d_{M_1} \overline{M_1} - d_{M_2} \overline{M_2} = 0 \implies \mathcal{A}_{M_0} = 9.97 \times 10^5 \text{ (cell/cm}^3\text{) day}^{-1}.$$

Using values from [55], and considering (2.25) at steady state, leads to the equations

$$\begin{aligned} \mathcal{A}_{M_0} - \frac{\lambda_{M_1 I_\alpha} \overline{M_0}}{2} - \frac{\lambda_{M_1 I_\gamma} \overline{M_0}}{2} - \frac{\lambda_{M_2 I_{10}} \overline{M_0}}{2} - \frac{\lambda_{M_2 P_L} \overline{M_0}}{2} - d_{M_0} \overline{M_0} &= 0, \\ \frac{\lambda_{M_1 I_\alpha}}{2 \times 10.77} = \frac{\lambda_{M_1 I_\gamma}}{2 \times 12.54} = \frac{\lambda_{M_2 I_{10}}}{2 \times 6.81}. \end{aligned}$$

We assume that TGF- β repolarises M1 macrophages to the M2 phenotype more potently than IL-6, so that at steady state

$$\frac{\lambda_{M I_\beta}}{2 \times 5} = \frac{\lambda_{M I_6}}{2 \times 1}.$$

We also assume that IFN- γ repolarises M2 macrophages to the M1 phenotype slightly more potently than TNF. Hence, at steady state

$$\frac{\lambda_{M I_\gamma}}{2 \times 6} = \frac{\lambda_{M I_\alpha}}{2 \times 5}.$$

At steady state, we assume that

$$\frac{\lambda_{M_1 I_\alpha}/2 + \lambda_{M_1 I_\gamma}/2}{\overline{M_1}} = \frac{\lambda_{M_2 I_{10}}/2 + \lambda_{M_2 P_L}/2}{\overline{M_2}},$$

and that

$$\frac{\lambda_{M I_\gamma} M_1}{2} + \frac{\lambda_{M I_\alpha} M_1}{2} = \frac{\lambda_{M I_\beta} M_2}{2} + \frac{\lambda_{M I_6} M_2}{2}$$

to ensure equilibrium is maintained. Solving these simultaneously leads to,

$$\begin{aligned} \lambda_{M_1 I_\alpha} &= 0.23 \text{ day}^{-1}, \\ \lambda_{M_1 I_\gamma} &= 2.68 \times 10^{-1} \text{ day}^{-1}, \\ \lambda_{M_2 I_{10}} &= 1.46 \times 10^{-1} \text{ day}^{-1}, \\ \lambda_{M_2 P_L} &= 1.78 \text{ day}^{-1}, \\ \lambda_{M I_\gamma} &= 2.05 \times 10^{-1} \text{ day}^{-1}, \\ \lambda_{M I_\alpha} &= 1.71 \times 10^{-1} \text{ day}^{-1}, \\ \lambda_{M I_\beta} &= 8.12 \times 10^{-2} \text{ day}^{-1}, \\ \lambda_{M I_6} &= 1.62 \times 10^{-2} \text{ day}^{-1}. \end{aligned}$$

C.8.6 Estimates for K_0/K

To estimate NK cell production parameters, we do a similar process to macrophages. Adding (2.28) and (2.29) at steady state, leads to

$$\mathcal{A}_{K_0} - d_{K_0}\overline{K_0} - d_K\overline{K} = 0 \implies \mathcal{A}_{K_0} = 3.67 \times 10^5 \text{ (cell/cm}^3\text{) day}^{-1}.$$

Considering (2.29) at steady state leads to the equations

$$\frac{\lambda_{KI_2}\overline{K_0}}{2} + \frac{\lambda_{KD_0}\overline{K_0}}{2} + \frac{\lambda_{KD}\overline{K_0}}{2} - d_K\overline{K} = 0$$

We assume that mature DCs are more potent activators of NK cells than immature DCs so that at steady state

$$\frac{\lambda_{KD}}{2 \times 5} = \frac{\lambda_{KD_0}}{2 \times 1}.$$

We finally assume that DC-mediated NK-cell activation is twice as potent as cytokine-induced activation at steady state so that

$$\frac{\lambda_{KD_0}/2 + \lambda_{KD}/2}{2} = \frac{\lambda_{KI_2}/2}{1}.$$

Solving these simultaneously leads to

$$\begin{aligned} \lambda_{KI_2} &= 4.62 \times 10^{-1} \text{ day}^{-1}, \\ \lambda_{KD_0} &= 1.54 \times 10^{-1} \text{ day}^{-1}, \\ \lambda_{KD} &= 7.70 \times 10^{-1} \text{ day}^{-1}. \end{aligned}$$

C.9 Cytokine Production Constants

To estimate many of the cytokine production constants, we consider (2.30) - (2.34) at steady state and use the data from [55]. For each immune cell, we assume that each cytokine's corresponding gene expression is proportional to its production rate by that cell. We assume that the results for fibroblastic reticular cells in [56] translate directly to results for CAFs, recalling that CAFs are considered to be all fibroblasts found in the TME [56].

C.9.1 Estimates for I_2

Using values from [55] and considering (2.30) at steady state, or equivalently considering (2.49), leads to the equations

$$\frac{\lambda_{I_2T_8}}{0.114615876287774} = \frac{\lambda_{I_2T_1}}{0.335763693785869}$$

and

$$\lambda_{I_2T_8}\overline{T_8} + \lambda_{I_2T_1}\overline{T_1} - d_{I_2}\overline{I_2} = 0.$$

Solving these simultaneously leads to

$$\begin{aligned} \lambda_{I_2T_8} &= 7.44 \times 10^{-16} \text{ (g/cell)}^{-1}\text{day}^{-1}, \\ \lambda_{I_2T_1} &= 2.18 \times 10^{-15} \text{ (g/cell)}^{-1}\text{day}^{-1}. \end{aligned}$$

Consequently, considering (2.49), we have that

$$I_2(0) = \frac{1}{d_{I_2}} (\lambda_{I_2 T_8} T_8(0) + \lambda_{I_2 T_1} T_1(0)) = 2.81 \times 10^{-12} \text{ g/cm}^3.$$

C.9.2 Estimates for I_γ

Using values from [55] and considering (2.31) at steady state, or equivalently considering (2.50), leads to the equations

$$\frac{\lambda_{I_\gamma T_8}}{2 \times 0.0539973307184416} = \frac{\lambda_{I_\gamma T_1}}{2 \times 0.0188926732394088} = \lambda_{I_\gamma K}$$

and

$$(\lambda_{I_\gamma T_8} \overline{T_8} + \lambda_{I_\gamma T_1} \overline{T_1}) \frac{1}{2} + \lambda_{I_\gamma K} \overline{K} - d_{I_\gamma} \overline{I_\gamma} = 0.$$

Solving these simultaneously leads to

$$\begin{aligned} \lambda_{I_\gamma T_8} &= 1.26 \times 10^{-17} \text{ (g/cell)}^{-1} \text{ day}^{-1}, \\ \lambda_{I_\gamma T_1} &= 4.40 \times 10^{-18} \text{ (g/cell)}^{-1} \text{ day}^{-1}, \\ \lambda_{I_\gamma K} &= 1.16 \times 10^{-16} \text{ (g/cell)}^{-1} \text{ day}^{-1}. \end{aligned}$$

Consequently, considering (2.50), we have that

$$I_\gamma(0) = \frac{1}{d_{I_\gamma}} \left[(\lambda_{I_\gamma T_8} T_8(0) + \lambda_{I_\gamma T_1} T_1(0)) \frac{1}{1 + T_r(0)/K_{I_\gamma T_r}} + \lambda_{I_\gamma K} K(0) \right] = 1.82 \times 10^{-11} \text{ g/cm}^3.$$

C.9.3 Estimates for I_α

Using values from [55] and considering (2.3.20) at steady state, or equivalently considering (2.51), leads to the equations

$$\frac{\lambda_{I_\alpha T_8}}{0.0654443776961264} = \frac{\lambda_{I_\alpha T_1}}{0.108187215112606} = \frac{\lambda_{I_\alpha M_1}}{0.0396575742078822} = \frac{\lambda_{I_\alpha K}}{0.114108294134927}$$

and

$$\lambda_{I_\alpha T_8} \overline{T_8} + \lambda_{I_\alpha T_1} \overline{T_1} + \lambda_{I_\alpha M_1} \overline{M_1} + \lambda_{I_\alpha K} \overline{K} - d_{I_\alpha} \overline{I_\alpha} = 0.$$

Solving these simultaneously leads to

$$\begin{aligned} \lambda_{I_\alpha T_8} &= 3.24 \times 10^{-16} \text{ (g/cell)}^{-1} \text{ day}^{-1}, \\ \lambda_{I_\alpha T_1} &= 5.36 \times 10^{-16} \text{ (g/cell)}^{-1} \text{ day}^{-1}, \\ \lambda_{I_\alpha M_1} &= 1.97 \times 10^{-16} \text{ (g/cell)}^{-1} \text{ day}^{-1}, \\ \lambda_{I_\alpha K} &= 5.66 \times 10^{-16} \text{ (g/cell)}^{-1} \text{ day}^{-1}. \end{aligned}$$

Consequently, considering (2.51), we have that

$$I_\alpha(0) = \frac{1}{d_{I_\alpha}} (\lambda_{I_\alpha T_8} T_8(0) + \lambda_{I_\alpha T_1} T_1(0) + \lambda_{I_\alpha M_1} M_1(0) + \lambda_{I_\alpha K} K(0)) = 5.85 \times 10^{-11} \text{ g/cm}^3.$$

C.9.4 Estimates for I_β

We assume that at steady state, CAFs produce twice as much TGF- β than cancer cells in the TME. This, in conjunction with values from [55], and considering (2.32) at steady state, or equivalently considering (2.52), leads to the equations

$$\frac{\lambda_{I_\beta C_F}}{2} = \frac{\lambda_{I_\beta C}}{1}$$

and

$$\frac{\lambda_{I_\beta C_F}}{0.175283003265127} = \frac{\lambda_{I_\beta T_r}}{0.507677682409403}$$

and

$$\lambda_{I_\beta C} \bar{C} + \lambda_{I_\beta T_r} \bar{T}_r + \lambda_{I_\beta C_F} \bar{C}_F - d_{I_\beta} \bar{I}_\beta = 0.$$

Solving these simultaneously leads to

$$\begin{aligned} \lambda_{I_\beta C} &= 7.08 \times 10^{-12} \text{ (g/cell)}^{-1} \text{ day}^{-1}, \\ \lambda_{I_\beta T_r} &= 4.10 \times 10^{-11} \text{ (g/cell)}^{-1} \text{ day}^{-1}, \\ \lambda_{I_\beta C_F} &= 1.42 \times 10^{-11} \text{ (g/cell)}^{-1} \text{ day}^{-1}. \end{aligned}$$

Consequently, considering (2.52), we have that

$$I_\beta(0) = \frac{1}{d_{I_\beta}} (\lambda_{I_\beta C} C(0) + \lambda_{I_\beta T_r} T_r(0) + \lambda_{I_\beta C_F} C_F(0)) = 1.05 \times 10^{-6} \text{ g/cm}^3.$$

C.9.5 Estimates for I_{10}

Amongst 48 different cell lines tested, it was found in [57] that cancer IL-10 production was maximised in cell lines derived from colon carcinomas. As such, we assume that at steady state, cancer production of IL-10 is equal to half of that by M_2 macrophages. We assume that the enhancement factor of IL-2 for IL-10 production by Tregs is similar in CRC to that of inflammatory bowel disease and use the estimate of $\lambda_{I_{10} I_2} = 3$ that was used in [58]. This, in conjunction with values from [55], and considering (2.33) at steady state leads to the equations

$$\frac{\lambda_{I_{10} C}}{1} = \frac{\lambda_{I_{10} M_2}}{2} \tag{C.4}$$

and

$$\frac{\lambda_{I_{10} M_2}}{1} = \frac{\lambda_{I_{10} T_r} \left(1 + \frac{\lambda_{I_{10} I_2}}{2}\right)}{0.472157630570674}$$

and

$$\lambda_{I_{10} C} \bar{C} + \lambda_{I_{10} M_2} \bar{M}_2 + \lambda_{I_{10} T_r} \left(1 + \frac{\lambda_{I_{10} I_2}}{2}\right) \bar{T}_r - d_{I_{10}} \bar{I}_{10} = 0.$$

Solving these simultaneously leads to

$$\begin{aligned} \lambda_{I_{10} C} &= 1.94 \times 10^{-17} \text{ (g/cell)}^{-1} \text{ day}^{-1}, \\ \lambda_{I_{10} M_2} &= 3.89 \times 10^{-17} \text{ (g/cell)}^{-1} \text{ day}^{-1}, \\ \lambda_{I_{10} T_r} &= 7.34 \times 10^{-18} \text{ (g/cell)}^{-1} \text{ day}^{-1}. \end{aligned}$$

C.9.6 Estimates for I_6

Using values from [55], and considering (2.34) at steady state leads to the equations

$$\frac{\lambda_{I_6D}}{0.0101779065606832} = \frac{\lambda_{I_6CF}}{0.0881605096837823}$$

and

$$\lambda_{I_6D}\bar{D} + \lambda_{I_6CF}\bar{C}_F - d_{I_6}\bar{I}_6.$$

Solving these simultaneously leads to

$$\begin{aligned}\lambda_{I_6D} &= 1.56 \times 10^{-14} \text{ (g/cell)}^{-1} \text{ day}^{-1}, \\ \lambda_{I_6CF} &= 1.35 \times 10^{-13} \text{ (g/cell)}^{-1} \text{ day}^{-1}.\end{aligned}$$

C.10 TDLN Subsystem Constants

C.10.1 Estimate for V_{TS}

The mean tumour volume in CRC patients with a T stage of T4a or an N stage of N2 was found to be 27.56 cm³ and 27.57 cm³, respectively. As such, we set $V_{TS} = 2.76 \times 10^1 \text{ cm}^3$.

C.10.2 Estimate for V_{LN}

The mean diameter of lymph nodes in CRC patients where cancer has metastasised was found to be 5.6 mm in [59]. Assuming a spherical lymph node, this corresponds to $V_{LN} = \frac{4}{3} \times 2.8^3 \times \pi \text{ mm}^3 = 9.20 \times 10^{-2} \text{ cm}^3$.

C.10.3 Estimate for τ_m

In [60], it took 18 hours for DCs, which acquired antigen from a site of subcutaneous injection, to arrive at the lymph node. We assume that this migration time is the same for DCs acquiring cancer antigens from the TS so that $\tau_m = 18 \text{ h} = 0.75 \text{ d}$.

C.10.4 Estimate for τ_a

To estimate τ_a , we note that T cells in the TDLN travel at speeds of 11 – 14 $\mu\text{m}/\text{min}$, in comparison to DCs which migrate at speeds of 3 – 6 $\mu\text{m}/\text{min}$ [61]. We thus have that $\tau_a = \frac{4.5}{12.5}\tau_m \approx 0.27 \text{ d}$.

C.10.5 Estimates for CD8+ T cells

It was found in [62] that activated CD8+ T cells required 39 hours on average to complete their first cell division, and so we set $\Delta_8^0 = 39 \text{ h} = 1.63 \text{ d}$. Furthermore, the average division time for subsequent cell cycles is 8.6 hours [62]; however, it can vary between 5 – 28 hours. Thus, we set $\Delta_8 = 8.6 \text{ h} = 0.36 \text{ d}$. It was shown in [63] that fully activated CD8+ T cells divide a minimum of 7 – 10 times; however, they can divide more if persistent antigen exposure is present. Indeed, in Lymphocytic Choriomeningitis Virus (LCV), CD8+ T cells can divide more than 15 times [64]. We perform a compromise and set $n_{\text{max}}^8 = 10$. We thus have that $\tau_{T_A^8} = 4.87 \text{ d}$. Finally, it is widely accepted that T cell exhaustion can arise only days to weeks from the initial antigen exposure in the case of chronic antigen stimulation [65, 66] so that we take $\tau_l = 10 \text{ d}$.

C.10.6 Estimates for Th1 cells

We first note that Th1 cells are phenotypes of CD4+ T helper cells. It was found in [67] that CD4+ T cell priming takes between 1 – 2 days, and so we set $\tau_4^{\text{act}} = 1.5$ d. Compared to CD8+ T cells, CD4+ T cells appear to divide less, with only approximately nine cell divisions as in LCV [68]. We assume this is similar in MSI-H/dMMR CRC, and so set $n_{\text{max}}^1 = 9$. It takes between 12 and 24 hours for the first CD4+ T cell division to occur, with subsequent divisions occurring at a rate of approximately 10 hours per cell division [69]. We thus set $\Delta_1^0 = 18.5$ h = 0.77 d, and $\Delta_1 = 10$ h = 0.42 d. This leads to $\tau_{T_A^1} = 4.13$ d.

C.10.7 Estimates for Tregs

We assume that the activation of Tregs takes the amount of time as that of CD4+ T helper cells so that $\tau_r^{\text{act}} = 1.5$ d. It was found in [70] that in mice, 6 days after tumour implantation, 45% of Tregs in the TDLN had undergone at least 1 division, and 14% had undergone more than six divisions. We thus set $n_{\text{max}}^r = 6$ and assume that the cell division rates of Tregs and CD4+ T helper cells are the same so that $\Delta_r^0 = 0.77$ d and $\Delta_r = 0.42$ d. We thus have that $\tau_{T_A^r} = 2.87$ d.

C.11 T Cell Parameters and Estimates

C.11.1 Estimates for T_0^8 , T_A^8 , T_8 and T_{ex}

Considering (2.8) at steady state leads to

$$\mathcal{A}_{T_0^8} - \overline{R^8} - d_{T_0^8} \overline{T_0^8} = 0,$$

and in particular,

$$\overline{R^8} = \frac{\lambda_{T_0^8 T_A^8} e^{-d_{T_0^8} \tau_8^{\text{act}}} \overline{D^{\text{LN}} T_0^8}}{2}.$$

Considering (2.11) at steady state leads to

$$\frac{2^{n_{\text{max}}^8} e^{-d_{T_0^8} \tau_{T_A^8}} \overline{R^8}}{2} - \lambda_{T_A^8 T_8} \overline{T_A^8} - d_{T_8} \overline{T_A^8} = 0.$$

We first consider the case where no pembrolizumab is present. Considering (2.12) and (2.13) at steady state leads to

$$\begin{aligned} \lambda_{T_A^8 T_8} e^{-d_{T_8} \tau_a} \overline{T_A^8} + \frac{\lambda_{T_8 I_2} \overline{T_8}}{2} - \frac{\lambda_{T_8 C} \overline{T_8}}{2} - \frac{d_{T_8} \overline{T_8}}{2} &= 0, \\ \frac{\lambda_{T_8 C} \overline{T_8}}{2} - \frac{d_{T_{\text{ex}}} \overline{T_{\text{ex}}}}{2} &= 0. \end{aligned}$$

We assume that at steady state, 95% of positive T_8 growth is due to T_A^8 migration to the TS, and the other 5% is due to IL-2-induced proliferation. Thus, we have that

$$\frac{\lambda_{T_A^8 T_8} e^{-d_{T_8} \tau_a} \overline{T_A^8}}{0.95} = \frac{\lambda_{T_8 I_2} \overline{T_8} / 2}{0.05}.$$

To determine $\lambda_{T_{\text{ex}A_1}}$, we assume that when pembrolizumab is present, at steady state 20% of exhausted CD8+ T cells are reinvigorated. That is, we assume that

$$\frac{\lambda_{T_{\text{ex}A_1}} T_{\text{ex}}/2}{0.2} = \frac{d_{T_{\text{ex}}} T_{\text{ex}}/2}{0.8}.$$

Solving these equations simultaneously leads to

$$\begin{aligned} \mathcal{A}_{T_0^8} &= 3.71 \times 10^5 \text{ (cell/cm}^3\text{) day}^{-1}, \\ \lambda_{T_0^8 T_A^8} &= 2.94 \times 10^{-11} \text{ (cell/cm}^3\text{)}^{-1}, \\ \overline{R^8} &= 9.59 \times 10^2 \text{ (cell/cm}^3\text{) day}^{-1}, \\ \lambda_{T_A^8 T_8} &= 3.41 \times 10^{-1} \text{ day}^{-1}, \\ \lambda_{T_8 I_2} &= 8.04 \times 10^{-4} \text{ day}^{-1}, \\ \lambda_{T_8 C} &= 7.08 \times 10^{-3} \text{ day}^{-1}, \\ \lambda_{T_{\text{ex}A_1}} &= 2.25 \times 10^{-3} \text{ day}^{-1}. \end{aligned}$$

C.11.2 Estimates for T_0^4 , T_A^1 , and T_1

Considering (2.14) at steady state leads to

$$\mathcal{A}_{T_0^4} - \overline{R^1} - d_{T_0^4} \overline{T_0^4} = 0,$$

where

$$\overline{R^1} = \frac{\lambda_{T_0^4 T_A^1} e^{-d_{T_0^4} \tau_{\text{act}}^4} \overline{D^{\text{LN}} T_0^4}}{2}.$$

Considering (2.17) at steady state leads to

$$\frac{2^{n_{\text{max}}^1} e^{-d_{T_0^4} \tau_{T_A^1}} \overline{R^1}}{2} - \lambda_{T_A^1 T_1} \overline{T_A^1} - d_{T_1} \overline{T_A^1} = 0.$$

Finally, considering (2.18) at steady state leads to

$$\lambda_{T_A^1 T_1} e^{-d_{T_1} \tau_a} \overline{T_A^1} + \frac{\lambda_{T_1 I_2} \overline{T_1}}{2} - d_{T_1} \overline{T_1} = 0.$$

We assume, like for CD8+ T cells, that at steady state, 95% of positive T_1 growth is due to T_A^1 migration to the TS, and the other 5% is due to IL-2-induced proliferation. Thus, we have that

$$\frac{\lambda_{T_A^1 T_1} e^{-d_{T_1} \tau_a} \overline{T_A^1}}{0.95} = \frac{\lambda_{T_1 I_2} \overline{T_1}/2}{0.05}.$$

Solving these equations simultaneously leads to

$$\begin{aligned} \mathcal{A}_{T_0^4} &= 2.69 \times 10^5 \text{ (cell/cm}^3\text{) day}^{-1}, \\ \lambda_{T_0^4 T_A^1} &= 5.16 \times 10^{-11} \text{ (cell/cm}^3\text{)}^{-1}, \\ \overline{R^1} &= 9.74 \times 10^2 \text{ (cell/cm}^3\text{) day}^{-1}, \\ \lambda_{T_A^1 T_1} &= 2.88 \times 10^{-2} \text{ day}^{-1}, \end{aligned}$$

$$\lambda_{T_1 I_2} = 8.00 \times 10^{-4} \text{ day}^{-1}.$$

C.11.3 Estimates for T_0^r and T_A^r

Considering (2.19) at steady state leads to

$$\mathcal{A}_{T_0^r} - \overline{R^r} - d_{T_0^r} \overline{T_0^r} = 0,$$

where

$$\overline{R^r} = \frac{\lambda_{T_0^r T_A^r} e^{-d_{T_0^r} \tau_{\text{act}}^r} \overline{D^{\text{LN}} T_0^r}}{2}.$$

Considering (2.22) at steady state leads to

$$\frac{2^{n_{\text{max}}^r} e^{-d_{T_0^r} \tau_{T_A^r}^r} \overline{R^r}}{2} - \lambda_{T_A^r T_r} \overline{T_A^r} - d_{T_r} \overline{T_A^r} = 0.$$

Finally, considering (2.23) at steady state leads to

$$\lambda_{T_A^r T_r} e^{-d_{T_r} \tau_a^r} \overline{T_A^r} - d_{T_r} \overline{T_r} = 0.$$

Solving these equations simultaneously leads to

$$\begin{aligned} \mathcal{A}_{T_0^r} &= 9.95 \times 10^4 \text{ (cell/cm}^3\text{) day}^{-1}, \\ \lambda_{T_0^r T_A^r} &= 3.05 \times 10^{-8} \text{ (cell/cm}^3\text{)}^{-1}, \\ \overline{R^r} &= 9.72 \times 10^4 \text{ (cell/cm}^3\text{) day}^{-1}, \\ \lambda_{T_A^r T_r} &= 5.82 \times 10^{-1} \text{ day}^{-1}. \end{aligned}$$

C.12 Estimates for C and N_c

C.12.1 Estimates for C

Since CD8+ T cells are more effective at lysing cancer cells than Th1 cells, we approximate

$$\frac{\lambda_{CT_8}/4}{8} = \lambda_{CT_1}.$$

We assume that CD8+ T cells and NK cells kill cancer cells with similar potency, so we approximate

$$\lambda_{CK}/4 = \lambda_{CT_8}/4 \implies \lambda_{CK} = \lambda_{CT_8}.$$

We also assume that the rate that TNF induces tumour necroptosis is larger than that for IFN- γ , so we approximate

$$\frac{\lambda_{CI_\alpha}}{2 \times 5} = \frac{\lambda_{CI_\gamma}}{2}.$$

We note that not considering (2.1) at steady state as part of the parameter estimation process results in more accurate trajectories for the time period of interest. However, this may result in reduced accuracy for trajectories extending significantly beyond this timeframe.

C.12.2 Estimates for N_c

Considering (2.2) at steady state leads to the equation

$$\frac{\lambda_{CI_\alpha}\bar{C}}{2} + \frac{\lambda_{CI_\gamma}\bar{C}}{2} - d_{N_c}\bar{N}_c = 0.$$

C.12.3 Fitting λ_C , λ_{CT_8} , λ_{CI_α} , and C_0

We fit λ_C , λ_{CT_8} , λ_{CI_α} , and C_0 by choosing the values such that the steady state value of C and N_c is reached at 155 days, in particular ensuring that C and N_c reach steady state at exactly 155 days. Furthermore, we expect monotonicity in the growth of the total cancer population ($C + N_c$) as the cancer progresses without treatment, and so we aim to minimise

$$\text{Objective} = \max \left(\frac{|C(155) - \bar{C}|}{\bar{C}}, \frac{|N_c(155) - \bar{N}_c|}{\bar{N}_c}, \frac{|C(155) + N_c(155) - (\bar{C} + \bar{N}_c)|}{\bar{C} + \bar{N}_c} \right), \quad (\text{C.5})$$

subject to

$$\max_{t \in [0, 155]} (C(t) + N_c(t)) \leq 1.05(\bar{C} + \bar{N}_c). \quad (\text{C.6})$$

We perform a parameter sweep to minimise (C.5) subject to (C.6), and set the parameter space to be $\lambda_C \in (0 \text{ day}^{-1}, 2 \text{ day}^{-1}]$, $\lambda_{CT_8} \in (0 \text{ day}^{-1}, 1 \times 10^{-6} \text{ day}^{-1}]$, $\lambda_{CI_\alpha} \in (0 \text{ day}^{-1}, 2 \text{ day}^{-1}]$, and $C_0 \in (8 \times 10^7 \text{ cell/cm}^3, 10^{11} \text{ cell/cm}^3]$, ensuring that all model parameters are positive. The optimal values of λ_C , λ_{CT_8} , λ_{CI_α} , and C_0 were found to be

$$\begin{aligned} \lambda_C &= 8.35 \times 10^{-1} \text{ day}^{-1}, \\ \lambda_{CT_8} &= 5.60 \times 10^{-7} (\text{cell/cm}^3)^{-1} \text{ day}^{-1}, \\ \lambda_{CI_\alpha} &= 1.63 \times 10^{-1} \text{ day}^{-1}, \\ C_0 &= 5.47 \times 10^8 \text{ cell/cm}^3, \end{aligned}$$

which implies that

$$\begin{aligned} \lambda_{CT_1} &= 1.75 \times 10^{-8} (\text{cell/cm}^3)^{-1} \text{ day}^{-1}, \\ \lambda_{CK} &= 5.60 \times 10^{-7} (\text{cell/cm}^3)^{-1} \text{ day}^{-1}, \\ \lambda_{CI_\gamma} &= 3.30 \times 10^{-2} \text{ day}^{-1}, \\ d_{N_c} &= 0.89 \text{ day}^{-1}. \end{aligned}$$

C.13 Estimates for A_1 and A_1^{LN}

C.13.1 Estimate for f_{pembro}

To determine f_{pembro} , we use the formula

$$f_{\text{pembro}} = \frac{C_{\text{max,ss}}(\xi_{\text{pembro}}) - C_{\text{min,ss}}(\xi_{\text{pembro}})}{\xi_{\text{pembro}}}, \quad (\text{C.7})$$

where $C_{\text{max,ss}}/C_{\text{min,ss}}$ corresponds to the maximum and minimum serum concentration of pembrolizumab at steady state after a dose, ξ_{pembro} , of pembrolizumab is administered, respectively.

For pembrolizumab, the mean $C_{\min,ss}/C_{\max,ss}$ was found to be approximately 32.6/85.8 $\mu\text{g/mL}$ and 22.4/147.7 $\mu\text{g/mL}$ for Treatment 1 and Treatment 2 respectively [26]. This results in $f_{\text{pembro}} \approx 2.90 \times 10^{-7} \text{ g/cm}^3 \text{ day}^{-1}/\text{mg}$ of pembrolizumab administered for all doses.

C.13.2 Estimate for $d_{P_D A_1}$, $d_{P_D^{8LN} A_1^{LN}}$, $d_{P_D^{1LN} A_1^{LN}}$, $d_{P_D^{rLN} A_1^{LN}}$

For simplicity, we assume that the depletion rates of PD-1 by pembrolizumab are the same regardless of the type of PD-1-expressing cell. Thus, we assume $d_{P_D A_1} = d_{P_D^{8LN} A_1^{LN}} = d_{P_D^{1LN} A_1^{LN}} = d_{P_D^{rLN} A_1^{LN}}$. We choose the depletion rates to ensure that the model outputs trajectories that are consistent with our expectations from clinical trials. In particular, we expect the two FDA-approved pembrolizumab regimens for metastatic MSI-H/dMMR CRC to yield comparable efficacies. As such, we set

$$d_{P_D A_1} = d_{P_D^{8LN} A_1^{LN}} = d_{P_D^{1LN} A_1^{LN}} = d_{P_D^{rLN} A_1^{LN}} = 3.62 \times 10^{-1} \text{ (g/cm}^3\text{)}^{-1} \text{ day}^{-1},$$

noting that nearby choices of depletion rates do not significantly alter the model trajectories.

C.13.3 Estimate for $d_{A_1 P_D}$

Three weeks after a 200 mg pembrolizumab dose was administered, the mean net number of PD-1 molecules on each CD8+ T cell was determined to be 2271 molec/cell, corresponding to a 17.75% reduction from treatment commencement in [19]. Similarly, the mean net number of PD-1 molecules on each CD4+ T cell was determined to be 1600 molec/cell, corresponding to a 22.07% reduction. As such, we assume, at steady state, that 20% of pembrolizumab in the TS is used in blocking PD-1, while the remaining 80% degrades naturally. Considering (2.47), we have that

$$\frac{d_{A_1 P_D} \overline{A_1 P_D}}{20\%} = \frac{d_{A_1} \overline{A_1}}{80\%} \implies d_{A_1 P_D} = \frac{d_{A_1}}{4 P_D} = 8.47 \times 10^{-13} \text{ (molec/cm}^3\text{)}^{-1} \text{ day}^{-1}.$$

C.13.4 Estimate for $d_{A_1^{LN} P_D^{8LN}}$, $d_{A_1^{LN} P_D^{1LN}}$, and $d_{A_1^{LN} P_D^{rLN}}$

We use assumptions similar to those used to estimate $d_{A_1 P_D}$, assuming that 20% of pembrolizumab in the TDLN is used in blocking PD-1, while the remaining 80% degrades naturally. Considering (2.48), we have that

$$\frac{\sum_{i=8,1,r} d_{A_1^{LN} P_D^{iLN}} \overline{A_1^{LN} P_D^{iLN}}}{20\%} = \frac{d_{A_1} \overline{A_1^{LN}}}{80\%} \implies \sum_{i=8,1,r} d_{A_1^{LN} P_D^{iLN}} \overline{P_D^{iLN}} = \frac{d_{A_1}}{4}.$$

We assume that the depletion constants for PD-1 molecules in the TDLN are inversely proportional to their corresponding steady-state concentrations. Specifically, for $i = 8, 1, r$,

$$d_{A_1^{LN} P_D^{iLN}} = \frac{\gamma}{P_D^{iLN}},$$

for some constant γ . Solving these simultaneously leads to

$$\gamma = \frac{d_{A_1}}{12} = 2.23 \times 10^{-3} \text{ (molec/cm}^3\text{)}^{-1},$$

so that

$$\begin{aligned}
d_{A_1^{LN} P_D^{8LN}} &= 6.72 \times 10^{-13} \text{ (molec/cm}^3\text{)}^{-1} \text{ day}^{-1}, \\
d_{A_1^{LN} P_D^{1LN}} &= 1.89 \times 10^{-13} \text{ (molec/cm}^3\text{)}^{-1} \text{ day}^{-1}, \\
d_{A_1^{LN} P_D^{rLN}} &= 2.27 \times 10^{-13} \text{ (molec/cm}^3\text{)}^{-1} \text{ day}^{-1}.
\end{aligned}$$

C.14 Model Parameters

Table C.1: Parameter values for the model. TDLN denotes the tumour-draining lymph node, whilst TS denotes the tumour site. est. denotes estimated parameters.

Parameter	Description	Value	Unit	References
\mathcal{A}_{D_0}	Source of D_0	9.89×10^5	$(\text{cell/cm}^3) \text{ day}^{-1}$	est.
$\mathcal{A}_{T_0^8}$	Source of T_0^8	3.71×10^5	$(\text{cell/cm}^3) \text{ day}^{-1}$	est.
$\mathcal{A}_{T_0^4}$	Source of T_0^4	2.69×10^5	$(\text{cell/cm}^3) \text{ day}^{-1}$	est.
$\mathcal{A}_{T_0^r}$	Source of T_0^r	9.95×10^4	$(\text{cell/cm}^3) \text{ day}^{-1}$	est.
\mathcal{A}_{M_0}	Source of M_0	9.97×10^5	$(\text{cell/cm}^3) \text{ day}^{-1}$	est.
\mathcal{A}_{K_0}	Source of K_0	3.71×10^5	$(\text{cell/cm}^3) \text{ day}^{-1}$	est.
λ_C	Growth rate of C	8.35×10^{-1}	day^{-1}	est.
λ_{CT_8}	Elimination rate of C by T_8	5.60×10^{-7}	$(\text{cell/cm}^3)^{-1} \text{ day}^{-1}$	est.
λ_{CT_1}	Elimination rate of C by T_1	1.75×10^{-8}	$(\text{cell/cm}^3)^{-1} \text{ day}^{-1}$	est.
λ_{CK}	Elimination rate of C by K	5.60×10^{-7}	$(\text{cell/cm}^3)^{-1} \text{ day}^{-1}$	est.
λ_{CI_α}	Necrosis rate of C by I_α	1.63×10^{-1}	day^{-1}	est.
λ_{CI_γ}	Necrosis rate of C by I_γ	3.30×10^{-2}	day^{-1}	est.
λ_{HN_c}	Production rate of H by N_c	8.59×10^{-15}	$(\text{g/cell}) \text{ day}^{-1}$	est.
λ_{HC_F}	Production rate of H by C_F	9.55×10^{-16}	$(\text{g/cell}) \text{ day}^{-1}$	est.
λ_{SN_c}	Production rate of S by N_c	1.70×10^{-14}	$(\text{g/cell}) \text{ day}^{-1}$	est.
λ_{DH}	Maturation rate of D_0 by H	1.98×10^{-1}	day^{-1}	est.
λ_{DS}	Maturation rate of D_0 by S	1.98×10^{-2}	day^{-1}	est.
λ_{D_0K}	Killing rate of D_0 by K	1.11×10^{-7}	$(\text{cell/cm}^3)^{-1} \text{ day}^{-1}$	est.
$\lambda_{DD^{LN}}$	Migration rate of D to TDLN	1.68×10^{-2}	day^{-1}	est.
$\lambda_{T_0^8 T_A^8}$	Kinetic rate constant for T_0^8 activation	2.94×10^{-11}	$(\text{cell/cm}^3)^{-1}$	est.
$\lambda_{T_A^8 T_8}$	Kinetic rate constant for T_A^8 migration to TS	3.41×10^{-1}	day^{-1}	est.
$\lambda_{T_8 I_2}$	Growth rate of T_8 by I_2	8.04×10^{-4}	day^{-1}	est.
$\lambda_{T_8 C}$	Exhaustion rate of T_8 due to C exposure	7.08×10^{-3}	day^{-1}	est.
$\lambda_{T_{\text{ex}} A_1}$	Reinvigoration rate of T_{ex} by A_1	2.25×10^{-3}	day^{-1}	est.
$\lambda_{T_0^4 T_A^1}$	Kinetic rate constant for T_0^4 activation into T_A^1	5.16×10^{-11}	$(\text{cell/cm}^3)^{-1}$	est.
$\lambda_{T_A^1 T_1}$	Kinetic rate constant for T_A^1 migration to TS	2.88×10^{-2}	day^{-1}	est.
$\lambda_{T_1 I_2}$	Growth rate of T_1 by I_2	8.00×10^{-4}	day^{-1}	est.
$\lambda_{T_0^r T_A^r}$	Kinetic rate constant for T_0^r activation into T_A^r	3.05×10^{-8}	$(\text{cell/cm}^3)^{-1}$	est.

$\lambda_{T_A^r T_r}$	Kinetic rate constant for T_A^r migration to TS	5.82×10^{-1}	day ⁻¹	est.
λ_{C_F}	Growth rate of C_F	6.93×10^{-1}	day ⁻¹	[54]
$\lambda_{C_F I_\beta}$	Growth rate of C_F by I_β	9.98×10^{-1}	day ⁻¹	est.
$\lambda_{M_1 I_\alpha}$	Polarisation rate of M_0 to M_1 by I_α	0.23	day ⁻¹	est.
$\lambda_{M_1 I_\gamma}$	Polarisation rate of M_0 to M_1 by I_γ	2.68×10^{-1}	day ⁻¹	est.
$\lambda_{M_2 I_{10}}$	Polarisation rate of M_0 to M_2 by I_{10}	1.46×10^{-1}	day ⁻¹	est.
$\lambda_{M_2 P_L}$	Polarisation rate of M_0 to M_2 by P_L	1.78	day ⁻¹	est.
$\lambda_{M I_\gamma}$	Polarisation rate of M_2 to M_1 by I_γ	2.05×10^{-1}	day ⁻¹	est.
$\lambda_{M I_\alpha}$	Polarisation rate of M_2 to M_1 by I_α	1.71×10^{-1}	day ⁻¹	est.
$\lambda_{M I_\beta}$	Polarisation rate of M_1 to M_2 by I_β	8.12×10^{-2}	day ⁻¹	est.
$\lambda_{M I_6}$	Polarisation rate of M_1 to M_2 by I_6	1.62×10^{-2}	day ⁻¹	est.
$\lambda_{K I_2}$	Maturation rate of K_0 by I_2	4.62×10^{-1}	day ⁻¹	est.
$\lambda_{K D_0}$	Maturation rate of K_0 by D_0	1.54×10^{-1}	day ⁻¹	est.
$\lambda_{K D}$	Maturation rate of K_0 by D	7.70×10^{-1}	day ⁻¹	est.
$\lambda_{I_2 T_8}$	Production rate of I_2 by T_8	7.44×10^{-16}	(g/cell) ⁻¹ day ⁻¹	est.
$\lambda_{I_2 T_1}$	Production rate of I_2 by T_1	2.18×10^{-15}	(g/cell) ⁻¹ day ⁻¹	est.
$\lambda_{I_\gamma T_8}$	Production rate of I_γ by T_8	1.26×10^{-17}	(g/cell) ⁻¹ day ⁻¹	est.
$\lambda_{I_\gamma T_1}$	Production rate of I_γ by T_1	4.40×10^{-18}	(g/cell) ⁻¹ day ⁻¹	est.
$\lambda_{I_\gamma K}$	Production rate of I_γ by K	1.16×10^{-16}	(g/cell) ⁻¹ day ⁻¹	est.
$\lambda_{I_\alpha T_8}$	Production rate of I_α by T_8	3.24×10^{-16}	(g/cell) ⁻¹ day ⁻¹	est.
$\lambda_{I_\alpha T_1}$	Production rate of I_α by T_1	5.36×10^{-16}	(g/cell) ⁻¹ day ⁻¹	est.
$\lambda_{I_\alpha M_1}$	Production rate of I_α by M_1	1.97×10^{-16}	(g/cell) ⁻¹ day ⁻¹	est.
$\lambda_{I_\alpha K}$	Production rate of I_α by K	5.66×10^{-16}	(g/cell) ⁻¹ day ⁻¹	est.
$\lambda_{I_\beta C}$	Production rate of I_β by C	7.08×10^{-12}	(g/cell) ⁻¹ day ⁻¹	est.
$\lambda_{I_\beta T_r}$	Production rate of I_β by T_r	4.10×10^{-11}	(g/cell) ⁻¹ day ⁻¹	est.
$\lambda_{I_\beta C_F}$	Production rate of I_β by C_F	1.42×10^{-11}	(g/cell) ⁻¹ day ⁻¹	est.
$\lambda_{I_{10} C}$	Production rate of I_{10} by C	1.94×10^{-17}	(g/cell) ⁻¹ day ⁻¹	est.
$\lambda_{I_{10} M_2}$	Production rate of I_{10} by M_2	3.89×10^{-17}	(g/cell) ⁻¹ day ⁻¹	est.
$\lambda_{I_{10} T_r}$	Production rate of I_{10} by T_r	7.34×10^{-18}	(g/cell) ⁻¹ day ⁻¹	est.
$\lambda_{I_{10} I_2}$	Production ratio of I_{10} by I_2	3	dimensionless	[58] est.
$\lambda_{I_6 D}$	Production rate of I_6 by D	1.56×10^{-14}	(g/cell) ⁻¹ day ⁻¹	est.
$\lambda_{I_6 C_F}$	Production rate of I_6 by C_F	1.35×10^{-13}	(g/cell) ⁻¹ day ⁻¹	est.
f_{pembro}	A_1/A_1^{LN} dose scaling factor	2.90×10^{-7}	g/cm ³ day ⁻¹ /mg	[26] est.
$K_{C I_\alpha}$	Half-saturation constant of I_α for C	5.30×10^{-11}	g/cm ³	[14] est.
$K_{C I_\gamma}$	Half-saturation constant of I_γ for C	1.69×10^{-11}	g/cm ³	[8] est.
$K_{D H}$	Half-saturation constant of H for D	1.01×10^{-8}	g/cm ³	[6] est.

K_{DS}	Half-saturation constant of S for D	4.50×10^{-8}	g/cm ³	[7] est.
$K_{T_8 I_2}$	Half-saturation constant of I_2 for T_8	2.00×10^{-12}	g/cm ³	[10] est.
$K_{T_8 C}$	Half-saturation constant T_8 exhaustion due to C exposure	3.31×10^8	(cell/cm ³) day	est.
$K_{T_{ex} A_1}$	Half-saturation constant of T_{ex} reinvigoration by A_1	5.08×10^{-5}	g/cm ³	est.
$K_{T_1 I_2}$	Half-saturation constant of I_2 for T_1	2.00×10^{-12}	g/cm ³	[10] est.
$K_{C_F I_\beta}$	Half-saturation constant of I_β for C_F	1.51×10^{-6}	g/cm ³	[16] est.
$K_{M_1 I_\alpha}$	Half-saturation constant of I_α for M_1	5.30×10^{-11}	g/cm ³	[14] est.
$K_{M_1 I_\gamma}$	Half-saturation constant of I_γ for M_1	1.69×10^{-11}	g/cm ³	[8] est.
$K_{M_2 I_{10}}$	Half-saturation constant of I_{10} for M_2	1.15×10^{-10}	g/cm ³	[14] est.
$K_{M_2 P_L}$	Half-saturation constant of P_L for M_2	1.39×10^{11}	g/cm ³	est.
$K_{M I_\gamma}$	Half-saturation constant of I_γ for M_1/M_2	1.69×10^{-11}	g/cm ³	[8] est.
$K_{M I_\alpha}$	Half-saturation constant of I_α for M_1/M_2	5.30×10^{-11}	g/cm ³	[14] est.
$K_{M I_\beta}$	Half-saturation constant of I_β for M_1/M_2	1.51×10^{-6}	g/cm ³	[16] est.
$K_{M I_6}$	Half-saturation constant of I_6 for M_1/M_2	3.12×10^{-6}	g/cm ³	[16] est.
$K_{K I_2}$	Half-saturation constant of I_2 for K	2.00×10^{-12}	g/cm ³	[10] est.
$K_{K D_0}$	Half-saturation constant of D_0 for K	1.46×10^6	cell/cm ³	est.
$K_{K D}$	Half-saturation constant of D for K	4.78×10^5	cell/cm ³	est.
$K_{I_{10} I_2}$	Half-saturation constant of I_2 for I_{10}	5.47×10^8	g/cm ³	est.
C_0	Carrying capacity of C	2.00×10^{-12}	cell/cm ³	est.
$K_{C I_\beta}$	Inhibition constant of T_8 elimination of C by I_β	1.51×10^{-6}	g/cm ³	est.
$K_{C P_L^C}$	Inhibition constant of T_8 elimination of C by P_L^C	5.53×10^{10}	molec/cm ³	est.
$K_{C I_6}$	Inhibition constant of K elimination of C by I_6	3.12×10^{-6}	g/cm ³	est.
$K_{C P_D}$	Inhibition constant of K elimination of C by P_D	7.88×10^9	molec/cm ³	est.
V_{TS}	Volume of the TS	2.76×10^1	cm ³	[71] est.
V_{LN}	Volume of the TDLN	9.20×10^{-2}	cm ³	[59] est.

$K_{T_0^8 P_D^{8LN}}$	Inhibition constant of T_0^8 activation by P_D^{8LN}	6.62×10^9	(molec/cm ³) day	est.
$K_{T_A^8 Q^{8LN}}$	Inhibition constant of activated CD8+ T cell proliferation by Q^{8LN}	4.48×10^5	(molec/cm ³) day	est.
$K_{T_8 I_{10}}$	Inhibition constant of T_8 death by I_{10}	1.15×10^{-10}	g/cm ³	[14] est.
$K_{T_{ex} I_{10}}$	Inhibition constant of T_{ex} death by I_{10}	1.15×10^{-10}	g/cm ³	[14] est.
$K_{T_0^4 P_D^{1LN}}$	Inhibition constant of T_0^4 activation by P_D^{1LN}	1.77×10^{10}	(molec/cm ³) day	est.
$K_{T_A^1 Q^{1LN}}$	Inhibition constant of activated Th1 cell proliferation by Q^{1LN}	1.35×10^6	(molec/cm ³) day	est.
$K_{T_0^r P_D^{rLN}}$	Inhibition constant of T_0^r activation by P_D^{rLN}	1.47×10^{10}	(molec/cm ³) day	est.
$K_{T_A^r Q^{rLN}}$	Inhibition constant of activated Treg proliferation by Q^{rLN}	7.84×10^5	(molec/cm ³) day	est.
C_{F0}	Carrying Capacity of C_F	3.07×10^7	cell/cm ³	est.
$K_{I_\gamma T_r}$	Inhibition constant of T cell production of I_γ by T_r	1.45×10^5	cell/cm ³	est.
d_{N_c}	Removal rate of N_c	0.89	day ⁻¹	est.
d_H	Degradation rate of H	5.55	day ⁻¹	[27] est.
d_S	Degradation rate of S	1.39	day ⁻¹	[28, 29] est.
d_{D_0}	Death rate of D_0	3.57×10^{-2}	day ⁻¹	[30] est.
d_D	Death rate of D	3.15×10^{-1}	day ⁻¹	[31] est.
$d_{T_0^8}$	Death rate of T_0^8	3.22×10^{-2}	day ⁻¹	[32] est.
d_{T_8}	Death rate of T_8	9×10^{-3}	day ⁻¹	[33]
$d_{T_{ex}}$	Death rate of T_{ex}	9×10^{-3}	day ⁻¹	[33]
$d_{T_0^4}$	Death rate of T_0^4	4.03×10^{-2}	day ⁻¹	[32] est.
d_{T_1}	Death rate of T_1	8×10^{-3}	day ⁻¹	[33]
$d_{T_0^r}$	Death rate of T_0^r	2.2×10^{-3}	day ⁻¹	[34]
d_{T_r}	Death rate of T_r	6.30×10^{-2}	day ⁻¹	[35] est.
d_{C_F}	Death rate of C_F	1.98×10^{-1}	day ⁻¹	[36] est.
d_{M_0}	Death rate of M_0	0.73	day ⁻¹	[37]
d_{M_1}	Death rate of M_1	0.99	day ⁻¹	[37]
d_{M_2}	Death rate of M_2	1.35×10^{-1}	day ⁻¹	[37]
d_{K_0}	Death rate of K_0	6.93×10^{-2}	day ⁻¹	[38–40] est.
d_K	Death rate of K	6.93×10^{-2}	day ⁻¹	[38–40] est.
d_{I_2}	Degradation rate of I_2	1.45×10^2	day ⁻¹	[41] est.
d_{I_γ}	Degradation rate of I_γ	3.33×10^1	day ⁻¹	[42] est.
d_{I_α}	Degradation rate of I_α	5.48×10^1	day ⁻¹	[72, 73] est.
d_{I_β}	Degradation rate of I_β	3.99×10^2	day ⁻¹	[45] est.
$d_{I_{10}}$	Degradation rate of I_{10}	6.16	day ⁻¹	[46] est.
d_{I_6}	Degradation rate of I_6	1.11	day ⁻¹	[48] est.
$d_{P_D A_1}$	Depletion rate of P_D by A_1	3.62×10^{-1}	(g/cm ³) ⁻¹ day ⁻¹	est.
$d_{P_D^{8LN} A_1^{LN}}$	Depletion rate of P_D^{8LN} by A_1^{LN}	3.62×10^{-1}	(g/cm ³) ⁻¹ day ⁻¹	est.
$d_{P_D^{1LN} A_1^{LN}}$	Depletion rate of P_D^{1LN} by A_1^{LN}	3.62×10^{-1}	(g/cm ³) ⁻¹ day ⁻¹	est.

$d_{P_D^{rLN} A_1^{LN}}$	Depletion rate of P_D^{rLN} by A_1^{LN}	3.62×10^{-1}	$(\text{g}/\text{cm}^3)^{-1} \text{day}^{-1}$	est.
$\alpha_{P_D^{LN} P_L^{LN}}$	Formation rate of $Q^{8LN}/Q^{1LN}/Q^{rLN}$	2.64×10^{-11}	$(\text{molec}/\text{cm}^3)^{-1} \text{day}^{-1}$	[22]
$d_{Q^{LN}}$	Dissociation rate of $Q^{8LN}/Q^{1LN}/Q^{rLN}$	1.24×10^5	day^{-1}	[22]
$d_{A_1 P_D}$	Depletion rate of A_1 from blocking P_D	8.47×10^{-13}	$(\text{molec}/\text{cm}^3)^{-1} \text{day}^{-1}$	est.
d_{A_1}	Degradation rate of A_1/A_1^{LN}	2.67×10^{-2}	day^{-1}	[49–51] est.
$d_{A_1^{LN} P_D^{8LN}}$	Depletion rate of A_1^{LN} from blocking P_D^{8LN}	6.72×10^{-13}	$(\text{molec}/\text{cm}^3)^{-1} \text{day}^{-1}$	est.
$d_{A_1^{LN} P_D^{1LN}}$	Depletion rate of A_1^{LN} from blocking P_D^{1LN}	1.89×10^{-13}	$(\text{molec}/\text{cm}^3)^{-1} \text{day}^{-1}$	est.
$d_{A_1^{LN} P_D^{rLN}}$	Depletion rate of A_1^{LN} from blocking P_D^{rLN}	2.27×10^{-13}	$(\text{molec}/\text{cm}^3)^{-1} \text{day}^{-1}$	est.
$\rho_{P_D^8}$	Number of PD-1 molecules expressed on T_8/T_A^8	2.76×10^3	molec/cell	[19]
$\rho_{P_D^{\text{ex}}}$	Number of P_D molecules expressed on T_{ex}	1.38×10^4	molec/cell	[19] est.
$\rho_{P_D^1}$	Number of PD-1 molecules expressed on T_1/T_A^1	2.05×10^3	molec/cell	[19]
$\rho_{P_D^r}$	Number of PD-1 molecules expressed on T_r/T_A^r	2.05×10^3	molec/cell	[19]
$\rho_{P_D^{M2}}$	Number of PD-1 molecules expressed on M_2	1.47×10^3	molec/cell	[19]
$\rho_{P_D^K}$	Number of PD-1 molecules expressed on K	5.52×10^2	molec/cell	est.
$\rho_{P_L^C}$	Number of PD-L1 molecules expressed on C	1.67×10^3	molec/cell	[23] est.
$\rho_{P_L^D}$	Number of PD-L1 molecules expressed on D/D^{LN}	1.77×10^4	molec/cell	[22, 24]
$\rho_{P_L^8}$	Number of PD-L1 molecules expressed on T_8/T_A^8	1.49×10^3	molec/cell	[22, 23]
$\rho_{P_L^1}$	Number of PD-L1 molecules expressed on T_1/T_A^1	2.08×10^3	molec/cell	[22, 23]
$\rho_{P_L^r}$	Number of PD-L1 molecules expressed on T_r/T_A^r	2.08×10^3	molec/cell	[22, 23]
$\rho_{P_L^{CF}}$	Number of PD-L1 molecules expressed on C_F	2.81×10^3	molec/cell	[23] est.
$\rho_{P_L^{M2}}$	Number of PD-L1 molecules expressed on M_2	1.79×10^3	molec/cell	[1, 25] est.
τ_m	DC migration time from TDLN to TS	0.75	day	[60] est.
τ_8^{act}	CD8+ T cell activation time	2	day	[74]
Δ_8^0	Time taken for first CTL division	1.63	day	[62]
n_{max}^8	Maximal number of CTL divisions in the TDLN	10	dimensionless	[63, 64] est.

Δ_8	Time taken for successive CTL divisions	0.36	day	[63]
$\tau_{T_A^8}$	Time taken for CTL division program	4.87	day	est.
τ_a	T cell migration time from TDLN to TS	0.27	day	est.
τ_l	Time for CTL to become exhausted in TS	10	day	[65, 66] est.
τ_4^{act}	CD4+ T cell activation time	1.5	day	[67] est.
Δ_1^0	Time taken for first Th1 cell division	0.77	day	[69] est.
n_{max}^1	Maximal number of Th1 cell divisions in the TDLN	9	dimensionless	[68] est.
Δ_1	Time taken for successive Th1 cell divisions	0.42	day	[69] est.
$\tau_{T_A^1}$	Time taken for Th1 cell division program	4.13	day	est.
τ_r^{act}	Treg activation time	1.5	day	[67] est.
Δ_r^0	Time taken for first Treg division	0.77	day	[69] est.
n_{max}^r	Maximal number of Treg divisions in the TDLN	6	dimensionless	[70] est.
Δ_r	Time taken for successive Treg divisions	0.42	day	[69] est.
$\tau_{T_A^r}$	Time taken for Treg division program	2.87	day	est.

References

- [1] Siewe N, Friedman A. TGF- β inhibition can overcome cancer primary resistance to PD-1 blockade: A mathematical model. PLOS ONE. 2021 Jun;16(6):e0252620. Available from: <http://dx.doi.org/10.1371/journal.pone.0252620>.
- [2] Siewe N, Friedman A. Optimal timing of steroid initiation in response to CTLA-4 antibody in metastatic cancer: A mathematical model. PLOS ONE. 2022 Nov;17(11):e0277248. Available from: <http://dx.doi.org/10.1371/journal.pone.0277248>.
- [3] Siewe N, Friedman A. Cancer therapy with immune checkpoint inhibitor and CSF-1 blockade: A mathematical model. Journal of Theoretical Biology. 2023 Jan;556:111297. Available from: <http://dx.doi.org/10.1016/j.jtbi.2022.111297>.
- [4] Han Y, Liu D, Li L. PD-1/PD-L1 pathway: current researches in cancer. American journal of cancer research. 2020;10(3):727. Available from: <https://pmc.ncbi.nlm.nih.gov/articles/PMC7136921/>.
- [5] Berenbaum M. In vivo determination of the fractional kill of human tumor cells by chemotherapeutic agents. Cancer chemotherapy reports. 1972;56(5):563-71.

- [6] Zhang W, An F, Xia M, Zhan Q, Tian W, Jiao Y. Increased HMGB1 expression correlates with higher expression of c-IAP2 and pERK in colorectal cancer. *Medicine*. 2019 Jan;98(3):e14069. Available from: <http://dx.doi.org/10.1097/MD.00000000000014069>.
- [7] Abdullah TM, Whatmore J, Bremer E, Slibinskas R, Michalak M, Eggleton P. Endoplasmic reticulum stress-induced release and binding of calreticulin from human ovarian cancer cells. *Cancer Immunology, Immunotherapy*. 2021 Nov;71(7):1655–1669. Available from: <http://dx.doi.org/10.1007/s00262-021-03072-6>.
- [8] Calu V, Ionescu A, Stanca L, Geicu OI, Iordache F, Pisoschi AM, et al. Key biomarkers within the colorectal cancer related inflammatory microenvironment. *Scientific Reports*. 2021 Apr;11(1). Available from: <http://dx.doi.org/10.1038/s41598-021-86941-5>.
- [9] Kim YW, Kim SK, Kim CS, Kim IY, Cho MY, Kim NK. Association of Serum and Intratumoral Cytokine Profiles with Tumor Stage and Neutrophil Lymphocyte Ratio in Colorectal Cancer. *Anticancer research*. 2014;34(7):3481-7. Available from: <https://ar.iiarjournals.org/content/34/7/3481.long>.
- [10] Autenshlyus AI, Arkhipov SA, Kunts TA, Marinkin IO, Mikhailova ES, Karpukhina XV, et al. Cytokine profiles of tumor supernatants in invasive ductal cancer and fibroadenoma of the breast and its relationship with VEGF-A expression in the tumors. *International Journal of Immunopathology and Pharmacology*. 2017 Jan;30(1):83–88. Available from: <http://dx.doi.org/10.1177/0394632016681306>.
- [11] Zhao H, Wu L, Yan G, Chen Y, Zhou M, Wu Y, et al. Inflammation and tumor progression: signaling pathways and targeted intervention. *Signal Transduction and Targeted Therapy*. 2021 Jul;6(1). Available from: <http://dx.doi.org/10.1038/s41392-021-00658-5>.
- [12] West WH. Continuous infusion recombinant interleukin-2 (rIL-2) in adoptive cellular therapy of renal carcinoma and other malignancies. *Cancer Treatment Reviews*. 1989 Jun;16:83–89. Available from: [http://dx.doi.org/10.1016/0305-7372\(89\)90027-3](http://dx.doi.org/10.1016/0305-7372(89)90027-3).
- [13] Czajka-Francuz P, Francuz T, Cisoń-Jurek S, Czajka A, Fajkis M, Szymczak B, et al. Serum cytokine profile as a potential prognostic tool in colorectal cancer patients – one center study. *Reports of Practical Oncology & Radiotherapy*. 2020 Nov;25(6):867–875. Available from: <http://dx.doi.org/10.1016/j.rpor.2020.08.004>.
- [14] Sharp SP, Avram D, Stain SC, Lee EC. Local and systemic Th17 immune response associated with advanced stage colon cancer. *Journal of Surgical Research*. 2017 Feb;208:180–186. Available from: <http://dx.doi.org/10.1016/j.jss.2016.09.038>.
- [15] Krzystek-Korpacka M, Diakowska D, Kapturkiewicz B, Bębenek M, Gamian A. Profiles of circulating inflammatory cytokines in colorectal cancer (CRC), high cancer risk conditions, and health are distinct. Possible implications for CRC screening and surveillance. *Cancer Letters*. 2013 Aug;337(1):107–114. Available from: <http://dx.doi.org/10.1016/j.canlet.2013.05.033>.
- [16] Wang J, Xu K, Wu J, Luo C, Li Y, Wu X, et al. The changes of Th17 cells and the related cytokines in the progression of human colorectal cancers. *BMC Cancer*. 2012 Sep;12(1). Available from: <http://dx.doi.org/10.1186/1471-2407-12-418>.

- [17] Shim KS, Kim KH, Han WS, Park EB. Elevated serum levels of transforming growth factor beta 1 in patients with colorectal carcinoma. *Cancer*. 1999 Feb;85(3):554–561. Available from: [http://dx.doi.org/10.1002/\(SICI\)1097-0142\(19990201\)85:3<554::AID-CNCR6>3.0.CO;2-X](http://dx.doi.org/10.1002/(SICI)1097-0142(19990201)85:3<554::AID-CNCR6>3.0.CO;2-X).
- [18] Stanilov N, Miteva L, Deliysky T, Jovchev J, Stanilova S. Advanced Colorectal Cancer Is Associated With Enhanced IL-23 and IL-10 Serum Levels. *Laboratory Medicine*. 2010 Mar;41(3):159–163. Available from: <http://dx.doi.org/10.1309/LM7T43AQZIUPIOWZ>.
- [19] Pluim D, Ros W, Miedema IHC, Beijnen JH, Schellens JHM. Multiparameter Flow Cytometry Assay for Quantification of Immune Cell Subsets, PD-1 Expression Levels and PD-1 Receptor Occupancy by Nivolumab and Pembrolizumab. *Cytometry Part A*. 2019 Aug;95(10):1053–1065. Available from: <http://dx.doi.org/10.1002/cyto.a.23873>.
- [20] Jiang Y, Li Y, Zhu B. T-cell exhaustion in the tumor microenvironment. *Cell Death & Disease*. 2015 Jun;6(6):e1792–e1792. Available from: <http://dx.doi.org/10.1038/cddis.2015.162>.
- [21] Liu Y, Cheng Y, Xu Y, Wang Z, Du X, Li C, et al. Increased expression of programmed cell death protein 1 on NK cells inhibits NK-cell-mediated anti-tumor function and indicates poor prognosis in digestive cancers. *Oncogene*. 2017 Jul;36(44):6143–6153. Available from: <http://dx.doi.org/10.1038/onc.2017.209>.
- [22] Cheng X, Veverka V, Radhakrishnan A, Waters LC, Muskett FW, Morgan SH, et al. Structure and Interactions of the Human Programmed Cell Death 1 Receptor. *Journal of Biological Chemistry*. 2013 Apr;288(17):11771–11785. Available from: <http://dx.doi.org/10.1074/jbc.M112.448126>.
- [23] Saito A, Tojo M, Kumagai Y, Ohzawa H, Yamaguchi H, Miyato H, et al. Flow cytometry detection of cell type-specific expression of programmed death receptor ligand-1 (PD-L1) in colorectal cancer specimens. *Heliyon*. 2021 Jan;7(1):e05880. Available from: <http://dx.doi.org/10.1016/j.heliyon.2020.e05880>.
- [24] Moreira TG, Mangani D, Cox LM, Leibowitz J, Lobo ELC, Oliveira MA, et al. PD-L1+ and XCR1+ dendritic cells are region-specific regulators of gut homeostasis. *Nature Communications*. 2021 Aug;12(1). Available from: <http://dx.doi.org/10.1038/s41467-021-25115-3>.
- [25] Lai X, Friedman A. Mathematical modeling of cancer treatment with radiation and PD-L1 inhibitor. *Science China Mathematics*. 2020 Feb;63(3):465–484. Available from: <http://dx.doi.org/10.1007/s11425-019-1648-6>.
- [26] Lala M, Li TR, de Alwis DP, Sinha V, Mayawala K, Yamamoto N, et al. A six-weekly dosing schedule for pembrolizumab in patients with cancer based on evaluation using modelling and simulation. *European Journal of Cancer*. 2020 May;131:68–75. Available from: <http://dx.doi.org/10.1016/j.ejca.2020.02.016>.
- [27] Zandarashvili L, Sahu D, Lee K, Lee YS, Singh P, Rajarathnam K, et al. Real-time Kinetics of High-mobility Group Box 1 (HMGB1) Oxidation in Extracellular Fluids Studied by in Situ Protein NMR Spectroscopy. *Journal of Biological Chemistry*. 2013 Apr;288(17):11621–11627. Available from: <http://dx.doi.org/10.1074/jbc.M113.449942>.
- [28] Zhang Y, Thangam R, You SH, Sultonova RD, Venu A, Min JJ, et al. Engineering Calreticulin-Targeting Monobodies to Detect Immunogenic Cell Death in Cancer Chemotherapy. *Cancers*. 2021 Jun;13(11):2801. Available from: <http://dx.doi.org/10.3390/cancers13112801>.

- [29] Goicoechea SM, Murphy-Ullrich JE. In: Cell Surface Calreticulin: Role in Signaling Thrombospondin Anti-Adhesive Activity. Springer US; 2003. p. 193–204. Available from: http://dx.doi.org/10.1007/978-1-4419-9258-1_18.
- [30] Ruedl C, Koebel P, Bachmann M, Hess M, Karjalainen K. Anatomical Origin of Dendritic Cells Determines Their Life Span in Peripheral Lymph Nodes. *The Journal of Immunology*. 2000 Nov;165(9):4910–4916. Available from: <http://dx.doi.org/10.4049/jimmunol.165.9.4910>.
- [31] Kamath AT, Henri S, Battye F, Tough DF, Shortman K. Developmental kinetics and lifespan of dendritic cells in mouse lymphoid organs. *Blood*. 2002 Sep;100(5):1734–1741. Available from: http://dx.doi.org/10.1182/blood.V100.5.1734.h81702001734_1734_1741.
- [32] Takada K, Jameson SC. Self-class I MHC molecules support survival of naive CD8 T cells, but depress their functional sensitivity through regulation of CD8 expression levels. *Journal of Experimental Medicine*. 2009 Sep;206(10):2253–2269. Available from: <http://dx.doi.org/10.1084/jem.20082553>.
- [33] Hellerstein M, Hanley MB, Cesar D, Siler S, Papageorgopoulos C, Wieder E, et al. Directly measured kinetics of circulating T lymphocytes in normal and HIV-1-infected humans. *Nature Medicine*. 1999 Jan;5(1):83–89. Available from: <http://dx.doi.org/10.1038/4772>.
- [34] Kumbhari A, Egelston CA, Lee PP, Kim PS. Mature Dendritic Cells May Promote High-Avidity Tuning of Vaccine T Cell Responses. *Frontiers in Immunology*. 2020 Oct;11. Available from: <http://dx.doi.org/10.3389/fimmu.2020.584680>.
- [35] Vukmanovic-Stejic M, Zhang Y, Cook JE, Fletcher JM, McQuaid A, Masters JE, et al. Human CD4+ CD25hi Foxp3+ regulatory T cells are derived by rapid turnover of memory populations in vivo. *Journal of Clinical Investigation*. 2006 Sep;116(9):2423–2433. Available from: <http://dx.doi.org/10.1172/JCI28941>.
- [36] Louzoun Y, Xue C, Lesinski GB, Friedman A. A mathematical model for pancreatic cancer growth and treatments. *Journal of Theoretical Biology*. 2014 Jun;351:74–82. Available from: <http://dx.doi.org/10.1016/j.jtbi.2014.02.028>.
- [37] Patel AA, Zhang Y, Fullerton JN, Boelen L, Rongvaux A, Maini AA, et al. The fate and lifespan of human monocyte subsets in steady state and systemic inflammation. *Journal of Experimental Medicine*. 2017 Jun;214(7):1913–1923. Available from: <http://dx.doi.org/10.1084/jem.20170355>.
- [38] Wu SY, Fu T, Jiang YZ, Shao ZM. Natural killer cells in cancer biology and therapy. *Molecular Cancer*. 2020 Aug;19(1). Available from: <http://dx.doi.org/10.1186/s12943-020-01238-x>.
- [39] Vivier E, Tomasello E, Baratin M, Walzer T, Ugolini S. Functions of natural killer cells. *Nature Immunology*. 2008 Apr;9(5):503–510. Available from: <http://dx.doi.org/10.1038/ni1582>.
- [40] Lowry LE, Zehring WA. Potentiation of Natural Killer Cells for Cancer Immunotherapy: A Review of Literature. *Frontiers in Immunology*. 2017 Sep;8. Available from: <http://dx.doi.org/10.3389/fimmu.2017.01061>.
- [41] Lotze MT, Matory YL, Ettinghausen SE, Rayner AA, Sharrow SO, Seipp CA, et al. In vivo administration of purified human interleukin 2. II. Half life, immunologic effects, and expansion of peripheral lymphoid cells in vivo with recombinant IL 2. *The Journal of Immunology*. 1985 Oct;135(4):2865–2875. Available from: <http://dx.doi.org/10.4049/jimmunol.135.4.2865>.

- [42] Balachandran S, Adams GP. Interferon- γ -Induced Necrosis: An Antitumor Biotherapeutic Perspective. *Journal of Interferon & Cytokine Research*. 2013 Apr;33(4):171–180. Available from: <http://dx.doi.org/10.1089/jir.2012.0087>.
- [43] Ma Y, Zhao S, Shen S, Fang S, Ye Z, Shi Z, et al. A novel recombinant slow-release TNF α -derived peptide effectively inhibits tumor growth and angiogenesis. *Scientific Reports*. 2015 Sep;5(1). Available from: <http://dx.doi.org/10.1038/srep13595>.
- [44] Oliver J, Bland L, Oettinger C, Arduino M, McAllister S, Aguero S, et al. Cytokine kinetics in an in vitro whole blood model following an endotoxin challenge. *Lymphokine and cytokine research*. 1993 April;12(2):115–120. Available from: <https://pubmed.ncbi.nlm.nih.gov/8324076/>.
- [45] Tirado-Rodriguez B, Ortega E, Segura-Medina P, Huerta-Yepez S. TGF- β : An Important Mediator of Allergic Disease and a Molecule with Dual Activity in Cancer Development. *Journal of Immunology Research*. 2014;2014:1–15. Available from: <http://dx.doi.org/10.1155/2014/318481>.
- [46] Huhn RD, Radwanski E, Gallo J, Affrime MB, Sabo R, Gonyo G, et al. Pharmacodynamics of subcutaneous recombinant human interleukin-10 in healthy volunteers. *Clinical Pharmacology & Therapeutics*. 1997 Aug;62(2):171–180. Available from: [http://dx.doi.org/10.1016/S0009-9236\(97\)90065-5](http://dx.doi.org/10.1016/S0009-9236(97)90065-5).
- [47] Waage A, Brandtzaeg P, Halstensen A, Kierulf P, Espevik T. The complex pattern of cytokines in serum from patients with meningococcal septic shock. Association between interleukin 6, interleukin 1, and fatal outcome. *The Journal of experimental medicine*. 1989 Jan;169(1):333–338. Available from: <http://dx.doi.org/10.1084/jem.169.1.333>.
- [48] Wirtz DC, Heller KD, Miltner O, Zilkens KW, Wolff JM. Interleukin-6: a potential inflammatory marker after total joint replacement. *International Orthopaedics*. 2000 Oct;24(4):194–196. Available from: <http://dx.doi.org/10.1007/s002640000136>.
- [49] Yan T, Yu L, Shanguan D, Li W, Liu N, Chen Y, et al. Advances in pharmacokinetics and pharmacodynamics of PD-1/PD-L1 inhibitors. *International Immunopharmacology*. 2023 Feb;115:109638. Available from: <http://dx.doi.org/10.1016/j.intimp.2022.109638>.
- [50] Longoria TC, Tewari KS. Evaluation of the pharmacokinetics and metabolism of pembrolizumab in the treatment of melanoma. *Expert Opinion on Drug Metabolism & Toxicology*. 2016 Aug;12(10):1247–1253. Available from: <http://dx.doi.org/10.1080/17425255.2016.1216976>.
- [51] Dang TO, Ogunniyi A, Barbee MS, Drilon A. Pembrolizumab for the treatment of PD-L1 positive advanced or metastatic non-small cell lung cancer. *Expert Review of Anticancer Therapy*. 2015 Dec;16(1):13–20. Available from: <http://dx.doi.org/10.1586/14737140.2016.1123626>.
- [52] Piccioli D, Sbrana S, Melandri E, Valiante NM. Contact-dependent Stimulation and Inhibition of Dendritic Cells by Natural Killer Cells. *The Journal of Experimental Medicine*. 2002 Feb;195(3):335–341. Available from: <http://dx.doi.org/10.1084/jem.20010934>.
- [53] Verdijk P, Aarntzen EHJG, Lesterhuis WJ, Boullart ACI, Kok E, van Rossum MM, et al. Limited Amounts of Dendritic Cells Migrate into the T-Cell Area of Lymph Nodes but Have High Immune Activating Potential in Melanoma Patients. *Clinical Cancer Research*. 2009 Apr;15(7):2531–2540. Available from: <http://dx.doi.org/10.1158/1078-0432.CCR-08-2729>.

- [54] Potdar PD, Chaudhary S. Molecular characterization of cancer-associated fibroblasts isolated from human colorectal cancer as a major stromal cell component promoting metastasis. *Journal of Unexplored Medical Data*. 2017 Feb;2(1). Available from: <http://dx.doi.org/10.20517/2572-8180.2016.10>.
- [55] Cui A, Huang T, Li S, Ma A, Pérez JL, Sander C, et al. Dictionary of immune responses to cytokines at single-cell resolution. *Nature*. 2023 Dec;625(7994):377–384. Available from: <http://dx.doi.org/10.1038/s41586-023-06816-9>.
- [56] Zhang Y, Lv N, Li M, Liu M, Wu C. Cancer-associated fibroblasts: tumor defenders in radiation therapy. *Cell Death & Disease*. 2023 Aug;14(8). Available from: <http://dx.doi.org/10.1038/s41419-023-06060-z>.
- [57] Gastl GA, Abrams JS, Nanus DM, Oosterkamp R, Silver J, Liu F, et al. Interleukin-10 production by human carcinoma cell lines and its relationship to interleukin-6 expression. *International Journal of Cancer*. 1993 Aug;55(1):96–101. Available from: <http://dx.doi.org/10.1002/ijc.2910550118>.
- [58] Lo WC, Arsenescu V, Arsenescu RI, Friedman A. Inflammatory Bowel Disease: How Effective Is TNF- α Suppression? *PLOS ONE*. 2016 Nov;11(11):e0165782. Available from: <http://dx.doi.org/10.1371/journal.pone.0165782>.
- [59] Rössler O, Betge J, Harbaum L, Mrak K, Tschmelitsch J, Langner C. Tumor size, tumor location, and antitumor inflammatory response are associated with lymph node size in colorectal cancer patients. *Modern Pathology*. 2017 Jun;30(6):897–904. Available from: <http://dx.doi.org/10.1038/modpathol.2016.227>.
- [60] Catron DM, Itano AA, Pape KA, Mueller DL, Jenkins MK. Visualizing the First 50 Hr of the Primary Immune Response to a Soluble Antigen. *Immunity*. 2004 Sep;21(3):341–347. Available from: <http://dx.doi.org/10.1016/j.immuni.2004.08.007>.
- [61] Anaya JM, Shoenfeld Y, Rojas-Villarraga A, Levy RA, Cervera R. *Autoimmunity: from bench to bedside*. El Rosario University Press; 2013.
- [62] Plambeck M, Kazeroonian A, Loeffler D, Kretschmer L, Salinno C, Schroeder T, et al. Heritable changes in division speed accompany the diversification of single T cell fate. *Proceedings of the National Academy of Sciences*. 2022 Feb;119(9). Available from: <http://dx.doi.org/10.1073/pnas.2116260119>.
- [63] Kaech SM, Ahmed R. Memory CD8⁺ T cell differentiation: initial antigen encounter triggers a developmental program in naïve cells. *Nature Immunology*. 2001 May;2(5):415–422. Available from: <http://dx.doi.org/10.1038/87720>.
- [64] Masopust D, Murali-Krishna K, Ahmed R. Quantitating the Magnitude of the Lymphocytic Choriomeningitis Virus-Specific CD8 T-Cell Response: It Is Even Bigger than We Thought. *Journal of Virology*. 2007 Feb;81(4):2002–2011. Available from: <http://dx.doi.org/10.1128/jvi.01459-06>.
- [65] Blank CU, Haining WN, Held W, Hogan PG, Kallies A, Lugli E, et al. Defining ‘T cell exhaustion’. *Nature Reviews Immunology*. 2019 Sep;19(11):665–674. Available from: <http://dx.doi.org/10.1038/s41577-019-0221-9>.

- [66] McLane LM, Abdel-Hakeem MS, Wherry EJ. CD8 T Cell Exhaustion During Chronic Viral Infection and Cancer. *Annual Review of Immunology*. 2019 Apr;37(1):457–495. Available from: <http://dx.doi.org/10.1146/annurev-immunol-041015-055318>.
- [67] Jolley-Gibbs DM, Lepak NM, Yen M, Swain SL. Two Distinct Stages in the Transition from Naive CD4 T Cells to Effectors, Early Antigen-Dependent and Late Cytokine-Driven Expansion and Differentiation. *The Journal of Immunology*. 2000 Nov;165(9):5017–5026. Available from: <http://dx.doi.org/10.4049/jimmunol.165.9.5017>.
- [68] Homann D, Teyton L, Oldstone MBA. Differential regulation of antiviral T-cell immunity results in stable CD8+ but declining CD4+ T-cell memory. *Nature Medicine*. 2001 Aug;7(8):913–919. Available from: <http://dx.doi.org/10.1038/90950>.
- [69] Kaech SM, Wherry EJ, Ahmed R. Effector and memory T-cell differentiation: implications for vaccine development. *Nature Reviews Immunology*. 2002 Apr;2(4):251–262. Available from: <http://dx.doi.org/10.1038/nri778>.
- [70] Darrasse-Jèze G, Bergot AS, Durgeau A, Billiard F, Salomon BL, Cohen JL, et al. Tumor emergence is sensed by self-specific CD44hi memory Tregs that create a dominant tolerogenic environment for tumors in mice. *Journal of Clinical Investigation*. 2009 Aug. Available from: <http://dx.doi.org/10.1172/JCI36628>.
- [71] Park JY, Kim SH, Lee SM, Lee JS, Han JK. CT volumetric measurement of colorectal cancer helps predict tumor staging and prognosis. *PLOS ONE*. 2017 Jun;12(6):e0178522. Available from: <http://dx.doi.org/10.1371/journal.pone.0178522>.
- [72] Ma Y, Zhao S, Shen S, Fang S, Ye Z, Shi Z, et al. A novel recombinant slow-release TNF α -derived peptide effectively inhibits tumor growth and angiogenesis. *Scientific Reports*. 2015 Sep;5(1). Available from: <http://dx.doi.org/10.1038/srep13595>.
- [73] Oliver J, Bland L, Oettinger C, Arduino M, McAllister S, Aguero S, et al. Cytokine kinetics in an in vitro whole blood model following an endotoxin challenge. *Lymphokine and cytokine research*. 1993 April;12(2):115–120. Available from: <https://pubmed.ncbi.nlm.nih.gov/8324076/>.
- [74] Kinjyo I, Qin J, Tan SY, Wellard CJ, Mrass P, Ritchie W, et al. Real-time tracking of cell cycle progression during CD8+ effector and memory T-cell differentiation. *Nature Communications*. 2015 Feb;6(1). Available from: <http://dx.doi.org/10.1038/ncomms7301>.